The Thesis Committee for Aurélien Mainy
Certifies that this is the approved version of the following thesis:

Dynamic Buckling of Thin Metallic Rings Under External Pressure

APPROVED BY
SUPERVISING COMMITTEE:

Supervisor: Krishnaswamy Ravi-Chandar

Co-supervisor: Kenneth M. Liechti

Dynamic Buckling of Thin Metallic Rings Under External Pressure

by

Aurélien Mainy

Thesis

Presented to the Faculty of the Graduate School of

The University of Texas at Austin

in Partial Fulfillment

of the Requirements

for the Degree of

Master of Science in Engineering

The University of Texas at Austin

May 2012

Dedication

À Aurélie.

Acknowledgements

I would like to express my profound thanks and appreciation to my supervisors, Professor Ravi-Chandar and Professor Liechti who made the present work possible by mentoring my studies at the University of Texas at Austin. I am grateful to them for their exceptional guidance, their precious advice and, just as important, their human understanding.

The experience I have lived at UT over the past two years will remain forever in my mind and in my heart. The cultural diversity as well as the unique academic environment made these two years a fantastic experience. I would like to thank my fellow graduate students for their friendship, enriching so much the human experience I have lived: Aaron, Ali, Andrew B. and Andrew G., Aurélien, Claude-Antoine, Guillaume, Mathieu, Romeo, Santiago, Shixuan, Shravan, Sundeep, Thomas and many more. I would like to thank Joseph and Travis of the Machine Shops as well as Pablo of the Electronics Shop for their assistance in preparing the experiments.

I would like to express my enormous thanks to my family: my parents Alain and Béatrice, my brother Pierre-Baptiste, my sister and her husband Marie-Camille and Mickaël. None of this work would have been possible without your invaluable love and support. I owe you so much! Special thanks go to my grand-parents Camille and Paulette: their support has been tremendous over these two years.

I dedicate this thesis to my Love, Aurélie. Despite having half of our hearts separated by the Atlantic during these two years, she managed to keep me motivated by bringing joys and happiness to my life, even in the hardest times. Her strength has been unbelievable. Today, our hearts meet again and we can look serenely for Happiness together. I Love you.

Abstract

Dynamic Buckling of Thin Metallic Rings Under External Pressure

Aurélien Mainy, M.S.E.

The University of Texas at Austin, 2012

Supervisors: Krishnaswamy Ravi-Chandar

Kenneth M. Liechti

The main aim of this thesis is to gain insight through experiments into how the deformation characteristics of a thin ring made of a metallic material such as aluminum depend on the strain-rate. More precisely, this study investigates the buckling behavior of thin metallic rings subjected to a dynamic radial compressive loading. To do so, a total of twelve experiments were performed: three experiments for each of four load levels. The specimens used were aluminum 6061-O circular rings, having a mean radius of 15.5 mm with a radius-to-thickness ratio of 31. The external pressure acting on the specimens was created via electromagnetic induction following a rapid discharge of high voltage through a solenoid that was specially manufactured to interact with the ring specimen. This created a magnetic field that interacted with the specimen and therefore set a pressure on it. Three experiments were performed for each of the following charge levels: 2 kV, 3 kV, 4 kV and 5 kV. These experiments created maximum external pressures in the specimens that varied between 7 MPa and 38 MPa.

The dynamic response of the ring specimens was recorded using a digital high-speed camera; analyses of the images revealed the initial uniform radial acceleration of the rings followed by the onset and evolution of dynamic buckling. The buckling response of the aluminum rings revealed that several different wave lengths (or buckling modes) can be observed simultaneously. These wave lengths correspond to measured mode numbers between 3 and 44, depending on the rate of change of the applied loading with the higher modes selected at higher strain-rates. Superposition of several pictures taken at different times during the experiment shows that as the ring deforms, the buckling waves stay within the same angular sector, keeping the same mode numbers they initially selected all the way during deformation.

Numerical simulations were performed with the finite element program ABAQUS and validated the observation that several different buckling modes appear simultaneously in the rings and that their localizations are governed by material and geometric imperfections in the specimens.

Table of Contents

List of Tables

List of Figures

CHAPTER 1: INTRODUCTION

Dynamic buckling refers to the instability giving rise to buckles in a body subjected to a dynamic load. Mechanically speaking, a dynamic load corresponds to a high strain-rate experienced by this body. Compared to classical tests of buckling, an axially compressed column can sustain a much higher buckling load when it is dynamic than static; there are two possible reasons for the dynamic effects. First, if the dynamic load is applied during a very short period of time compared to the duration taken by the engendered mechanical wave to propagate along the column, the structure can sustain high loads. Second, the high strain-rate behavior of metals may be of first importance in dictating the flow properties of the material and hence influence the inelastic buckling response of the system. These characteristics of a material depend on the level of strain-rate encountered in the application. High strain-rate phenomena arise in a large range of general applications from manufacturing techniques such as deep-drawing and punching, to specialized applications such as armor-plating. The aim of this thesis is to gain insight into how the characteristics of a metallic material such as aluminum depend on the level of strain-rate applied, and how they influence the buckling response.

The work presented in this thesis focuses on buckling of circular aluminum rings undergoing dynamic radial compressive loading. This dynamic loading is created via electromagnetic induction following a rapid discharge of charge stored in capacitors. The typical pressure experienced by the specimen exhibits a sinusoidal time variation, whose amplitude depends on the voltage input, with a period of 25 μs. For the experiments performed in this thesis, charge levels between 2 to 5 kV have been set, leading to maximum amplitudes for the pressure on the order of 7 to 38 MPa, depending on the voltage. The total time of the event is

about 60 μs. High frequency buckling modes are observed with typical mode numbers between 3 and 44. The localized character of these modes and the localization of their onset are specially studied in this work. The dynamic deformations of the rings are recorded using high-speed digital imaging. Pictures taken during the event are analyzed using MATLAB codes and conclusions are deduced from these analyses.

The research on the specific subject of circular rings is intimately linked with the wider area of buckling of cylindrical shells. But whereas these experiments give results based on comparison between length-to-diameter ratios, the results presented in this thesis tend to get rid of the longitudinal dimension, leading to a plane strain approximation and focusing the results on a given diameter-to-thickness ratio of the ring and initial compressive impulse imposed on the specimen.

Buckling of cylinders under axial load has been studied widely in the literature. On the contrary, buckling of the same cylinders but under a radial pressure has drawn less attention. Nonetheless, general theories on buckling of thin circular rings have been developed and a brief summary is presented here.

1.1 Elastic buckling of thin circular rings

The theoretical model to describe elastic buckling of thin circular rings is well-known. Timoshenko (1936) and Brush and Almroth (1975) have described two different approaches for this problem. In both cases a circular ring that can only deform elastically and is subjected to a uniform radial pressure is considered. Timoshenko describes the problem following an analysis of the governing differential equations while Brush and Almroth show an alternative to this method, using energy considerations to derive the characteristic equation for buckling. The

method of Timoshenko is summarized in Chapter 3 of this thesis. It gives a good understanding of the geometric deformations while elastic buckling occurs. The result of this analysis is a relation between the external pressure applied and the buckling mode number appearing on the shape of the ring. The Brush and Almroth analysis goes a bit further as they also describe the case of a centrally directed pressure loading, instead of a pressure normal to the surface. This result is also discussed in Chapter 4.

In our experiments, the pressure is applied in the radial direction of the ring, but over a very short duration. In order to take into account the dynamic effect of such a load, notably through the inertia terms relative to the radial acceleration, special theories have been developed. Lindberg and Florence (1987) describe such a theory; their analysis is based on initial imperfections in the radial and tangential displacements and derives from energy considerations. Furthermore, they considered an impulse loading rather than a continuously varying pressure. The theory they developed seems to agree with experiments for very thin cylindrical shells with a radius-to-thickness ratio of around 480. The present work deals with a radius-to-thickness ratio around 30, and thus an elastic buckling analysis is not sufficient.

1.2 Plastic buckling and dynamic uniform radial impulse

Both Florence (1968) and Jones and Okawa (1976) have developed a model for plastic buckling of rings, under several hypotheses and approximations. First, they considered the pressure to be an impulse rather than a function depending on time. This constitutes a limit to their theory while comparing with the results of our experiments. Nevertheless, the pressure actually encountered in the experiments can be integrated all over the uniform deformation motion of the ring, leading to an interpretation of the pressure as an impulse loading. Another

approximation in the model derived by Florence (1968) as well as Jones and Okawa (1976) is the mechanical behavior of the material. Indeed, even if they deal with an elastic-plastic material, they assume that the plastic region is determined by a constant tangential modulus. An even stronger approximation that is made is that the tangential modulus is small compared to the elastic Young's modulus of the material, which leads to the circumferential compressive stress being constant. Details of this interpretation are shown in Chapter 3.

Jones (1976) studied theoretically the influence of initial imperfections in the geometry of the ring and the impulsive velocity on the appearance of certain modes in the buckled shape. He arrived at the conclusion that buckling is more sensitive to the shape imperfections than to imperfections in the impulsive velocity. For a radius-to-thickness ratio of 30, which is close to the rings used in our experiments, the factor of influence between deflection and velocity imperfections is about 80. In practice, the shape of the rings can be controlled easily, meaning that the results should be predicted within a relatively good tolerance. In the experiments performed in this work, the impulse velocity is produced by electromagnetic interactions created by a solenoid; as a solenoid creates a nearly perfect uniform magnetic field, the influence of the impulse velocity imperfections is expected to be diminished.

In all these works discussed above, the authors considered a global behavior for buckling; that is to say, first a uniform axisymmetric axial motion followed by a perturbed behavior gives rise to buckling waves. Also, only one mode is said to appear in the buckling shape: the most amplified mode given by the theory. No discussions were provided on whether several buckling modes could appear at different places in the ring simultaneously.

Florence (1968) has reported on a series of experiments to study buckling of metallic cylinders: Al 2024-T3, Al 6061-T6, Steel 1015, Brass and Copper. The pressure on the tubes was

produced by an arrangement of an explosive substance separated from the tube by an attenuator made of neoprene foam. The detonation of the explosive induced a shock wave in the attenuator medium, transmitting an impulsive velocity to the cylinder. These velocities were in the range of 45 – 240 m/s; the R/t ratio varied from about 10 for aluminum and copper to 35.6 for steel. The number of crests measured in the experiments was between 9 and 28, corresponding to the buckling mode number. This number depends, of course, on the material used, the ratio radius-to-thickness of the tubes, and the impulse velocity. This last parameter cannot be perfectly controlled in this kind of explosive experiment: several imperfections in the deformed tube shapes are seen at sensitive places such as near the explosive and attenuator joints, resulting in non-uniformities in the velocity distribution. Florence has shown that the number and amplitude of crests increases with the radius-to-thickness ratio. Moreover, after computing the theoretically most magnified component of the buckling terms corresponding to the most probable mode number, Florence showed that experiments agree with the theory developed in that all the measured modes were lower than the theoretical values. Nonetheless, the lower the number of crests, the closer this value was to the theory. For a high mode number, the theoretical value can be twice as large as the measured value.

Jones (1976) performed similar experiments, with a nearly identical arrangement, using aluminum 6061-T6 and rolled mild steel. For steel, the initial impulse velocities measured were in the range of 63 – 250 m/s; the R/t ratio varied from 10 to 43.6. The measured mode numbers starts from 4 for the smaller R/t specimens to 17 for the larger R/t specimens; the corresponding theoretical values are 6 and 18. In comparison, one of the aluminum specimens had a radius-to-thickness ratio of 10 and all the others had ratios around 17.3. The observed mode numbers were between 7 and 11, corresponding to theoretical values from 8 to 11. Florence also computed the

impulse necessary to produce buckling. These threshold impulses range from 130 Pa.s for copper to 270 Pa.s for aluminum 2024-T3. These values will be compared with the pressure encountered by the rings in the experiments performed in this thesis.

Finally, Al-Hassani (1974) appears to have been the only one to have conducted such experiments using electromagnetically induced pressures. In his work, he used an arrangement very similar to that used in the present thesis: a solenoid creates a magnetic field, acting on the specimens and producing a repulsive radial pressure. His aluminum specimens were very of comparable dimensions to that used in the present work. For different length/diameter ratios of the specimens, Al-Hassani measured buckling modes to be between 12 and 18 for discharge energies in the solenoid between 0.36 kJ to 11.53 kJ.

1.3 Outline of present study

This work addresses the dynamic buckling of annealed aluminum 6061-O for a given radius/thickness ratio. This thesis is organized as follows: in Chapter 2, the experimental methods are described, focusing on the governing equations for the magnetic interactions and the procedure for manufacturing the solenoid. In Chapter 3, the results of the experiments are presented and analyzed. The theory of elastic and plastic dynamic buckling is summarized in Chapter 4. A numerical simulation of the problem using the finite element software ABAQUS is also presented in this Chapter 4. Finally, conclusions from this study are summarized in Chapter 5.

CHAPTER 2: EXPERIMENTAL METHODS

The general principle of the experiments performed to investigate the response of a metallic ring to dynamic compressive loading, more precisely its buckling response, is the following: an electrically conducting specimen lies within a specially built solenoid made of six loops. Applying a rapidly varying high-voltage discharge into the solenoid creates an electromagnetic field which interacts with the specimen and then gives birth to a repulsive induced current in the ring. Consequently, a compressive radial load is applied via magnetic induction to the specimen. This experimental method is described in detail in this chapter.

2.1 Electromagnetically Induced Loading

2.1-1 Faraday's Law of Induction

The experiments performed use the concept of electromagnetic induction to produce a dynamic loading on the specimen. According to Faraday's law of electromagnetic induction, first discovered in 1831, an electromotive force (EMF) will be generated on a closed circuit whenever it is subjected to a varying magnetic flux. This condition can be met in two different cases: first, the flux changes itself with time; second, the conductor moves or is in the process of deformation and therefore the flux through it changes. Faraday's equation of induction gives the resulting EMF, calculated in volts:

$$EMF = -\frac{d\phi_B}{dt} \tag{2.1}$$

where ϕ_B is the magnetic flux through the oriented surface $\overrightarrow{dS}$ bounded by the closed circuit:

$$\phi_B = \iint \vec{B}.\overrightarrow{dS} \tag{2.2}$$

$\vec{B}$ being the magnetic field.

According to Lenz's law, this EMF therefore gives rise to a current in the closed circuit, called the induced current, whose direction enables its magnetic field to oppose the original change in magnetic flux. The minus sign in Eq. (2.1) is in accordance with this law, since it indicates that the induced EMF and the change in flux have opposite signs. The induced current is represented by electrically charged particles (charge q) in motion in the metal. Consequently, the Lorentz force will act on these charges according to the following equation:

$$\vec{F} = q\left(\vec{E} + \vec{v} \times \overrightarrow{B}\right) \tag{2.3}$$

where $\vec{F}$ is the force, $\vec{E}$ is the electric field, $\vec{B}$ is the magnetic field and $\vec{v}$ is the instantaneous velocity of the particle. Considering the particles in motion, which constitutes the current, the closed circuit is subject to the magnetic force q $(\vec{v} \times \overrightarrow{B})$, whose macroscopic resultant is called the Lorentz force, given by:

$$\vec{F} = \vec{j} \times \vec{B} \tag{2.4}$$

where $\vec{j}$ is the density of current induced in the closed circuit. This is the force that the conductor will actually experience.

In this work, the magnetic field $\vec{B}$ is created by a solenoid: it is subjected to current derived from discharge of a high voltage capacitor (described later in this document). The magnetic field depends on time and therefore, the specimen placed inside the solenoid experiences an external radial force according to the reasoning developed earlier. The rapidity with which the capacitors are discharged as well as the charge level are the two key parameters that allow us to vary on the radial pressure and hence the strain rate encountered by the specimen. Typically, the time of discharge is dictated by the capacitance and inductance in the circuit and in

the present work is on the order of 50 μs. In the experiments described later, the voltage level is selected in the range of 2 to 5 kV.

2.1-2 Magnetic Field of the Solenoid

As described above, knowing the magnetic field created by the solenoid is of primary importance since this field will generate the induced current in the specimen. The magnetic field of the solenoid is then at the root of the repulsive force acting on the specimen and gives rise to the radial pressure on the specimen.

The solenoid is of the same kind as the one used by Zhang and Ravi-Chandar (2006) for their expanding ring experiments. It contains six turns ideally wound without pitch, as will be described later. This absence of pitch ideally provides a purely radial loading, which enables the specimen to stay in a same plane perpendicular to its axis while deforming. This condition is necessary for the experiment presented in this work because of the obvious reasons of focusing: the images recorded provide a basis for the experimental observations and measurements, from which theories will be compared. The recording cameras do not allow a large range of displacement of the specimen along the solenoid axis to obtain a reasonable focus. Consequently, the fact that the specimen stays in the same plane facilitates focusing the image throughout the whole experiment. Even more importantly, if the specimen moves either forward or backward while deforming, it could considerably alter our perception of its actual radial velocity, and as a result provide inaccurate estimates of the stresses and strains experienced by the specimen.

To calculate the magnetic field of this solenoid, we can then make the approximation that its six turns form a stack of six identical circular closed loops, in planes parallel to the specimen,

and whose radii are identical: r_i. At a point (r, θ, z) in the space, the general form of the magnetic field is:

$$\vec{B}^s = B_r^s(r,\theta,z)\,\overrightarrow{u_r} + B_\theta^s(r,\theta,z)\,\overrightarrow{u_\theta} + B_z^s(r,\theta,z)\,\overrightarrow{u_z} \tag{2.5}$$

This expression can be simplified, by noting that all planes containing the z-axis are an anti-symmetric planes for the current, which results in the following general form of the magnetic field:

$$\vec{B}^s = B_r^s(r,z)\,\overrightarrow{u_r} + B_z^s(r,z)\,\overrightarrow{u_z} \tag{2.6}$$

This total magnetic field produced by the solenoid is the result of the sum of magnetic fields produced by each of the 6 loops of the solenoid. We denote each of them by the index i:

$$\vec{B}^i = B_r^i(r,z_i)\,\overrightarrow{u_r} + B_z^i(r,z_i)\,\overrightarrow{u_z} \tag{2.7}$$

is the magnetic field produced by the loop i at the point (r, θ, z_i), with z_i being the distance between the center of this loop to the point, along the z-axis. Then, we have:

$$\vec{B}^s = \sum_{i=1}^{6} \vec{B}^i \tag{2.8}$$

That is:

$$B_r^s(r,z) = \sum_{i=1}^{6} B_r^i(r,z_i) \qquad and \qquad B_z^s(r,z) = \sum_{i=1}^{6} B_z^i(r,z_i) \tag{2.9}$$

The ultimate goal is to compute the magnetic flux passing through the specimen; that is, from Eq. (2.2):

$$\phi_{s\to ring} = \int_{\theta=0}^{2\pi} \int_{r=0}^{R} B_z^s(r,z)\; r\, dr\, d\theta \tag{2.10}$$

where R is the radius of the specimen. Consequently, only the z-component of the magnetic field is required. This component can be calculated with the Biot-Savart law, leading to:

$$B_z^i(r, z_i) = \frac{\mu_0 I_1(t)}{2\pi} \int_0^{\pi} \frac{r_i^2 - r_i r \cos\theta}{(r^2 - 2r_i r \cos\theta + r_i^2 + z_i^2)^{3/2}} \, d\theta \qquad (2.11)$$

where $I_1(t)$ is the current flowing through the solenoid. It can also be shown that:

$$B_z^i(r, z_i) = \frac{\mu_0 I_1(t)}{2\pi\sqrt{(r_i + r)^2 + {z_i}^2}} \left(E(k) \frac{{r_i}^2 - r^2 - {z_i}^2}{(r_i + r)^2 + {z_i}^2 - 4rr_i} + K(k) \right) \qquad (2.12)$$

with $\mu_0 = 4\pi.10^{-7}$H/m (permeability), $k = \sqrt{\frac{4rr_i}{(r_i+r)^2+{z_i}^2}}$, $K(k) = \int_0^{\pi/2} \frac{d\theta}{\sqrt{1-k^2 sin^2\theta}}$ and $E(k) = \int_0^{\pi/2} \sqrt{1 - k^2 sin^2\theta} \, d\theta$ are the elliptic integral functions of the first and second kinds. Since the specimen is placed on the central plane of the solenoid, z_i is the spatial distance between the i^{th} loop plane and the specimen plane. The total magnetic field is then computed with Eq. (2.9).

2.1-3 Coupled equations

The solenoid-specimen system can be considered as two equivalent RLC circuits coupled together according to electromagnetic laws for induction. The first circuit contains the source of the current (the capacitor bank) and the solenoid. The current flowing through it is I_1. The second circuit contains the ring specimen and its induced current is I_2. Schematics of these two circuits are shown in Figures 2.1a and 2.1b. In practice, it is possible to measure I_1 and I_2 with two Rogowski probes placed strategically in the circuit, as described later in this chapter. As shown by Zhang and Ravi-Chandar (2006) for the expanding ring experiment, writing the electrical equations for the described circuits make it possible to establish a relationship between the compressive radial velocity of the samples and the current in the circuit.

For the first circuit, Kirchhoff voltage law gives:

$$C\frac{dV}{dt} = I_1$$

$$V + R_1 I_1 + L_{11}\frac{dI_1}{dt} + \frac{d(L_{12}I_2)}{dt} = 0 \tag{2.13}$$

where C is the capacitance, R_1 is the resistance of the solenoid circuit, L_{11} is the self-inductance of the solenoid, L_{12} is the mutual inductance between the solenoid and the ring specimen and V is the applied discharge voltage. Note that since the specimen is deforming during the experiment, the mutual inductance L_{12} varies with time. Consequently it has to be differentiated with time together with I_2 to obtain the electromotive force induced through circuit 1 by the magnetic field of the ring: indeed by definition of L_{12} we have: $EMF_{2\to1} = -\frac{d\phi_{2\to1}}{dt} = -\frac{d(L_{12}I_2)}{dt}$. This is not the case for the self-inductance of the solenoid: L_{11} is a constant with respect to time.

For the second circuit we have:

$$R_2 I_2 + \frac{d(L_{22}I_2)}{dt} + \frac{d(L_{12}I_1)}{dt} = 0 \tag{2.14}$$

where R_2 and L_{22} are the resistance and the self-inductance of the ring respectively. Again, L_{22} changes with time in line with the change of the radius of the specimen $r(t)$. Notably, we can write: $\frac{dL_{\alpha 2}}{dt} = \dot{r}\frac{dL_{\alpha 2}}{dr}$, with $\alpha = 1, 2$. The following relations can be derived from (2.13) and (2.14):

$$\ddot{I_1} = -\frac{R_1}{L_{11}}\dot{I_1} - \frac{L_{12}}{L_{11}}\ddot{I_2} - \frac{2\dot{I_2}\dot{r} + I_2\ddot{r}}{L_{11}}\frac{dL_{12}}{dr} - \frac{I_2\dot{r}^2}{L_{11}}\frac{d^2L_{12}}{dr^2} - \frac{I_1}{L_{11}C} \tag{2.15}$$

$$\dot{I_2} = -\frac{R_2}{L_{22}}I_2 - \frac{L_{12}}{L_{22}}\dot{I_1} - \frac{I_1\dot{r}}{L_{22}}\frac{dL_{12}}{dr} - \frac{I_2\dot{r}}{L_{22}}\frac{dL_{22}}{dr} \tag{2.16}$$

From these two equations, it can be noticed that, although (2.15) is a complicated differential equation in r involving $\dot{r}$, $\ddot{r}$, $\dot{r}^2$, Eq. (2.16) involves $\dot{r}$ together with r. As $\dot{I_1}$ and $\dot{I_2}$ are given by

the Rogowski coils, L_{12} and L_{22} have to be determined in terms of r in order to give a reasonable solution to (2.16). The ring specimen self-inductance can be computed with (AIP, 1972):

$$L_{22} \approx \mu_0 r \left(\left(1 + \frac{r_w^2}{8r^2} \right) \ln \frac{8r}{r_w} + \frac{r_w^2}{24r^2} - 7/4 \right)$$

where $r_w = \sqrt{\frac{A}{\pi}}$ is the area-equivalent cross-section radius of the ring. For the tests performed in this thesis it can be considered that $\frac{r_w}{r} < 0.1$, which results in the following approximation (AIP, 1972):

$$L_{22} \approx \mu_0 r \left(\ln \frac{8r}{r_w} - \frac{7}{4} \right) \tag{2.17}$$

Figure 2.3 shows the plot of L_{22} as a function of r. The mutual inductance L_{12} can be calculated by differentiating the following relation: $L_{12} I_1 = \int_{\theta=0}^{2\pi} \int_0^r B_z^s(r,z)\, r dr d\theta = 2\pi \int_0^r B_z^s(r,z)\, r dr$ leading to:

$$\frac{dL_{12}}{dr} = 2\pi r b_z^s(r,z) = 2\pi r \sum_{i=1}^{6} b_z^i(r,z)$$

$$= \mu_0 r \sum_{i=1}^{6} \int_0^{\pi} \frac{r_i^2 - r_i r \cos\theta}{(r^2 - 2 r_i r \cos\theta + r_i^2 + z_i^2)^{3/2}}\, d\theta \tag{2.18}$$

where the lower case b represents the magnetic field divided by the current. Figure 2.2 shows the plot of L_{12} as a function of r.

2.1-4 Equation of motion

After Zhang and Ravi-Chandar (2006), the equation of motion can be determined from energy considerations. The energy of the system is composed of: the energy provided by the capacitor $\frac{1}{2} C V^2$, the energy dissipated in both resistors $\int_0^t (R_1 I_1^2 + R_2 I_2^2) dt$, the electromagnetic

stored energy $\frac{1}{2}\sum_{i,j=1}^{2} L_{ij} I_i I_j$, the kinetic energy of the ring specimen $\frac{1}{2} M \dot{r}^2$ where M is its mass and finally the mechanical work done on the specimen $\int_0^t 2\pi A \dot{r} \sigma(\epsilon) dt$ with A being the cross-section area and $\sigma(\epsilon)$ the constitutive law of the material of the ring. The total energy of the system is then:

$$W = \frac{1}{2} C V^2 + \int_0^t (R_1 I_1^2 + R_2 I_2^2) dt + \frac{1}{2} \sum_{i,j=1}^{2} L_{ij} I_i I_j + \frac{1}{2} M \dot{r}^2 + \int_0^t 2\pi A \dot{r} \sigma(\epsilon) dt \quad (2.19)$$

Letting $dW = 0$ and recalling Eqs. (2.15) and (2.16), we obtain the acceleration of the expanding ring, constituting the equation of motion:

$$\ddot{r} = \frac{I_1 I_2}{2\pi r A \rho} \frac{dL_{12}}{dr} + \frac{I_2^2}{4\pi r A \rho} \frac{dL_{22}}{dr} - \frac{\sigma}{\rho r} \quad (2.20)$$

In practice, the radial displacement r of the specimen can be measured from each frame taken by the camera. Typically, if the camera is adjusted so that it can take 150,000 frames per second, a frame will be recorded every 6.7 µs, meaning that $r(t = 6.7n)$ can be measured for $n \in \{0, 1, 2 \ldots\}$. Then the radial velocity $\dot{r}(t)$ can be computed from Eq. (2.16) using interpolation of the discretized radius measured. Finally, $\ddot{r}$ is determined and (2.20) is used to compute the stress σ encounters by the specimen.

2.2 Manufacture of the solenoid

Special care is needed while manufacturing the solenoid. Indeed, as indicated previously, any pitch in the coil turns should be avoided as much as possible. This way, the ring specimen will deform within its own plane, perpendicular to the axis of the solenoid. Moreover, Zhang and Ravi-Chandar (2006) have shown that 6 turns should be wound to constitute the solenoid, in

order to achieve a reasonably high driving efficiency. The coil manufacturing procedure consists of multiple steps. Figures 2.4a, 2.4b and 2.4c illustrate the three steps of this process. First a polycarbonate cylinder of diameter 2 in is chosen. In this cylinder, six grooves are machined perpendicularly to its longitudinal axis, deepening from the surface; this will ensure a coil winding with no pitch. The dimensions of the grooves are 0.06 in for both width and depth and the space between two grooves is 0.05 in. Another groove is machined but in the longitudinal direction so that it crosses the six hoop grooves. Its function is to provide enough space to wind the copper wire from one groove from another. The width of this longitudinal groove is taken as 0.2 in but can be either reduced or enlarged, depending on the room needed to turn the copper coil. The next step is to simply wind the coil around the grooves. The coil used is a 16-gauge square cross-section magnet wire made of copper. The most important thing for this step is to make sure that the so-wound wire stays in place in the grooves. To ensure its immobilization during the whole process of winding, the wire can be wedged and stuck with glue at selected points, for example at the end of each turn made. Figure 2.5 shows the copper coil wound around the polycarbonate cylinder. When the winding is finished and the coil is in place, the coil is placed in a container and filled with an epoxy resin solution. Once the epoxy has cured, it plays the dual role of holding the loops together within the polycarbonate cylinder and avoiding electrical arcing between the windings.

Epoxy is a thermosetting polymer formed from the reaction of an epoxide resin with a polyamide hardener. When these two compounds are mixed together, a chemical reaction takes place between the amine groups of the hardener and the epoxide groups of the resin. Covalent bonds are then formed during this reaction, called polymerization or curing. During this process, each amide group can react with an epoxide group, resulting in a heavily cross-linked polymer.

The time needed to cure the polymer depends on the type of epoxy used, on the surrounding temperature and depends also on the ratio resin/hardener mixed. While curing, the polymer hardens more and more, resulting in a completely solid and rigid form.

For the manufacture of the solenoid, it is extremely important to avoid bubbles in the epoxy. Indeed, bubbles are air pockets and thus constitute a more electro-conductive medium than epoxy, allowing possible arcing between adjacent coil loops. The compounds used for making the solenoid are EpoxiCure® Epoxy Hardener 20-8132-032 and EpoxiCure® Epoxy Resin 20-8130-128 from the Buehler brand. The ratio by weight of these compounds is 5 parts of resin for 1 part of hardener. A mixing time of at least 2 minutes was used. A stick is used to gently work the resin and hardener together, in a lift and tilt motion until the mixture is thoroughly blended. The mixture is then placed under vacuum for a few minutes to extract any bubbles left over from the mixing procedure. The mixture is then poured into the mold, as previously described, and allowed to cure around the wound coil for at least 6 hours.

After it has cured, the entire assembly is machined to the right final dimensions, preserving the axial alignment of the coil windings. The inner diameter of the solenoid is drilled such that the ring specimen can be placed inside the coil. The outer surface must be shaped at a diameter leaving enough epoxy to maintain the coil in place when high voltages are applied, without breaking the assembly. Indeed, the coil will encounter repulsive forces that will make it want to expand as discharge voltages are high. Finally, electrical insulation must be added to the exposed leads and lugs are soldered at their tips, allowing their connection to the capacitor bank. Figure 2.6 shows the solenoid finished and in place for the experiments.

2.3 Characteristics of the specimens

2.3-1 General characteristics

The specimens used during the experiments presented in this thesis are made of Al 6061 alloy. The major alloying elements of Al 6061 are magnesium and silicon. The ranges of weight percentage for these two elements are 0.8 % – 1.2% and 0.4% – 0.8% respectively. Al 6061 is one of the most commonly aluminum alloy used for general purpose.

Annealed rings (Al 6061-O) have been used for the experiments. In order to make sure that the Al 6061 specimens used were effectively annealed, a heat treatment has been conducted on the specimens. The annealing procedure is the following:

- The specimens are placed in the furnace
- The furnace is heated up to 760°F and kept at this temperature for 3 hours
- The furnace is cooled 50°F per hour down to 500°F
- At 500°F, the oven is turned off and the samples are allowed to cool down to room temperature before removing them from the furnace.

The aim of this annealing process is to remove the precipitates and obtain a homogeneous microstructure. It can be noticed that the melting temperature of aluminum is about 1220°F and is never reached during the annealing process. The resulting material, Al 6061-O has a very low yield strength and a high strain-hardening response.

The typical ring specimen has an external diameter of 31.5 mm. The solenoid previously described is designed with a sliding fit tolerance for the rings. This means that the internal diameter of the solenoid equals the external diameter of the ring plus some very small value. The rings are 0.5 mm thick, meaning that their internal radii are 15.25 mm, or that their mean radii are 15.5 mm; therefore the R/t ratio is ~30. The width of the rings is of 1 mm.

Experience has shown that the original grainy gray color of aluminum does not allow proper light reflection for the camera to display a well contrasted image. The result is a lack of precision in the measurements and analysis from the images. The trick to obtaining good images consists in reversing the white and black colors by painting the rings black on their front and inside surfaces so that no light is reflected at all. Moreover, a white background is added at the back-end of the solenoid. This white sheet reflects the light coming from the flash lamps, displaying a shadow of the specimen. This way, a better contrast is obtained when recording images with the camera and edges of the rings can be detected more precisely.

Figure 2.7 shows pictures of the ring specimen. Figure 2.8 shows the specimen inside the solenoid and ready for an experiment.

2.3-2 Mechanical behavior

The mechanical behavior of this annealed Al 6061-O is taken as follows. The stress-strain curve shows first an elastic region with the following material characteristics:

- Young's modulus: E = 70 MPa
- Poisson's ratio: ν = 0.33

The plastic response of Al 6061-O was investigated by Ravi-Chandar and Zhang (2006) through uniaxial tensile tests. It has been shown that the constitutive law of this material can be approximated by a power law of the form:

$$\sigma = \sigma_y\left(1 + \beta\varepsilon_p\right)^n \tag{2.21}$$

where the parameters are obtained by fitting to the experimental results: σ_y = 25 MPa, β = 14165 and n = 0.22. σ and ε_p represent the true stress and the logarithmic strain respectively. This

power law response is shown in Figure 2.9. In the finite element analysis performed with ABAQUS, this constitutive law is used to describe the mechanical behavior of this material.

2.4 Images recording

2.4-1 Camera characteristics

In order to track the radial compression and buckling of the rings, a Cordin Model 550-30 high speed camera was used. This camera consists of a high-speed rotating mirror system coupled with a CCD (Charged-Couple Device) based digital imaging. In this camera, the mirror spins at a maximum speed of 2,500 rps using an electric drive, leading to a maximum framing rate of 400,000 frames per second. This rate is adjustable directly on the software that controls the camera. In the experiments performed, a rate of around f = 150,000 fps was used. The exposure time at this rate is $1/f$, resulting in long exposures and image blur, especially when the ring moves at high speeds. Light enters the camera through the objective and internal field lenses and is reflected by the spinning mirror directly to the CCD sensor. The CCD Device used in this camera is a Kodak KAI-1020. A CCD sensor is made of a silicon chip on which an array of photoelectric detectors is etched. Each of these detectors corresponds to a pixel. The sensor used has a spatial resolution of 1000 x 1000 pixels and its gain is also adjustable directly on the controlling software. The camera is capable of recording 30 frames in these conditions.

Special timing and lighting equipment are required since the camera records for a relatively short period of time. In order to illuminate the sample, two xenon flash lamps, Model 605 from Cordin were used. In the single flash mode, the duration of the flash, called pulse duration, as well as the level of charge voltage can be adjusted. In the experiments performed, a pulse duration of 0.1 ms and a charge voltage of 7 kV were used.

2.4-2 Trigger Sequence

It takes about 300 μs for the flash lamps to reach the charging level once it has been triggered. Therefore, in order to capture images in an optimized way, a special trigger sequence has to be set and delays have to be established between the different triggers for the flash lamps, for the discharge from the capacitor bank and for capturing the images by the high-speed camera. These are accomplished with 565 series pulse generator from Berkley Nucleonics Corp. This pulse generator is triggered by a simple switch button that generates a 5 V pulse when pressed. This corresponds to time t = 0; the pulse generator then generates the following pulses in sequence on four channels:

- Channels B and C send a TTL signal immediately at t = 0 to the two Cordin flash lamps which rise up to full intensity in about 300 μs
- Channel D send a TTL signal at t = 300 μs to the Cordin Camera which starts capturing the images
- Channel A sends a TTL signal at t = 335 μs to the thyratron-ignitron firing circuit for the capacitor discharge.

These delays enable the flash lamps to reach their full intensity level when the camera begins to capture the images and to discharge the capacitor during the time interval when the images are acquired.

2.5 Capacitor Bank

2.5-1 Characteristics of the capacitor circuit

The circuit used to produce the current $I_1(t)$ in the solenoid consists in a 25 μF capacitor with a maximum voltage charge of 20 kV. The switching of the circuit is performed by using a thyratron-ignitron circuit that is synchronized with the data recording system as described before (triggered at time t = 335 μs). In the experiments, voltage levels between 2 kV to 5 kV are used. The energy stored in the capacitor bank is given by:

$$E_v = \frac{1}{2} C V^2 \tag{2.22}$$

where V is the voltage charge and C is the capacitance (C = 25 μF). Therefore, a charge of 2 kV gives E_v = 50 J and for a charge of 5 kV we have E_v = 312.5 J.

Figure 2.10 is a picture of the general arrangement of the experiment showing the solenoid, the capacitor bank, the flash lamp and the camera.

2.5-2 Measurement of the current

The current flowing through the main circuit due to the capacitor discharge is measured using a Rogowski probe. This probe is looped around the wire connecting the capacitor to the solenoid. The voltage V_R produced by a Rogowski coil is proportional to the derivative of the current going through it:

$$V_R = \frac{1}{K_R} \frac{dI_1}{dt} \tag{2.23}$$

where K_R is the Rogowski constant depending on the coil (known from calibration). Therefore, as V_R and K_R are known, I_1 can be computed. The current I_2 in the secondary circuit can be found also using another Rogowski probe. Indeed, if we loop this probe around both the solenoid and

the sample, it will respond to a total current of: $I = n\, I_1 + I_2$, where n is the number of turns in the solenoid ($n \approx 6$). Therefore, by knowing I and I_1 (previously calculated), I_2 can be obtained. This second Rogowski probe has a constant K_R different from the first instrument used. In the experiments performed, the Rogowski coils used have the following calibration constants:

- $K_R \approx 36705779.05\ \Omega^{-1}s^{-1}$ to measure I_1
- $K_R \approx 35141592.43\ \Omega^{-1}s^{-1}$ to measure I

Another way to measure I_2 is to refer to Eq. (2.16). From this equation, once I_1 is known, every other term can be computed with respect to r. From the experiments performed, $r(t)$ is determined for certain values of t after analysis of the pictures taken by the camera: r is then known as a discrete function of time. These discrete values are approximated with a best fit polynomial within a certain range of time. Once r is obtained as a continuous function of time, the inductances L_{12} and L_{22} are derived via, for example, MATLAB. R_2 being known, the derivative $\dot{I_2}$ is then computed, and I_2 is finally obtained. It is not necessary to use a second Rogowski coil for this method.

CHAPTER 3: BUCKLING RING EXPERIMENTS

In this chapter we describe and analyze the twelve dynamic buckling experiments that have been conducted with Al 6061-O. Experimental results are presented and comparisons are made with respect to the theories shown in Chapter 4. All of the specimens have R/t ratios of approximately 31, for a width of 1mm. The buckling behavior of the rings is influenced by the applied pressure and several different buckling modes appear on the deformed ring shape. This will be illustrated by discussing in detail the results of these experiments performed with charge levels of 2 kV, 3 kV, 4 kV and 5 kV.

The results include selected sets of images from the digital high-speed camera. Graphs presenting the applied pressure on the rings for the different set of charged voltages are also shown, as well as the calculated impulses corresponding to the onset of buckling.

3.1 Experimental results

3.1-1 Charge voltage of 2 kV

A first set of three experiments was conducted with a charge voltage of 2 kV. For each of these three tests, the rate of change of current $\dot{I}_1$ in the main circuit was monitored with a Rogowski probe and recorded with an oscilloscope as described in Chapter 2. The current I_2 was calculated from Eq. (2.16) once the evolution of the radius was measured from the pictures obtained with the high-speed camera. Figure 3.1 shows the plots of these two currents for a 2 kV discharge. They are plotted over a period of 100 μs, with t = 0 corresponding to the external trigger button. A short delay of the order of 3 μs is observed before the capacitor actually discharges, giving rise to I_1. This is caused by internal delays in both the ignitron box and the

capacitor circuit. Afterwards, I_1 follows a sinusoidal curve with a first positive peak at about 20 µs. Its maximum magnitude is in the order of 5200 A. The current I_2 exhibits first a negative peak of amplitude –6500 A at about 14 µs. I_1 and I_2 have opposite signs until 28 µs, when I_2 becomes positive to present an even higher peak in amplitude at 45 µs: 8200 A. Then, I_1 and I_2 have the same sign from 28 µs to 37.5 µs, when I_1 becomes negative, which results in a pressure directed outwards of the ring.

From these two currents in the main circuit and in the ring, the magnetic load encountered by the ring during its deformation can be computed using Eq. (2.20). The pressure is found to be:

$$p = \rho\, t \left(\frac{I_1 I_2}{2\pi r A \rho} \frac{dL_{12}}{dr} + \frac{I_2^2}{4\pi r A \rho} \frac{dL_{22}}{dr} \right) \tag{3.1}$$

where t = 0.5 mm is the width of the ring. The dependence of L_{12} and L_{22} on r are shown in Figures 2.2 and 2.3. The graph of the pressure for a test performed with a 2 kV charge is shown in Figure 3.2. The pressure is taken positive when directed inwards. This load exhibits a positive peak of magnitude 7.6 MPa at 17 µs, a negative wave with amplitude of –2.6 MPa and finally another high positive peak of 7.4 MPa.

The impulse corresponding to this pressure is given by the following definition:

$$\mathcal{I} = \int_0^t p\, dt \tag{3.2}$$

This impulse is shown in Figure 3.3 and will be used in estimating an analogy with the theory for which only impulse loads are considered. Notably, the graph shows a first local maximum in the impulse at about 28 µs, corresponding to an amplitude of 105 Pa.s.

A set of pictures taken at different times during the buckling of the rings is shown in Figure 3.4. For these tests, the camera ran at around 150,000 frames per second, meaning that a frame is taken at about every 6.7 μs. A more precise framing time can be seen in Figure 3.5 where the rising edge of the square signal is when for the camera actually takes a picture. From these images, several analyses can be made. First, the time at the onset of buckling, called t_0, can be approximated and the corresponding impulses are found. It is shown that t_0 lies between 40 and 50 μs. This relatively large span can be explained by the approximation of the time measuring technique. Indeed, the result is known with a precision equivalent to the framing rate: 6.7 μs. The corresponding impulses lie within the range 90 – 130 Pa.s. Table 1 summarizes the buckling times and impulses for the different experiments performed.

Secondly, the radial compression of the ring is measured. The method is as follows: using a code written on MATLAB (Appendix), several points (generally around 50) are selected along the edge of the ring. From these points, a best fit circle is computed using the least square method. An example of this method is shown in Figure 3.6. The radius of this best-fit circle is then plotted as a function of time and can be seen in Figure 3.7. The ring does not move before about 25 – 30 μs. Then a uniform axisymmetric motion of the ring is observed before buckling occurs: the radius decreases with a nearly constant slope. This slope gives the radial speed of the specimen: ~ –40 m/s. At the onset of buckling, the radius of the ring has reached a value around 14.9 mm. Finally, the radius continues to decrease, as the ring continues to buckle, until it reaches about 14.7 mm at the last recorded frame. It can be observed from Figure 3.7 that the radial velocity is nearly zero at this point and that the ring does not deform further: indeed, the specimens recovered after the test confirm that the deformation ceases after this stage.

The hoop strain can be calculated during the entire uniform axisymmetric deformation of the ring with the following formula:

$$\varepsilon(t) = \ln\left(\frac{r(t)}{r_0}\right) \tag{3.3}$$

where $r(t)$ is the radius at time t and r_0 = 15.5 mm is the initial radius. This formula, used during the uniform deformation of the ring, can be extrapolated to compute an "average" strain for after buckling has occurred: graphs of such averaged hoop strain are also shown in Figure 3.7 through the secondary axis. Buckling is visible in the images at a compressive strain level between 3.7 % and 4.2 %.

From the pictures taken by the camera, the different buckling waves are identified as shown in Figure 3.8. These waves have different wave lengths and correspond to different mode numbers. These mode numbers can be computed easily as follows. The center $(x_C; y_C)$ of the best-fit circle is known; at a certain time t, the i-th wave is defined between two points $(x_1; y_1)$ and $(x_2; y_2)$ on the ring, forming an angle $\theta_i(t)$ from the center of the circle. This angle is calculated with the following formula:

$$\theta_i(t) = \arcsin\left(\frac{y_2 - y_C}{\sqrt{(y_2 - y_C)^2 + (x_2 - x_C)^2}}\right) - \arcsin\left(\frac{y_1 - y_C}{\sqrt{(y_1 - y_C)^2 + (x_1 - x_C)^2}}\right) \tag{3.4}$$

Consequently, the apparent mode number can be computed as:

$$n_i(t) = \frac{2\pi}{\theta_i(t)} \tag{3.5}$$

Figure 3.8 shows an overlay of several pictures from one experiment with the numbering of the positions studied. Table 2 summarizes the mode numbers at these positions with respect to time. Several observations can be made. First, the largest mode is found to be 24, corresponding to a wave length $\lambda \approx 4$ mm. The smallest mode is $n = 3$, corresponding to $\lambda \approx 32.4$ mm. Secondly, n_i

does not vary much with time within experimental uncertainty. This means that, as the ring deforms, the waves stay respectively in a certain angular sector. As the radius reduces, the waves compress even more and keep the mode number that they selected at their onset.

Finally, Figure 3.9 shows pictures of the post-mortem rings for the second and the third experiments performed with a 2 kV charge voltage. Non-planar deformation is observed, but this appears later in the deformation of the rings due to slight asymmetries in the solenoid.

3.1-2 Charge voltage of 3 kV

A set of three experiments was conducted with a charge level of 3 kV. The current I_1 was measured with a Rogowski probe and I_2 was computed as described earlier. We can observe in Figure 3.10 that these two currents I_1 and I_2 have the same form as those for the 2 kV charge level, but of course have different magnitudes. For example, the maximum of I_1 was 7500 A. I_2 had a first peak of –9400 A, is zero at 24.5 μs and has a positive maximum amplitude of 11200 A around 40 μs.

The corresponding pressure can be seen in Figure 3.11. It exhibits the same shape as the one described for the 2 kV charge voltage, but now with a positive peak of 15.7 MPa followed by a negative wave with –5.6 MPa amplitude, and finally a second positive peak of 14 MPa. The resulting impulse encountered by the rings can be seen in Figure 3.12. The first local maximum of this impulse occurs at 26 μs and has a value of 210 Pa.s.

The pictures taken during the buckling of the rings are shown in Figure 3.13. The camera ran at 150,000 frames per second: a frame is taken at about every 6.7 μs. The analyses of these pictures are the following. First, the time t_0 at the onset of buckling lies between 27 and 38 μs.

The corresponding impulses are within the range 170 – 210 Pa.s. Table 1 gives a summary of the buckling times and impulses for the different experiments performed.

Secondly, the radial compression of the ring is measured using the method described earlier. The radius of the best-fit circle is plotted as a function of time in Figure 3.14. The ring does not move before about 20 – 25 μs. Then a uniform axisymmetric motion of the ring is observed before buckling occurs: the radius decreases with a constant slope: this slope gives the radial speed of the specimen: ~ –85 m/s. We can observe that the speed of the rings decreases as it approaches the critical point for buckling. At the onset of buckling, the radius of the ring has reached a value around 14.8 mm. Finally, the ring continues to buckle and, contrary to the case of a 2 kV charge voltage, the best-fit radius does not reach a limit. Even if the speed decreases slightly, the rings collapse completely, as one can see in the pictures of the post-mortem specimen, Figure 3.15. The calculated "average" hoop strain is shown in Figure 3.14 as a secondary axis. Buckling occurs at a compressive strain between 3.4 % and 4.4 %. Note that in the third experiment performed with a 3 kV charge voltage, the –7.1 % hoop strain measured corresponds to a picture were buckling is already well discernible, but the frame before it was missing in the camera recording. If we take the average between this frame and the last frame where buckling is not observable a strain of –4.38 % is found.

The different buckling waves are identified on the high speed images as shown in Figure 3.16. Table 3 summarizes the mode numbers of these waves with respect to time. Several observations can be made. First, the highest mode is found to be 34, corresponding to a wave length $\lambda \approx 2.8$ mm. The smallest is $n = 13$, corresponding to $\lambda \approx 7.5$ mm. Secondly, just as we observed for the case of a 2 kV charge voltage, n_i does not vary with time. This means that, as the ring deforms, the waves stay respectively in a certain angular sector. As the radius reduces,

the waves compress even more and keep the mode number that they selected at the onset of bukling.

3.1-3 Charge voltage of 4 kV

A set of three experiments was conducted with a charge voltage of 4 kV. The recorded current I_1 and the computed I_2 can be observed in Figure 3.17. The current follows the same shape as for the 2 kV and 3 kV charge levels. This time, the maximum of I_1 was 9500 A. I_2 first had a negative peak of –11900 A, was zero at 23.5 μs and had a positive maximum amplitude of 11500 A around 40 μs.

The corresponding pressure can be seen in Figure 3.18. The magnitude of the first positive peak is between 25 MPa and 25.7 MPa. It is followed by a negative wave whose amplitude is in the range –12 MPa / –13 MPa, and finally a second positive peak of about 19.5 MPa. The resulting impulse encountered by the rings can be seen in Figure 3.19. The first local maximum of this impulse occurs at 26 μs and has a value between 300 Pa.s and 330 Pa.s.

The pictures taken during the buckling of the rings are shown in Figures 3.20. The camera ran at 150,000 frames per second, meaning that a frame is taken about every 6.7 μs. From these pictures, several observations can be made. First, the time t_0 at the onset of buckling lies between 23.7 and 25 μs. The corresponding impulses are within the range 300 – 330 Pa.s. Table 1 gives a summary of the buckling times and impulses for the different experiments performed.

Secondly, the radial compression of the ring is measured using the method described earlier. The radius of the best-fit circle is plotted as a function of time in Figure 3.21. The ring did not move before about 12 – 17 μs. Then a uniform axisymmetric motion of the ring was observed before buckling occurred: the radius decreased with a constant slope. This slope gives

the radial speed of the specimen: ~ –140 m/s. We can observe that the speed of the rings slows down as it approaches the critical point for buckling. At the onset of buckling, the radius of the ring has reached a value around 14.7 mm. Finally, the radius continued to decrease, as the ring continues to buckle and, comparable to the case of a 3 kV charge voltage, the best-fit radius does not reach a limit. Even if the speed does reduce slightly, the rings collapse completely, as shown in the pictures of the post-mortem specimen, Figure 3.22. The "average" hoop strain is shown in Figure 3.21 as the secondary axis. Buckling becomes visible at a compressive strain around 4.5 %.

The different buckling waves are identified in the pictures taken by the camera. The numbering of the waves that were studied is shown in Figure 3.23. Table 4 summarizes the mode numbers of these waves with respect to time. Several observations can be made. First, the highest mode was found to be 31 in our experiments, corresponding to a wave length $\lambda \approx 3.1$ mm. The smallest was $n = 19$, corresponding to $\lambda \approx 5.1$ mm. Secondly, as we observed in the previous cases, n_i does not vary with time. The same conclusion can be drawn: each wave stays in a certain angular sector and as the radius reduces, the waves compress even more and keep the mode numbers that were selected at the onset of buckling.

3.1-4 Charge voltage of 5 kV

A final set of 3 experiments was conducted with a charge voltage of 5 kV. The recorded current I_1 and the computed I_2 can be observed in Figure 3.24. These two currents followed the same shapes as for the other charge voltages. The maximum value of I_1 increased to 11700 A. I_2 had first a negative peak of –14800 A, was zero around 25 μs and had a positive maximum amplitude of 17000 A around 40 μs.

The corresponding pressure can be seen in Figure 3.25. The magnitude of the first positive peak is around 38 MPa. It is followed by a negative wave whose amplitude is –13.5 MPa, and finally a second positive peak of about 32.7 MPa. The resulting impulse encountered by the rings can be seen in Figure 3.26. The first local maximum of this impulse occurs at 26 μs and has a value of 530 Pa.s.

The pictures taken during the buckling of the rings are shown in Figure 3.27. The camera ran at 150,000 frames per second for the first experiment (a frame is taken about every 6.7 μs), 200,000 frames per second for the second experiment (a frame is taken about every 5 μs) and finally 230,000 frames per second for the third test (a frame is taken about every 4.35 μs). Increasing the speed of the camera helps in gaining precision in the measurements, obtaining clearer images, especially for this level of charge where the radial speed of the specimen is high. From these pictures, several observations can be made. First, the time t_0 at the onset of buckling lies between 17 and 26 μs. The corresponding impulses are within the range 420 – 500 Pa.s. Table 1 gives a summary of the buckling times and impulses for the different experiments performed.

Secondly, the radial compression of the ring is measured using the method described earlier. The radius of the best-fit circle is plotted as a function of time in Figure 3.28. The ring does not move before about 8 – 13 μs. Then a uniform axisymmetric motion of the ring is observed before buckling occurs: the radius decreases with a constant slope. This slope gives the radial speed of the specimen: ~ –220 m/s. We can observe that the speed of the rings decreased as it approached the critical point for buckling. At the onset of buckling, the radius of the ring reached a value around 14.2 mm. Finally, the radius continues to decrease, as the ring continues to buckle and, comparable to the 3 kV and 4 kV charge levels, the best fit radius does not reach a

limit. Even though the speed decreased slightly, the rings collapse completely, as the pictures of the post-mortem specimen demonstrate in Figure 3.29. The calculated "average" hoop strain is shown in Figure 3.28 as the secondary axis. Buckling becomes visible at a compressive strain around 8.6 %. Note that the value of –12.28 % found for the hoop strain in the first experiment is aberrant: the low speed of the camera compared to the speed of the specimen made it produce blurred images while buckling was occurring. More important, it did not furnish enough pictures to be able to track the phenomenon correctly.

The different buckling waves are numbered on the pictures taken by the camera, as previously explained. The numbering of the studied waves is shown in Figure 3.30. Table 5 summarizes the mode numbers of these waves. For most of the waves identified, we were not able to track the same wave at different times. This is due to the fact that the rings were moving too quickly for the camera to properly capture buckling. The resulting blurred images made it difficult to discern the waves. Only three waves were measured at two different times for the third experiment performed at the 5 kV charge level, thanks to the increased speed of the camera which had been set at about 230,000 frames per second for this last test. Several observations can be made. First, the highest mode was found to be 44 in our experiments, corresponding to a wave length $\lambda \approx 2.2$ mm. The smallest was $n = 20$, corresponding to $\lambda \approx 4.9$ mm. Secondly, we observed that many more waves were discernible on the shape of the ring for this 5 kV charge level than for the other experiments: from 7 to as high as 14 waves were observed in each of these three experiments whereas around 5 waves were typically observed for the experiments performed with lower charge levels. In terms of occurrence, a large number of n_i appear to lie within the range 28 – 35. In a total of 28 waves identified of these three experiments, 15 of them corresponded to mode numbers between 30 and 35. Finally, from the three waves that we were

able to measure at two different times, we can notice that the apparent mode number they developed does not change much with time. The following conclusion can then be drawn: each wave stays in a certain angular sector and as the radius reduces, the waves compress even more and maintain the wave lengths that were selected at their onset.

CHAPTER 4: BUCKLING OF CIRCULAR RINGS

This chapter describes analytical and numerical methods for the analysis of the buckling of circular rings. The first method is based on the work of Timoshenko (1936) on the theory of elastic buckling for rings. The analyses by Lindberg and Florence (1987) as well as Jones (1989) on dynamic plastic buckling are also presented. Finally, the results obtained using the finite element code ABAQUS are shown.

4.1 Analytical Method

The analytical calculations are based on the theories developed by Lindberg and Florence (1987) and by Jones (1989) of plastic buckling of rings under dynamic radial loading. The theory of elastic buckling described by Timoshenko (1936) and Brush and Almroth (1975) are presented first because of their interest as starting points for the problem and for selecting parameters.

4.1-1 Elastic Buckling Analysis

The elastic behavior of the material is considered, with E denoting the elastic or Young's modulus. In order to derive the differential equation for the deflection of the ring, we consider first a curved bar $\{A-B\}$ represented in Figure 4.1a. If we define R and ρ as the initial and post-deformation radii of curvature of the center line of the bar, the bending moment in this portion $\{A-B\}$ is then given by:

$$M = -EI\left(\frac{1}{\rho} - \frac{1}{R}\right) \tag{4.1}$$

where I is the second moment of the cross-sectional area of the ring. The initial length of a small element $\{mn\}$ is:

$$ds = R\, d\theta \tag{4.2}$$

To compute the curvature ρ after deformation, we consider that the point m will move radially toward the center by an amount w (positive when directed this way) and we assume that the displacement in the tangential direction is negligible. Finally, we consider that the element $\{mn\}$ deforms as $\{m_1 n_1\}$ and both arcs have the same curvature. Under these conditions, the curvature after deformation is given by:

$$\frac{1}{\rho} = \frac{d\theta + \Delta d\theta}{ds + \Delta ds} \tag{4.3}$$

where $d\theta + \Delta d\theta$ denotes the angle between the normal cross sections m_1 and n_1 of the deformed bar and $ds + \Delta ds$ is the length of the element $\{m_1 n_1\}$. Considering Figure 4.1b, it can be shown that:

$$\Delta d\theta = \frac{d^2 w}{ds^2} ds \quad and \quad \Delta ds = -w d\theta = -\frac{w ds}{R} \tag{4.4}$$

Substituting (4.4) in (4.3) and neglecting higher order terms, the curvature after deformation is then:

$$\frac{1}{\rho} = \frac{1}{R}\left(1 + \frac{w}{R}\right) + \frac{d^2 w}{ds^2} \tag{4.5}$$

Finally, substituting (4.2) and (4.5) in (4.1) we obtain the following differential equation for the deflection curve of a thin bar with a circular center line:

$$\frac{d^2 w}{d\theta^2} + w = -\frac{MR^2}{EI} \tag{4.6}$$

To determine the moment M corresponding to a ring subjected to a uniform pressure, we consider Figure 4.2, where half of this ring is shown. Let p denote the uniform normal pressure per unit length of the center line of the ring and w_0 the radial displacement of points A and B. Considering that the action of the hidden half of the ring on the displayed half is represented in A and B by a compression S and by a moment M_0, it can be shown that:

$$S = p\,(R - w_0) \tag{4.7}$$

and:

$$M = M_0 - pR\,(w_0 - w) \tag{4.8}$$

Eq. (4.6) for the deflection then becomes:

$$\frac{d^2w}{d\theta^2} + w\left(1 + \frac{pR^3}{EI}\right) = \frac{-M_0R^2 + pR^3w_0}{EI} \tag{4.9}$$

This leads to the general solution for this differential equation for $w(\theta)$:

$$w = A_1 \sin(k\theta) + A_2 \cos(k\theta) + \frac{-M_0R^2 + pR^3w_0}{EI + pR^3} \tag{4.10}$$

with:

$$k^2 = 1 + \frac{pR^3}{EI} \tag{4.11}$$

Moreover, horizontal and vertical symmetries of the ring give: $\left(\frac{dw}{d\theta}\right)_{\theta=0} = 0$ and $\left(\frac{dw}{d\theta}\right)_{\theta=\frac{\pi}{2}} = 0$, which yield $A_1 = 0$ for the first condition and $\sin\left(\frac{k\pi}{2}\right) = 0$ for the second. For this last condition to be satisfied, k must be an even integer: $k = 2n$ with $n = 1, 2, 3$ .... However, if only one axis is considered as an axis of symmetry, which is a less restrictive limitation for the buckled shape, it is found that k has to be an odd integer: $k = 2n - 1$. The case $k = 1$ represents a rigid body

translation and is therefore not discussed. Each n corresponds to a critical pressure from which a shape of the buckled ring is obtained. These critical pressures are:

$$p_{cr,k} = (k^2 - 1)\frac{EI}{R^3} \qquad k = 2, 3, 4, \ldots \qquad (4.12)$$

Brush and Almroth (1975) obtained the same result using energy considerations. They also discussed the case of a pressure directed toward the center of the ring and not necessarily normal to the surface of the ring. In this case, the critical pressures found are:

$$p'_{cr,k} = \frac{(k^2 - 1)^2}{k^2 - 2}\frac{EI}{R^3} \qquad k = 2, 3, 4, \ldots \qquad (4.13)$$

These two equations constitute a range for critical pressures determination, given a certain mode number k. We note that the electromagnetic loading used in the present work generates a loading that is always directed normal to the deformed ring and therefore Eq. (4.12) is the appropriate critical pressure.

4.1-2 Dynamic Plastic Buckling

This section follows the work of Jones (1989) and Lindberg and Florence (1987). The material is now considered to be elastic-plastic and the buckling behavior of the ring is determined. Also, the load is taken to be dynamic, meaning that it changes rapidly with time. This means that the acceleration of the ring must be considered in the equations of motion. In order to simplify the problem, the stress-strain curve is taken to be bilinear: the elastic region has a modulus of E and the plastic region has a strain-hardening modulus of E_h. The total radial displacement $w^*(\theta, t)$ is composed of an initial imperfection $w^i(\theta)$ which depends only on θ

and of a radial displacement depending on time and measured positive toward the center of the ring: $w(\theta, t)$. Then:

$$w^*(\theta, t) = w(\theta, t) + w^i(\theta) \tag{4.14}$$

Considering Figure 4.3a, we obtain the following equilibrium equations corresponding respectively to the motion in the radial and tangential directions, and to the equilibrium of moment (ignoring rotary inertia):

$$\frac{dQ}{d\theta} + N + N\frac{d^2(w + w^i)}{Rd\theta^2} + \frac{dN}{d\theta}\frac{d(w + w^i)}{Rd\theta} - \mu R\frac{d^2w}{dt^2} = 0 \tag{4.15a}$$

$$\frac{dN}{d\theta} - Q - N\frac{d(w + w^i)}{Rd\theta} = 0 \tag{4.15b}$$

$$\frac{dM}{Rd\theta} - Q = 0 \tag{4.15c}$$

where μ is the mass per unit circumferential length of the ring. After some algebraic manipulations, this gives rise to the following governing equation:

$$\frac{d^2M}{d\theta^2} + NR + N\frac{d^2(w + w^i)}{d\theta^2} - \mu R^2\frac{d^2w}{dt^2} = 0 \tag{4.16}$$

To solve this equation, M and N can be determined knowing that, when the entire cross-section of the ring is fully plastic, we have:

$$M = E_h I\kappa \quad \text{and} \quad N = a\left(\pm\sigma_y + E_h\varepsilon\right) \tag{4.17}$$

where a is the radial thickness of the ring and σ_y is the uniaxial yield stress. From Figure 4.3b we have:

$$\kappa = -\frac{1}{R}\frac{d^2w}{d\theta^2} \quad and \quad \varepsilon = \frac{dS - dS_0}{dS_0} = -\frac{w}{R} + \frac{1}{2}\left(\frac{1}{R}\frac{dw}{d\theta}\right)^2 + \left(\frac{1}{R}\frac{dw}{d\theta}\right)\left(\frac{1}{R}\frac{dw^i}{d\theta}\right) \quad (4.18)$$

The final equation of motion is determined by replacing (4.18) in (4.17) and then (4.17) in (4.16). Moreover, it is assumed that the deformation of the ring from the initial imperfection consists of two parts: a dominant axisymmetric motion denoted $\overline{w}(t)$ and a perturbed non-axisymmetric displacement denoted $w'(\theta, t)$. After replacing all these expressions in (4.16) and separating low order to high order terms in the resulting equation, we end up with the following two differential equations, representing respectively the dominant motion and the perturbed behavior:

$$\frac{d^2\overline{w}}{dt^2} + \frac{E_h a}{\mu R^2}\overline{w} = -\frac{a\sigma_y}{\mu R} \quad (4.19)$$

$$\frac{d^4w'}{d\theta^4} + \frac{R^2 a}{I}\left(\frac{\sigma_y}{E_h} + \frac{\overline{w}}{R}\right)\frac{d^2w'}{d\theta^2} + \frac{\mu R^4}{E_h I}\frac{d^2w'}{dt^2} = -\frac{R^2 a}{I}w' - \frac{R^2 a}{I}\left(\frac{\sigma_y}{E_h} + \frac{\overline{w}}{R}\right)\frac{d^2w^i}{d\theta^2} \quad (4.20)$$

Eq. (4.19) gives rise to the following solution for the dominant axisymmetric behavior:

$$\overline{w} = C_1 \cos\left(\sqrt{\frac{E_h a}{\mu R^2}}t\right) + C_2 \sin\left(\sqrt{\frac{E_h a}{\mu R^2}}t\right) - \frac{\sigma_y R}{E_h} \quad (4.21)$$

Eq. (4.20) is more important in studying the buckled shape of the ring. In the general case, w' and w^i can be represented in the form of trigonometric series:

$$w' = \sum_{n=2}^{\infty} W_n'(t)\sin(n\theta) \qquad and \qquad w^i = \sum_{n=2}^{\infty} W_n^i \sin(n\theta) \quad (4.22)$$

As has been shown earlier, the case $n = 1$ corresponds to rigid body translation and is disregarded. Substituting (4.22) into (4.20), W_n' has to satisfy this final equation:

$$\frac{d^2W_n'}{dt^2} - R_n^2 W_n' = S_n W_n^i \qquad n = 2, 3, 4 \ldots \tag{4.23}$$

where R_n and S_n are given by:

$$R_n = -\frac{E_h I}{\mu R^4}\left\{-\frac{\left(\sigma_y a + E_h a\frac{\overline{w_f}}{R}\right)R^2}{E_h I}n^2 + n^4 + \frac{R^2 a}{I}\right\} \tag{4.24a}$$

$$S_n = \frac{\sigma_y a + E_h a\frac{\overline{w_f}}{R}}{\mu R^2}n^2 \tag{4.24b}$$

with $\overline{w_f} = \frac{\sigma_y R}{E_h}\left(\sqrt{1 + \frac{\mu V_0^2 E_h}{\sigma_y^2 a}} - 1\right)$. The case $R_n^2 < 0$ leads to an oscillatory solution for W_n' and is therefore not examined, whereas dynamic plastic buckling will manifest in the case $R_n^2 > 0$, for which we obtain:

$$W_n' = A_n \cosh(R_n t) + B_n \sinh(R_n t) - \frac{S_n W_n^i}{R_n^2} \tag{4.24}$$

Setting initial imperfections in velocity V_n^i such as: $\frac{dw(0)}{dt} = V_0 + \sum_{n=2}^{\infty} V_n^i \sin(n\theta)$, we can write the initial conditions: $W_n'(0) = 0$ and $\frac{dW_n'}{dt}(0) = V_n^i$. Finally, we obtain an expression for W_n':

$$W_n' = W_n^i E_n(t) + V_n^i F_n(t) \tag{4.25}$$

where $E_n(t) = \frac{S_n(\cosh(R_n t) - 1)}{R_n^2}$ and $F_n(t) = \frac{\sinh(R_n t)}{R_n}$ are respectively called the displacement and velocity amplification functions. Jones (1989) has shown that, even though the dimensionless ratio of displacement and velocity amplification functions decreases as the initial velocity increases, it is a relatively high number. In the experiment presented in this thesis, R is on the order of 15 mm and a is about 0.5 mm, so that $\frac{R}{a} \approx 30$. For this ratio radius to thickness, Jones

obtained $\frac{RE_n}{V_0F_n} \approx 80$, leading to the conclusion that dynamic plastic buckling is more sensitive to initial imperfections in shape than to imperfections in initial velocity, which therefore can be neglected. Finally, plotting E_n and F_n as functions of n shows that a maximum is reached for a certain value n_c, which is that same for both E_n and F_n. n_c is called the critical mode number and assuming $I = \frac{a^3}{12}$, it can be approximately computed with:

$$n_c = \frac{R}{a}\sqrt{\frac{6\bar{\sigma}}{E_h}} \qquad with \qquad \bar{\sigma} = \frac{\sigma_y}{2}\left(1 + \sqrt{1 + \frac{\mu V_0^2 E_h}{\sigma_y^2 a}}\right) \qquad (4.26)$$

Figure 4.4 shows a plot of the critical mode n_c as a function of the velocity V_0. This concept of critical mode is of primary importance. The main result above indicates that for any given velocity on the ring, a particular mode is selected. Considering stochastically distributed initial imperfections in the shape of the ring, this critical mode number will be the most probable we can observe on the deformed ring. In order to compare this critical value to the mode numbers actually measured in the experiments, calculations of n_c were made for the different values of V_0 corresponding to the four charge levels. The following parameters were taken for the calculation of n_c:

- E_h was approximated from the constitutive law (2.21) as: E_h = 240 MPa
- μ was computed from the density ρ = 2700 kg.m^{-3} for Al 6061-O: μ = 1.35 kg.m^{-2}
- V_0 was taken to be the velocities measured at the onset of buckling during the experiments: from –40 m.s^{-1} for the 2 kV charge to –200 m.s^{-1} for the 5 kV charge.

Table 6 gives a summary of the results found for the critical mode number n_c as well as a comparison with the minimum and maximum mode numbers found in the experiments for the corresponding charge levels. While the maximum modes found in the experiments are lower than

the calculated $n_c(V_0)$, a wide range of modes are activated in the experiments. In order to obtain a better estimate of the observed response, it is then important to track not only the fastest growing perturbation, but all perturbations in a statistical sense. This is considered next through direct numerical simulations of the experiments.

4.2 Finite Element Model

Dynamic plastic buckling calculations for the Al 6061-O rings were also performed using the finite element code ABAQUS.

4.2-1 Templates of the ring and material

The ring was modeled using 2-D plane-strain, explicit and quadratic elements. A three-dimensional analysis would have been better, but time constraints dictated this first choice. To use the structured meshing technique, the ring had to be divided into two half-rings. The dimensions of the ring that was drawn on ABAQUS followed the exact geometry of the rings used in the experiments: an external diameter of 15.75 mm, thickness of 0.5 mm and an internal diameter of 15.25 mm. The entire ring was meshed in the simulations, without imposing any symmetry. A total number of 19,480 elements were used to mesh the entire ring, with 10 elements used along the radial direction and 1948 elements along the circumference. The material used had the same properties as described in Chapter 2: elastic behavior with a modulus of 70 MPa and plastic response was modeled with a J_2 incremental theory of plasticity, following the power law described in Eq. (2.21). Moreover, for the computations of the inertia terms, the density of Al 6061-O was taken to be $\rho = 2700$ kg.m^{-3}.

The pressure history was applied normally to the outer radius of the ring. Three simulations were performed in ABAQUS, with three different pressures corresponding to the 3 kV, 4 kV and 5 kV charge levels. The pressures used in these simulations are shown in Figure 4.5. They are the exact forms of the pressures encountered by the specimen in the actual experiments from 0 to 60 μs. From 60 μs to 100 μs, the pressures used in ABAQUS were zeroed in order to allow the solution to converge while applying the buckling imperfections as described later. Indeed, the deformations are too large to be reliable for too long after that time, and the rings finally collapse entirely. As already described, the pressures are constituted of a first positive peak, followed by a negative wave and finally a positive peak whose amplitude is lower than the first peak.

4.2-2 Buckling Analysis

Before running these analyses, imperfections in the shape of the ring are included in order to reproduce the buckling effects in these numerical simulations. To do so, an eigenvalue analysis was performed prior to running the considered simulation on ABAQUS. A total number of 80 modes were computed and their shapes were added to the different simulations with certain amplitudes, in order to introduce specific buckling imperfections in the shape of the ring according to Eq. $(4.22-2)$. These initial imperfections will give rise to a natural selection of preferred buckling modes as the ring deforms. This way, the actual imperfections in the rings are simulated to furnish a good model of the experiments.

Figure 4.6 show examples of the buckling shapes for two modes computed by the ABAQUS eigenvalue analysis: $n = 6$ and $n = 30$. Referring to Eq. $(4.22-2)$, the equations for

these buckled shapes are $w^i = W_6^i \sin(6\,\theta)$ and $w^i = W_{30}^i \sin(30\,\theta)$ respectively. ABAQUS computes automatically the amplitudes W_6^i and W_{30}^i to produce the shapes shown in Figure 4.6.

4.2-3 3 kV charge simulation

This simulation was performed to compare with the 3 kV charge level experiments. Mode numbers between 15 and 30 were selected from the buckling analysis. This corresponds to the extent of modes we expect to observe for this charge level, according to both theory and experiments. From Eq. $(4.22-2)$, this introduces the following imperfections in the shape of the initial ring: $w^i = \sum_{n=15}^{30} W_n^i \sin(n\theta)$. The amplitudes set were: $W_n^i = 10^{-6}$ m for $n = 15$ to $n = 30$. An overlay of several images of the deformed shape of the ring at different steps during the simulation is shown in Figure 4.7. These images were taken between 0 and 72 µs at times comparable to those from the experiments – see Figure 3.16. We can note that the ring behaves globally as expected from the experimental results:

- First, the ring deforms uniformly in an axisymmetric fashion, as its radius decreases.
- Secondly, the compression of the ring slows down as it starts to buckle. This speed reduction coincides also with a decrease in the loading (reverse loading).
- Once it has buckled, the radius of the ring continues decreasing, but with a lower speed than in the first part and buckling waves grow in amplitude.

A plot of the decrease of the ring radius with time is shown in Figure 4.8. On this graph, six curves are drawn. Three of them are in different shades of orange. They correspond to the three points selected at different locations on the shape of the ring, as shown in Figure 4.7. Point 1 is in a region where no buckling waves appeared and hence can be considered as a "mean" radius for the entire ring. Point 2 corresponds to the uppermost point on a buckling wave, and hence is

moving slower than other parts of the ring. Point 3 corresponds to the lowest point on the same buckling wave. We can notice that these three curves coincide until buckling occurs. The time at the onset of buckling can be approximated from the percentage deviation computed between the radii at the two extreme points on the wave (points 2 and 3) and the mean radius at point 1. A graph of the percentage deviation is shown in Figure 4.9. Using the criterion that buckling appears when the deviation is of 0.5%, the onset of buckling can be approximated around 28 μs. The radial velocity during buckling is measured around –90 m/s. Both values are in the range found for the experiments with a 3 kV charge level. As the buckling wave grows in amplitude, the curves of the radii at the three locations 1, 2 and 3 dissociate from one another. Three other curves are drawn in different shades of blue on the same graph, Figure 4.8. They correspond to the three experiments performed with the 3 kV charge voltage. It appears that their shapes coincide well with the simulation curves if we shift them by a certain amount of time; this is possibly due to error in time resolution in the experiments and has not been resolved.

Finally, we observe that several modes appear simultaneously at different places in the ring. Higher modes (ranging from 15 to 30, selected as shape imperfections) are preferred and exhibit larger amplitudes than others. In other regions, no buckling waves appear.

4.2-4 4 kV charge simulation

This simulation was performed to compare with the 4 kV charge level experiments. Mode numbers between 20 and 30 were selected from the buckling analysis. This corresponds to the extent of modes we expect to observe (from the experiments) for this charge level. From Eq. $(4.22-2)$, this introduces the following imperfections in the shape of the initial ring: $w^i = \sum_{n=20}^{30} W_n^i \sin(n\theta)$. The amplitudes were set as: $W_n^i = 10^{-6}$ m for $n = 20$ to $n = 30$. An

overlay of several images at different steps during the simulation is shown in Figure 4.10. These images were taken between 0 and 60 μs at times comparable to those from the experiments – see Figure 3.23. The ring behaves globally as expected from the experimental results and as described for the previous simulation:

- First, a uniformly axisymmetric deformation of the ring.
- Second, the compression of the ring slows down as it starts to buckle. This speed reduction also coincides with a decrease in the loading (reverse loading).
- Finally, once it has buckled, the radius of the ring continues decreasing, but with a lower speed than in the first part, and buckling waves grow in amplitude.

A plot of the decrease of the ring radius with time is shown in Figure 4.11. On this graph, six curves are drawn. Three of them are in different shades of orange. They correspond to the three points selected on the shape of the ring as described earlier: point 1 is in a region where no buckling waves appeared, point 2 is at the uppermost point on a buckling wave and point 3 corresponds to the lowest point on the same buckling wave. The localizations of these points are shown in Figure 4.10. These three curves coincide until buckling occurs. The time at the onset of buckling can be approximated with the percentage deviation method, computed between the radii at the two extreme points on the wave (points 2 and 3) and the mean radius at point 1. Using the same criterion that buckling appears when the deviation is of 0.5%, the onset of buckling can be approximated around 24 μs. The radial velocity during buckling is measured around –160 m/s. Both values are in the range found for the experiments with a 4 kV charge level. As the buckling wave gains in amplitude, the curves of the radii at the three locations dissociate from one another. Three other curves are drawn in different shades of blue on the same graph, Figure 4.11. They correspond to the three experiments performed with the 4 kV charge voltage. This time, the three

of these curves have been shifted by $\Delta t = 7$ μs. This amount corresponds roughly to the time elapsed between two frames taken by the camera (at a speed of 150,000 frames per second, the camera takes a picture about every 6.7 μs). It appears that they all coincide reasonably well.

Finally, we observe that several modes appear simultaneously at different places in the ring. Higher modes (ranging from 20 to 30, as selected by shape imperfections) are preferred and exhibit larger amplitudes than others. In other regions, no buckling waves appear.

4.2-5 5 kV charge simulation

This simulation was performed to compare with the 5 kV charge level experiments. Mode numbers between 22 and 40 were selected from the buckling analysis. This corresponds to the extent of modes we expect to observe (from the experiments) for this charge level. From Eq. $(4.22-2)$, this introduces the following imperfections in the shape of the initial ring: $w^i = \sum_{n=22}^{40} W_n^i \sin(n\theta)$. The amplitudes were set as: $W_n^i = 10^{-6}$ m for $n = 22$ to $n = 40$. An overlay of several images at different steps during the simulation is shown in Figure 4.12. These images were taken between 0 and 35 μs at times comparable to those from the experiments – see Figure 3.30. The ring behaves globally as expected from the experimental results and as described for the previous simulation:

- First, a uniformly axisymmetric deformation of the ring.
- Second, the compression of the ring slows down as it starts to buckle. This speed reduction coincides also with a decrease in the loading (reverse loading).
- Finally, once it has buckled, the radius of the ring continues decreasing, but with a lower speed than in the first part, and buckling waves grow in amplitude.

A plot of the decrease of the ring radius with time is shown in Figure 4.13. On this graph, six curves are drawn. The plots in different shades of orange correspond to the three points selected on the shape of the ring as described earlier: point 1 is in a region where no buckling waves appeared, point 2 is at the uppermost point on a buckling wave and point 3 corresponds to the lowest point on the same buckling wave. The localizations of these points are shown in Figure 4.12. These three curves coincide until buckling occurs. The time at the onset of buckling can be approximated with the same percentage deviation method as previously used. Using the criterion that buckling appears when the deviation is of 0.5%, the onset of buckling can be approximated around 20 μs. The radial velocity during buckling is measured around –250 m/s. Both values are in the range found for the experiments with a 5 kV charge level. As the buckling wave gains in amplitude, the curves of the radii at the three locations dissociate from one another. Three other curves are drawn in different shades of blue on the same graph (Figure 4.13), corresponding to the three experiments performed with the 5 kV charge voltage. This time, only the first experimental curve was shifted by $\Delta t = 7$ μs, the others are from the crude data. They all coincide very well. At some point after buckling has occurred, the experimental and the simulation curves deviate from one another, possibly because of different buckling effects occurring in the specimens compared to the model implemented in the simulation. This may be due to the presence of initial imperfections which were not modeled.

Finally, we observe that several modes appear simultaneously at different places in the ring. Higher modes (ranging from 22 to 40 as selected by shape imperfections) are preferred and exhibit larger amplitudes than others. In other regions, no buckling waves appear.

CHAPTER 5: CONCLUSIONS AND RECOMMENDATIONS

The aim of this study was to investigate the buckling response of thin Al 6061-O rings subjected to uniform radial pressure. Twelve experiments were performed with different pressure levels. As described in Chapter 2, the pressure was created via electromagnetic induction. A rapid discharge of a capacitor through a specially-built solenoid created a magnetic field that interacted with the conducting specimen to generate an induced current. The interaction between the repulsive currents in both the solenoid and the ring produces a compressive pressure on the specimens. Three experiments were performed for each of the following four discharge levels: 2 kV, 3 kV, 4 kV and 5 kV. These discharges produced maximum pressure levels between 7 MPa and 38 MPa. The deformation of the specimens was monitored using a high-speed camera, which was set to take pictures at rates between 150,000 and 230,000 frames per second in the experiments performed. Analyses of these pictures are conducted in detail in Chapter 3. This section gives a summary of the conclusions of this study.

First of all, the following general observations were made about the deformation of the rings with respect to time:

- The movement of the ring is constrained until the pressure reaches a critical value, which ranges between 3 MPa for the 2 kV charge level and 28 MPa for the 5 kV discharge.
- Subsequently the average radius begins to decrease with a constant speed. This speed is around 40 m/s for the 2 kV discharge, 80 m/s for 3 kV, 140 m/s for 4 kV and 200 m/s for 5 kV. During this step of the deformation, the ring compresses in a uniform and axisymmetric fashion and no buckling waves appear.

- After it has reached a certain hoop strain, the ring begins to buckle, selecting certain mode shapes. The measured hoop strains at the visible onset of buckling were between –3.7 % for the 2 kV experiments and –8.8 % for the 5 kV discharges. It corresponds to impulses encountered by the specimens between around 100 Pa.s and 460 Pa.s for the respective charge levels.
- Once the ring buckles, its radial speed decreases as its kinetic energy transforms into strain energy.
- Finally, the specimen continues to buckle and collapses entirely.

Note that the different times measured are precise only within the time elapsed between two frames taken by the camera, which is about 6.7 μs for a camera speed of 150,000 frames per second. Consequently, the measures of the strain, the impulses and velocities at the onset of buckling are known only within a certain approximation, everything being based on the framing times. The higher the speed of the camera, the sharper these measures become; that is why it may be interesting, in future tests, to increase the speed of the camera which can spin to take up to 400,000 frames per second. This global motion of the specimen has been reasonably well reproduced and confirmed by the numerical simulations performed with ABAQUS.

Secondly, measurements of several buckling waves for each of the experiments were performed and the following conclusions can be drawn:

- At the onset of buckling, different buckling wave lengths appear *simultaneously*. Many different wave lengths of buckles, corresponding to different apparent mode numbers are selected appear simultaneously.

- The corresponding mode numbers range between 3 and 25 for the 2 kV discharge, 13 and 34 for 3 kV, 20 and 31 for 4 kV and finally between 20 and 44 for the 5 kV discharge. The mode numbers appearing in the shape of the rings increase as the pressure (and the rate of loading) on it increases.
- Comparison with the theory developed by Jones (1989) shows that the highest modes found for each voltage (25 for 2 kV, 34 for 3 kV, 31 for 4 kV and 44 for 5 kV) match well with the theoretical critical modes (26, 33, 39 and 47 respectively); in addition, lower modes are developed as well.
- A number of the buckling waves were studied at different times during the event. Interestingly, measurements show that once a certain mode is selected, the buckle maintains it all over the deformation of the ring until collapse.
- The comparison between this result and the finite element simulations shows that the selection of the mode by the ring is dictated by imperfections in its shape. In practice, these imperfections are distributed stochastically in the specimen, resulting in the appearance of selected modes at random places in the ring.

Note that not all the buckling waves were studied because of the difficulty to identify them clearly in many cases. To improve the consistency of the measurements of the wave lengths, more experiments should be performed. Nevertheless, the present study extended the observations that had been made by Al-Hassani (1974). The main new observation was that several buckling modes appeared after the onset of buckling. The combination of experiments and analysis performed here provided a broader understanding of the buckling response of metallic rings under dynamic loading. This work was conducted with thin Al 6061-O rings. Based on other works (Florence, 1968, Jones 1976), the response may differ from metal to metal.

Appendix

The following code was written with MATLAB in order to compute the best-fit circles for each picture of the ring specimens taken during their deformations. The least square method was used to determine the center $(x_C; y_C)$ and the radius R of this best fit circle. See Figure 3.6 for an example.

```
clear all; clf;clc;

[nom, repert] = uigetfile('*.bmp', 'Ouverture Matlab');
nomfich = ([repert,nom]);
M=importdata(nomfich);
disp('Fichier Ouvert')
image=imread(nomfich);
imagesc(image)

axis square
title ('Select Point','FontSize',14)
% Mouse : select with left button / end selection with right button
x = 0.;
y = 0.;
button = 1;


while button == 1            % while left button is pressed
[x,y,button] = ginput;       % read selected point
end

hold on


plot(x,y,'o')
   x=x(:); y=y(:);
   a=[x y ones(size(x))]\[-(x.^2+y.^2)];
   xc = -.5*a(1);            % x coordinate center best fit circle
   yc = -.5*a(2);            % y coordinate center best fit circle
   R  =  sqrt((a(1)^2+a(2)^2)/4-a(3));   % radius best fit circle


theta = linspace (0,2*pi,100);
xt = xc+R*cos(theta);
yt = yc+R*sin(theta);
```

```
hold on

plot (xt,yt,'r-','LineWidth',1)     % draw best fit circle
axis square

Matcircle=[R;xc;yc];                % data of the best fit circle

dr=R-sqrt((x-xc).^2+(y-yc).^2);     % distance between best fit circle
                                    and selected points

Mat=[x y dr];                       % matrix of the selected points
```

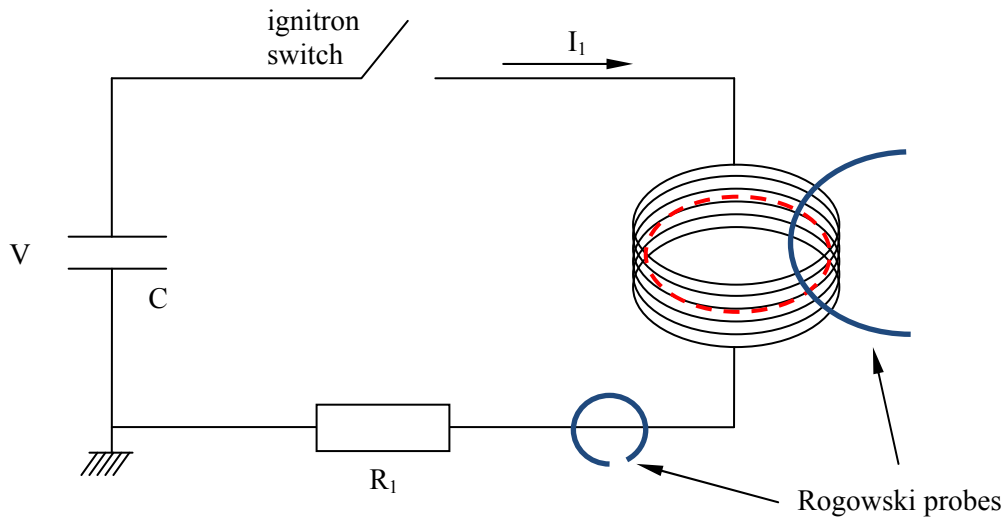

Figure 2.1a: Schematic of the coupled electromagnetic circuit. The ring specimen is shown in red inside the solenoid.

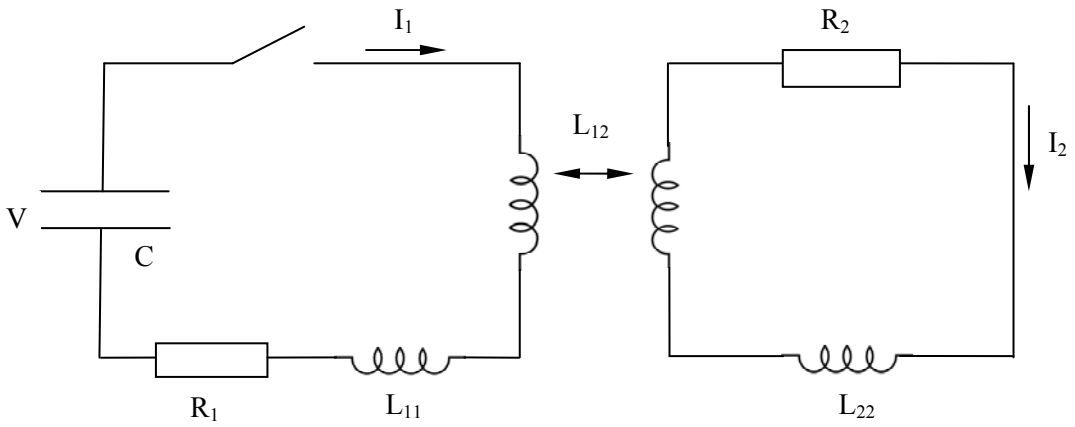

Figure 2.1b: Decoupled equivalent main (1) and secondary (2) circuits.

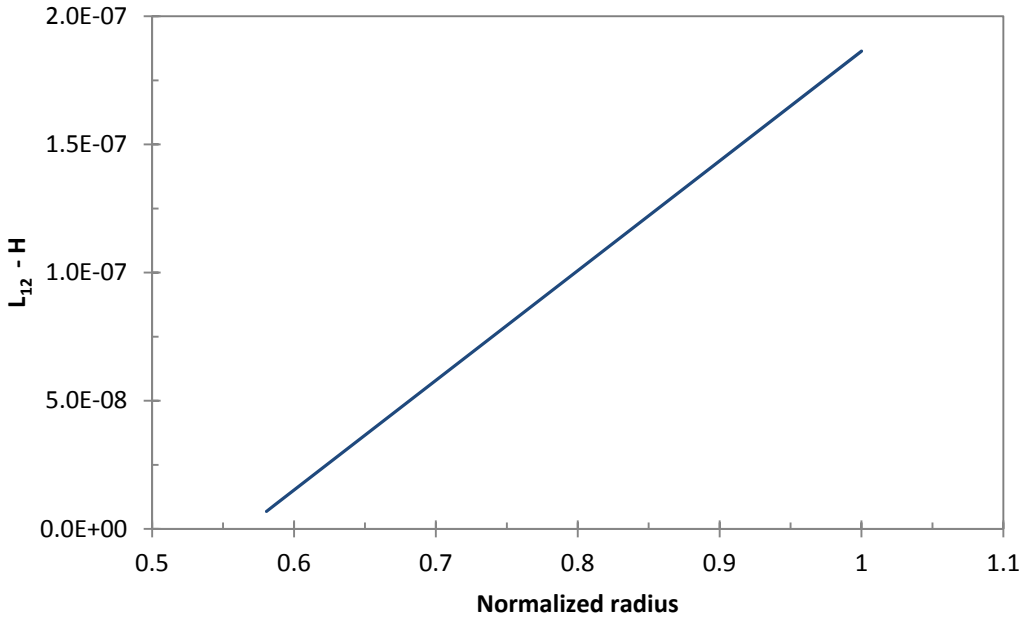

Figure 2.2: Graph of the mutual inductance L_{12} between the solenoid and the ring, as a function of the ring radius.

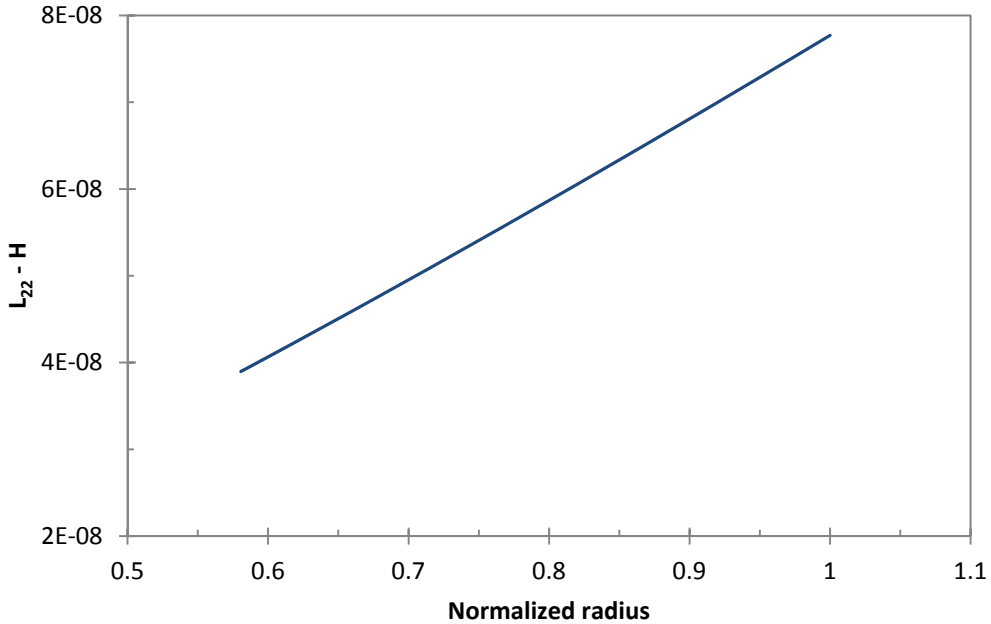

Figure 2.3: Graph of the self-inductance L_{22} as a function of the ring radius.

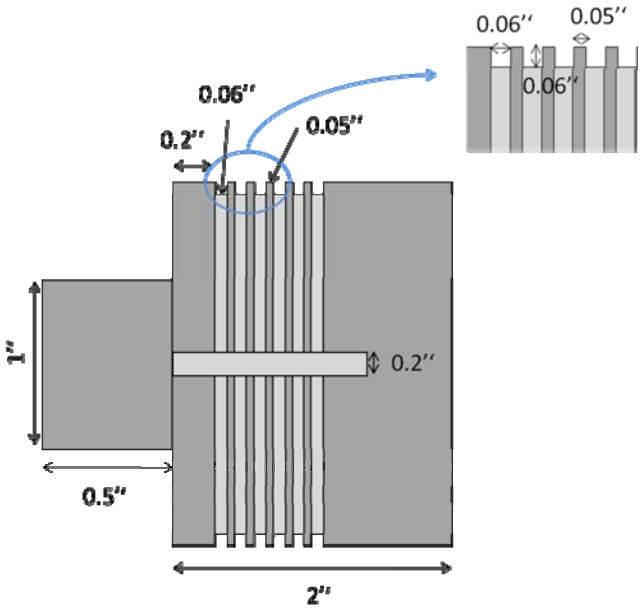

Side view

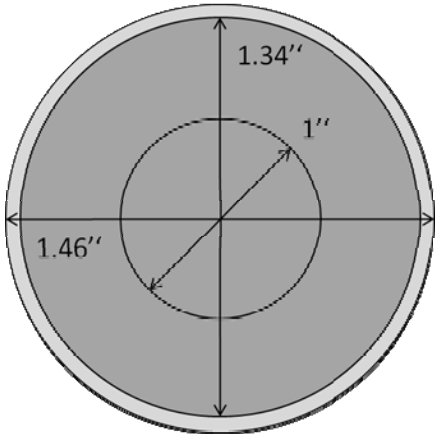

Top view

Figure 2.4a: Drawings of the first step in the manufacture of the solenoid: shaping of the cylinder and drilling of the grooves.

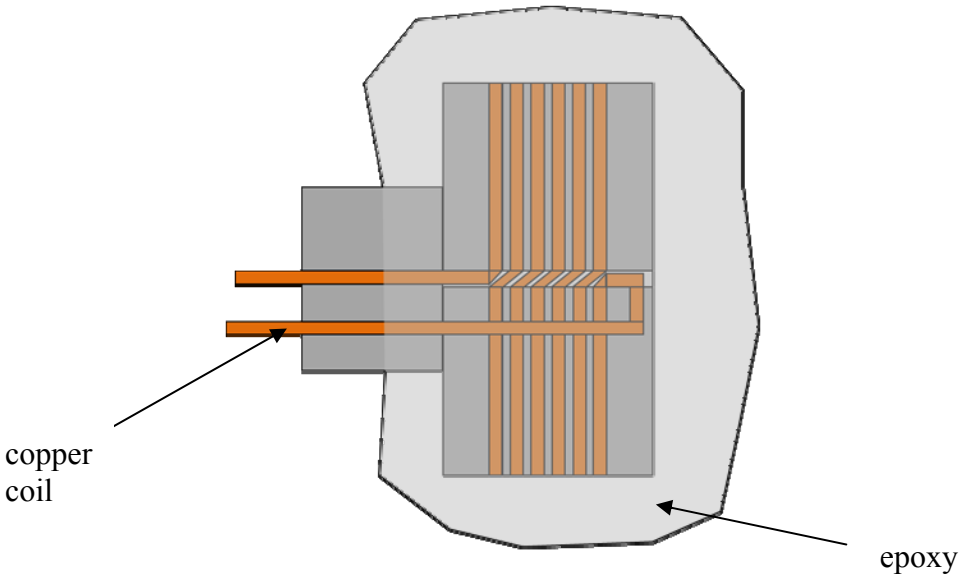

Side view

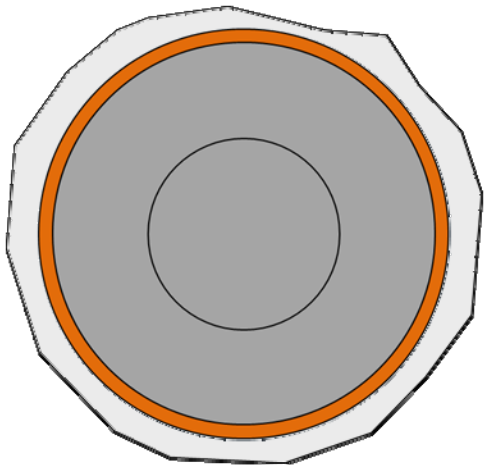

Top view

Figure 2.4b: Drawings of the second step in the manufacture of the solenoid: winding the copper coil and pouring and curing epoxy.

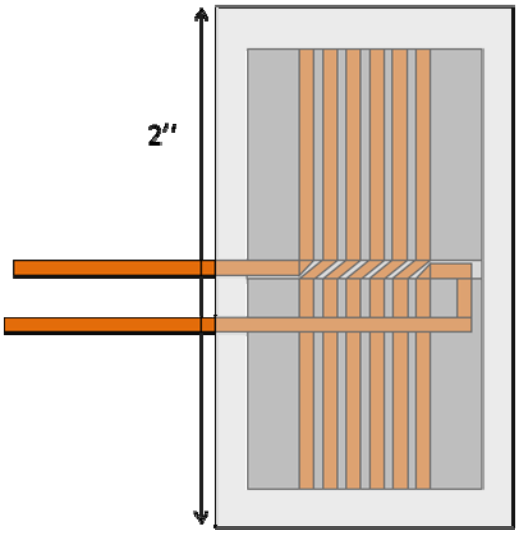

Side view

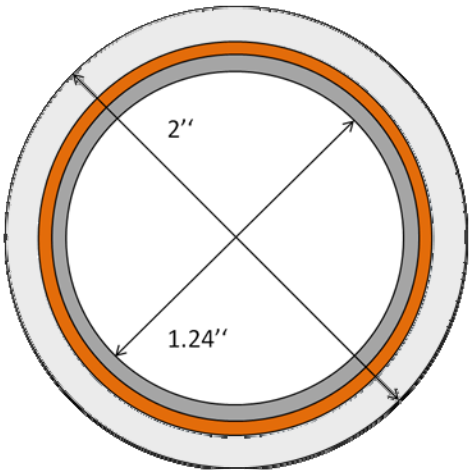

Top view

Figure 2.4c: Drawings of the third step in the manufacture of the solenoid: shaping the epoxy and drilling the central hole in the polycarbonate.

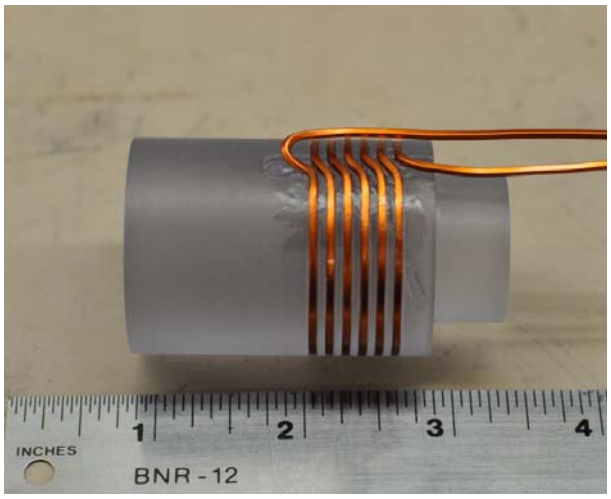

Figure 2.5: Picture of the copper coil wound around a polycarbonate cylinder during the process of the manufacture of the solenoid.

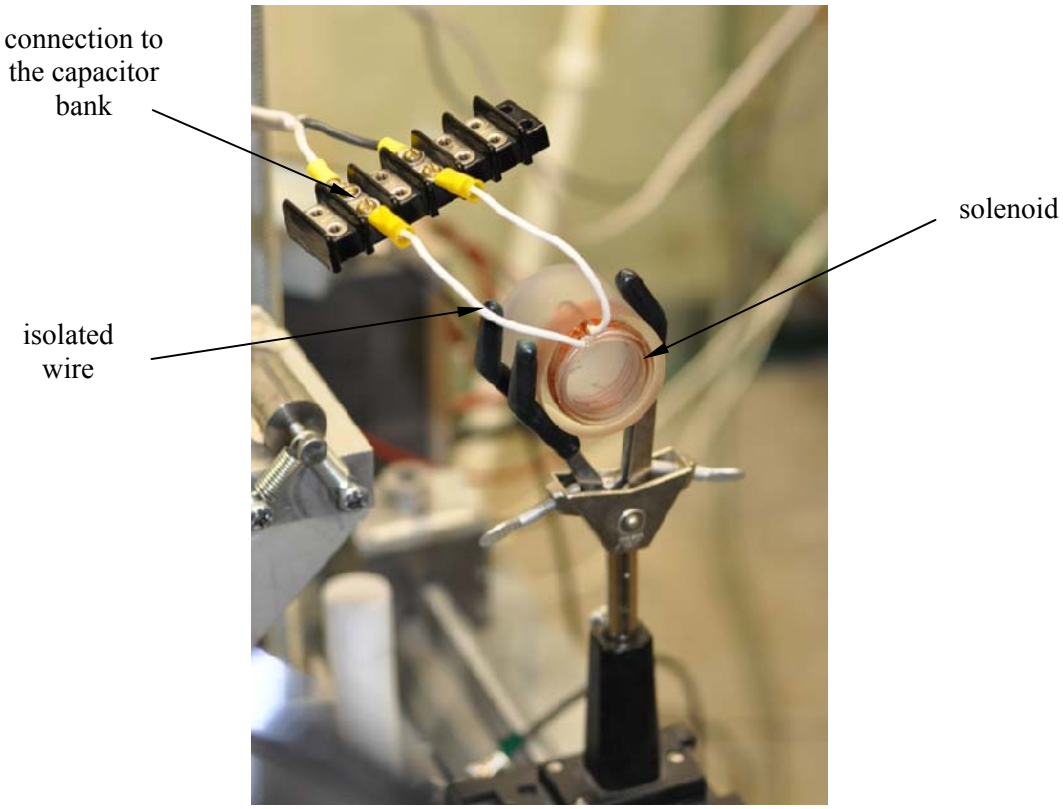

Figure 2.6: Picture of the finished solenoid in place on the support and connected to the capacitor bank.

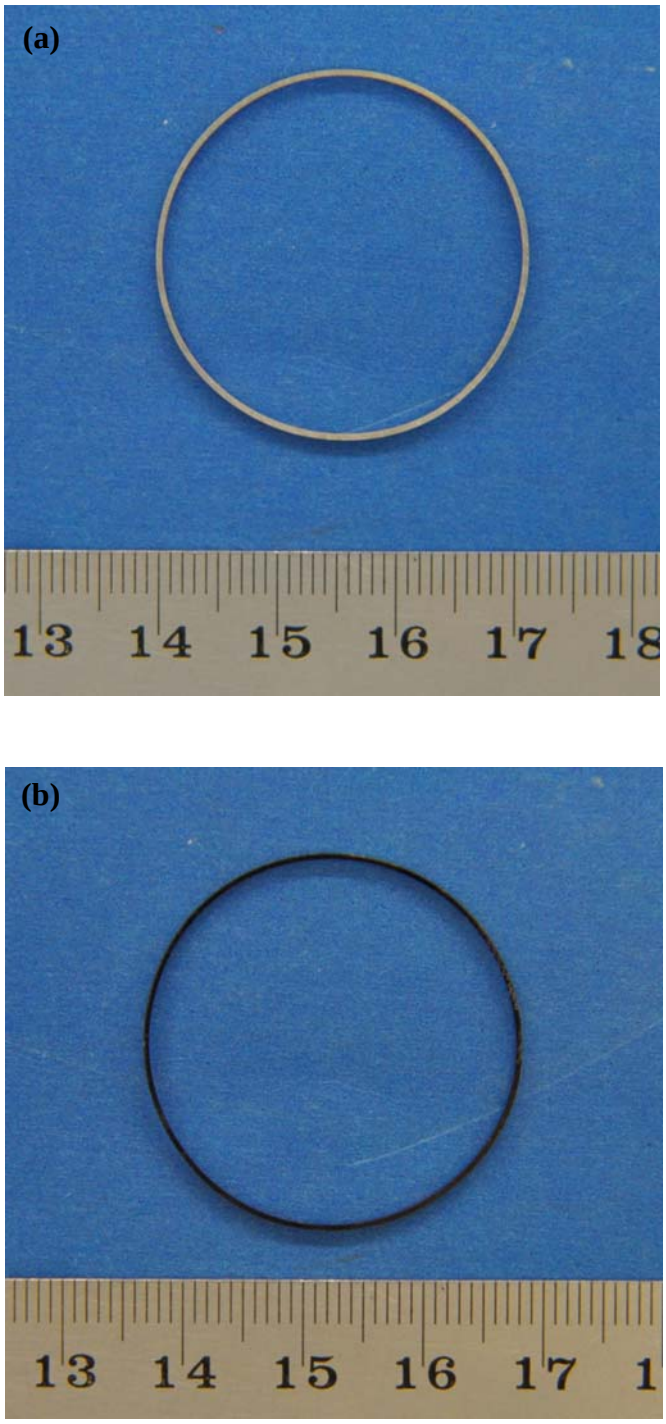

Figure 2.7: Picture of a ring specimen: before (a) and after (b) being painted in black.

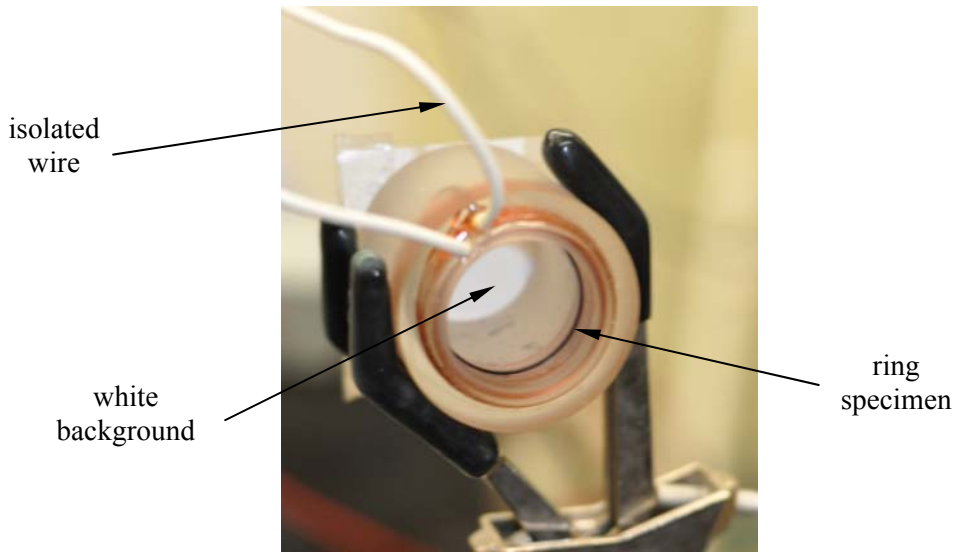

Figure 2.8: *Picture of a ring specimen in place inside the solenoid. The white background provides good reflection of the light coming from the flash lamps and hence better contrasted pictures.*

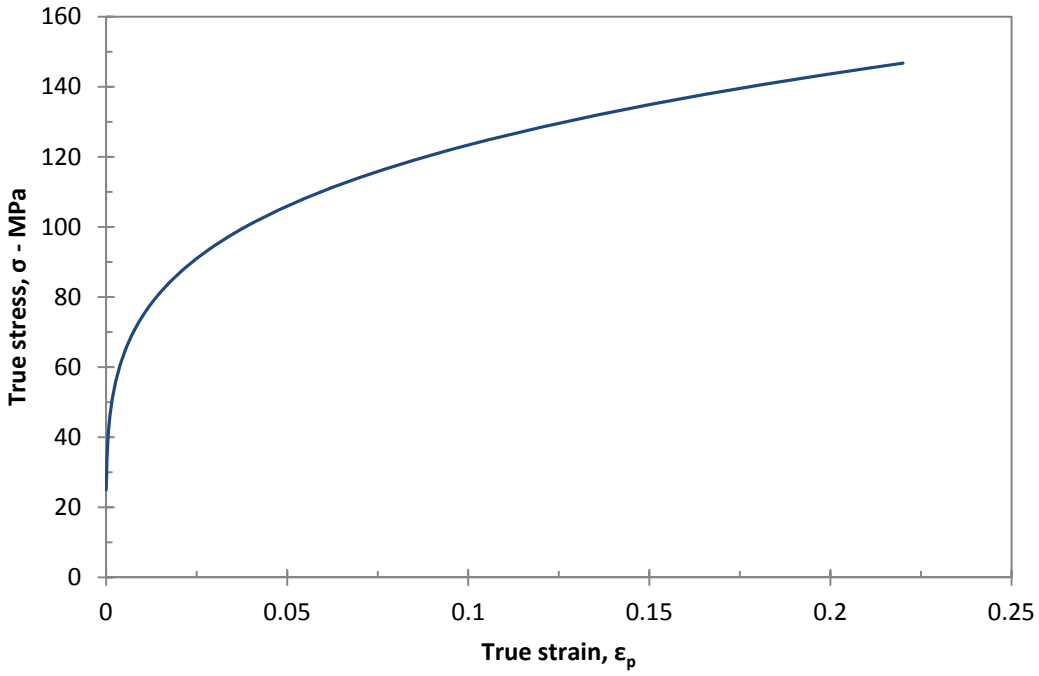

Figure 2.9: *True stress vs. true (logarithmic) strain curve representing the constitutive law for Al 6061-O.*

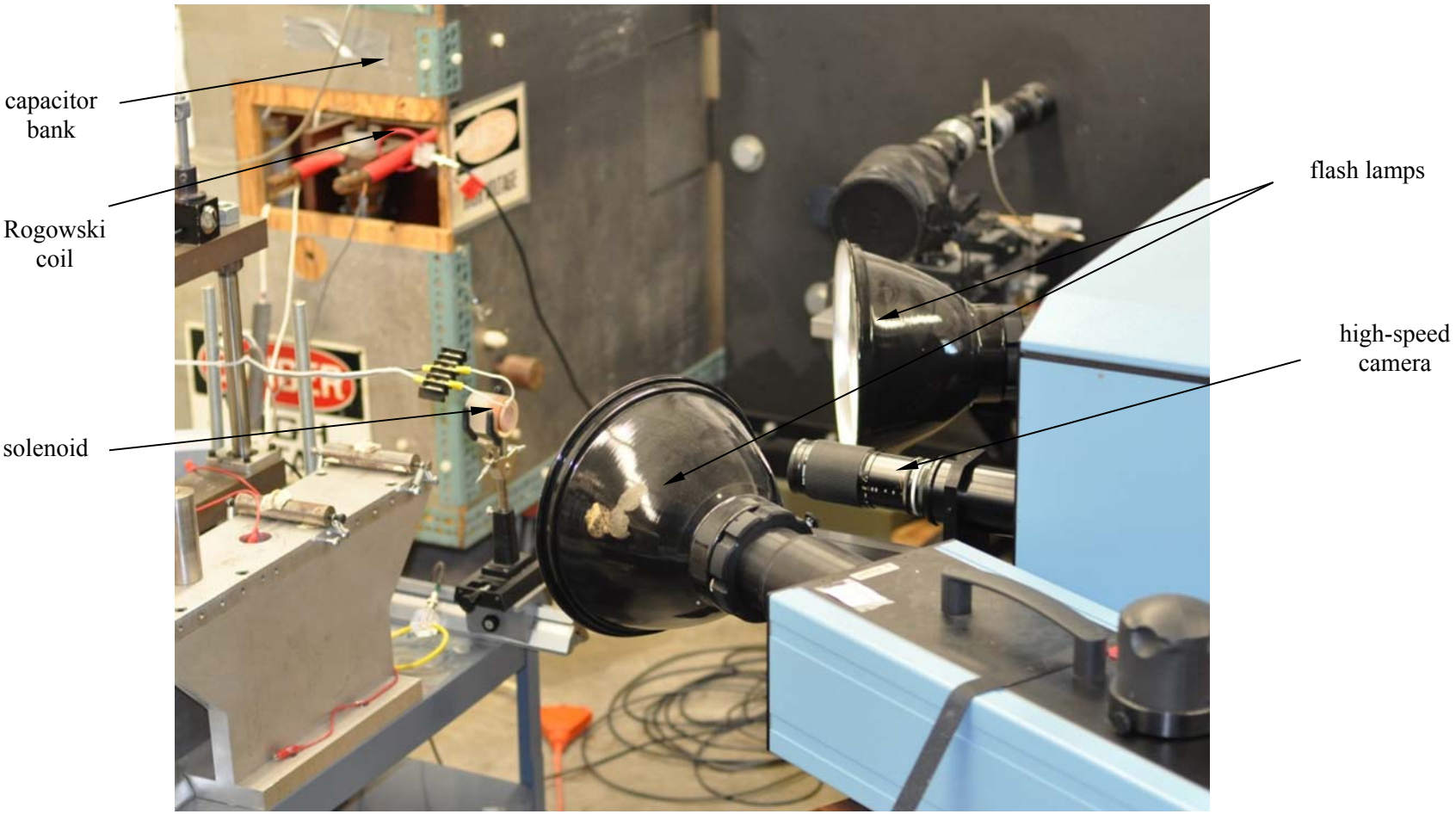

Figure 2.10: Photograph of the general experimental arrangement.

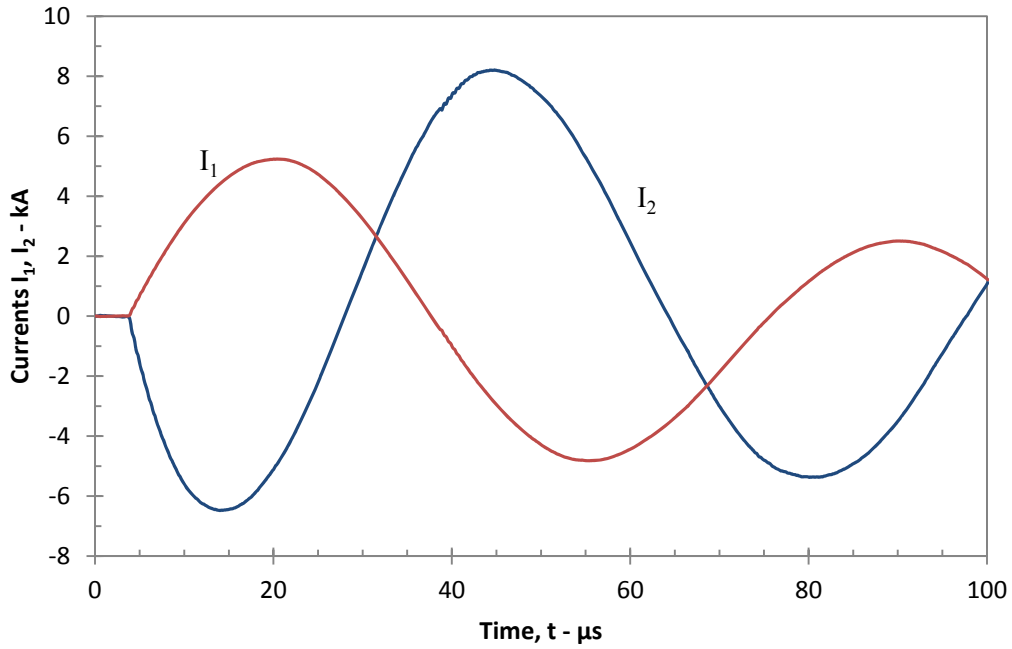

Figure 3.1: Currents I_1 and I_2 as functions of time, for a 2 kV charge voltage.

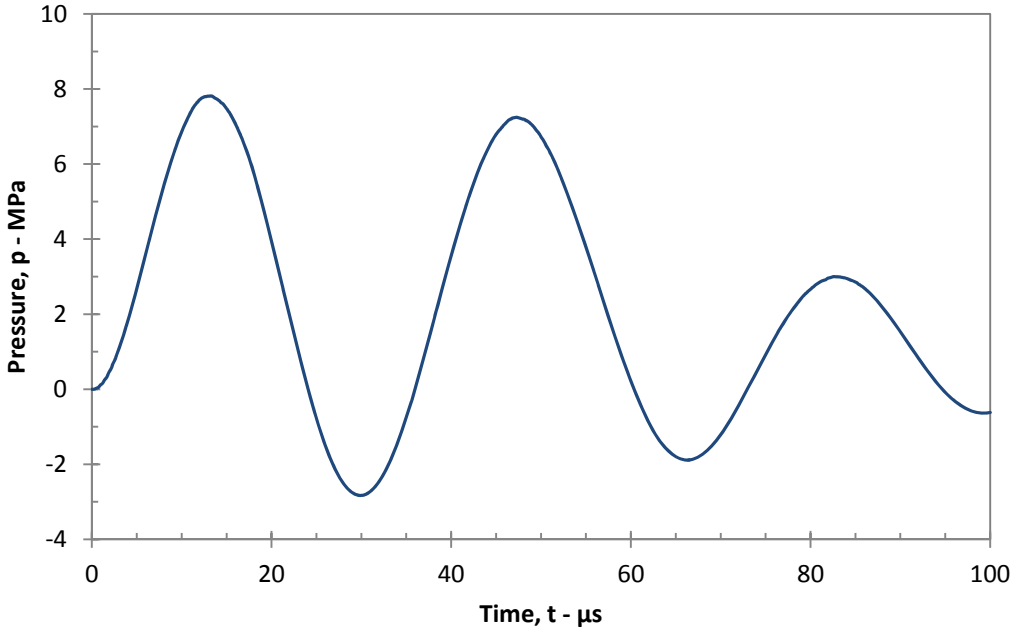

Figure 3.2: Pressure p acting on the ring as a function of time for a 2 kV charge voltage.

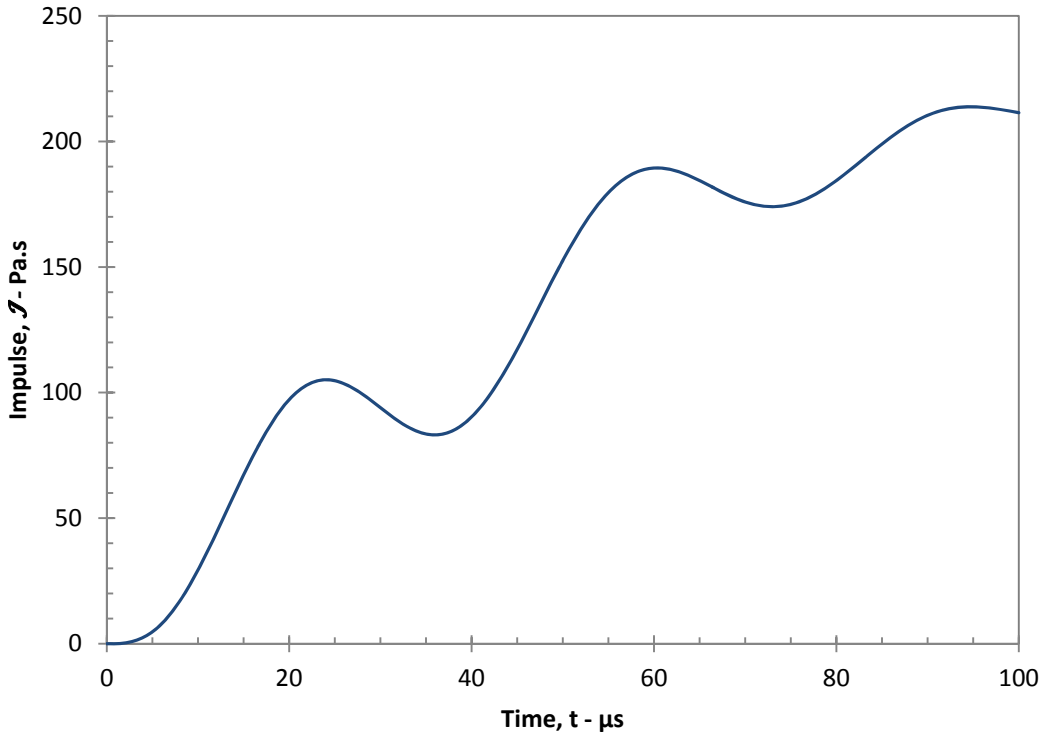

Figure 3.3: Impulse $\mathcal{I}$ in Pa.sec, corresponding to the previous pressure, for a 2 kV charge level.

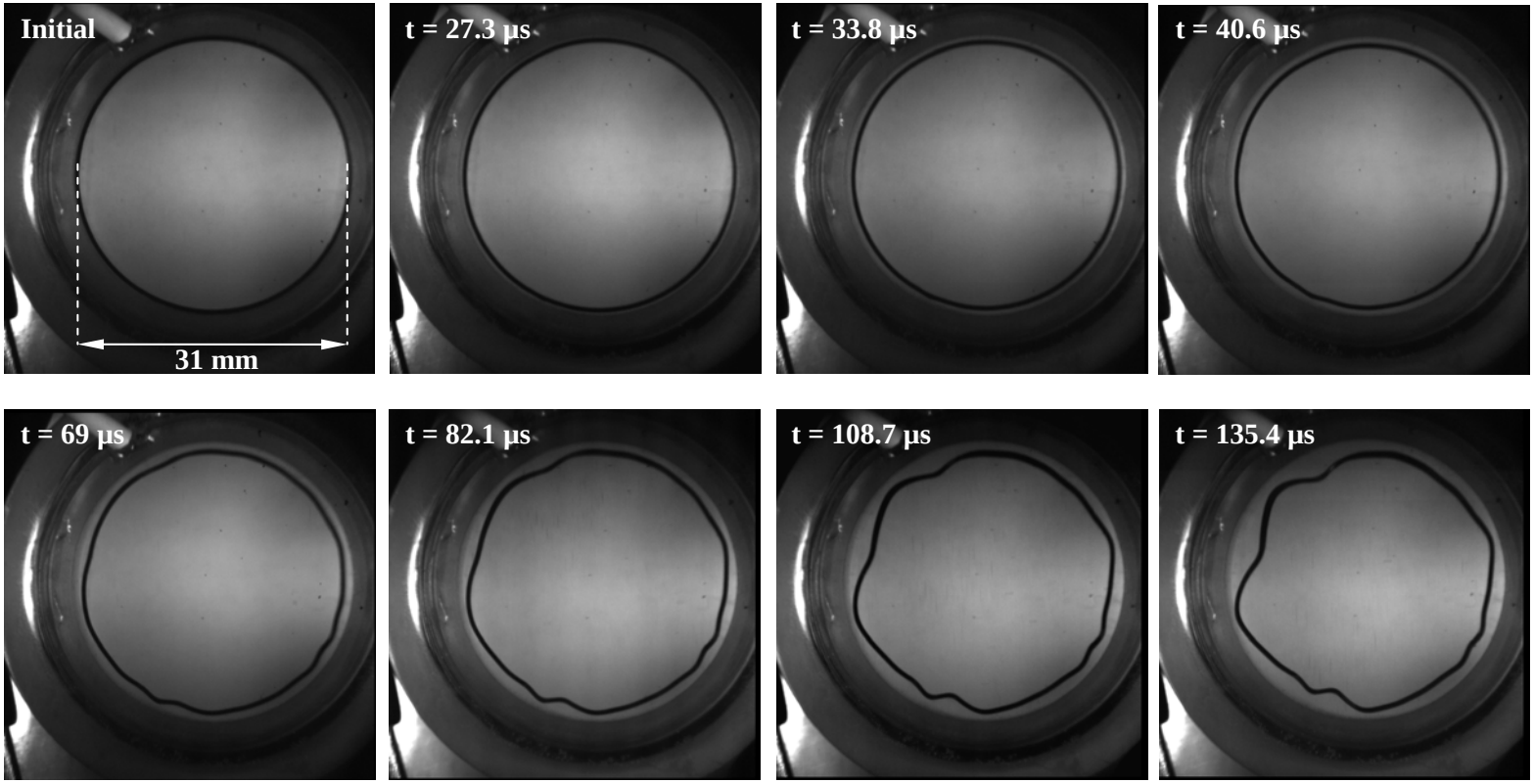

Figure 3.4: Selected sequence of images taken at different times during the deformation of a ring, for a 2 kV charge voltage.

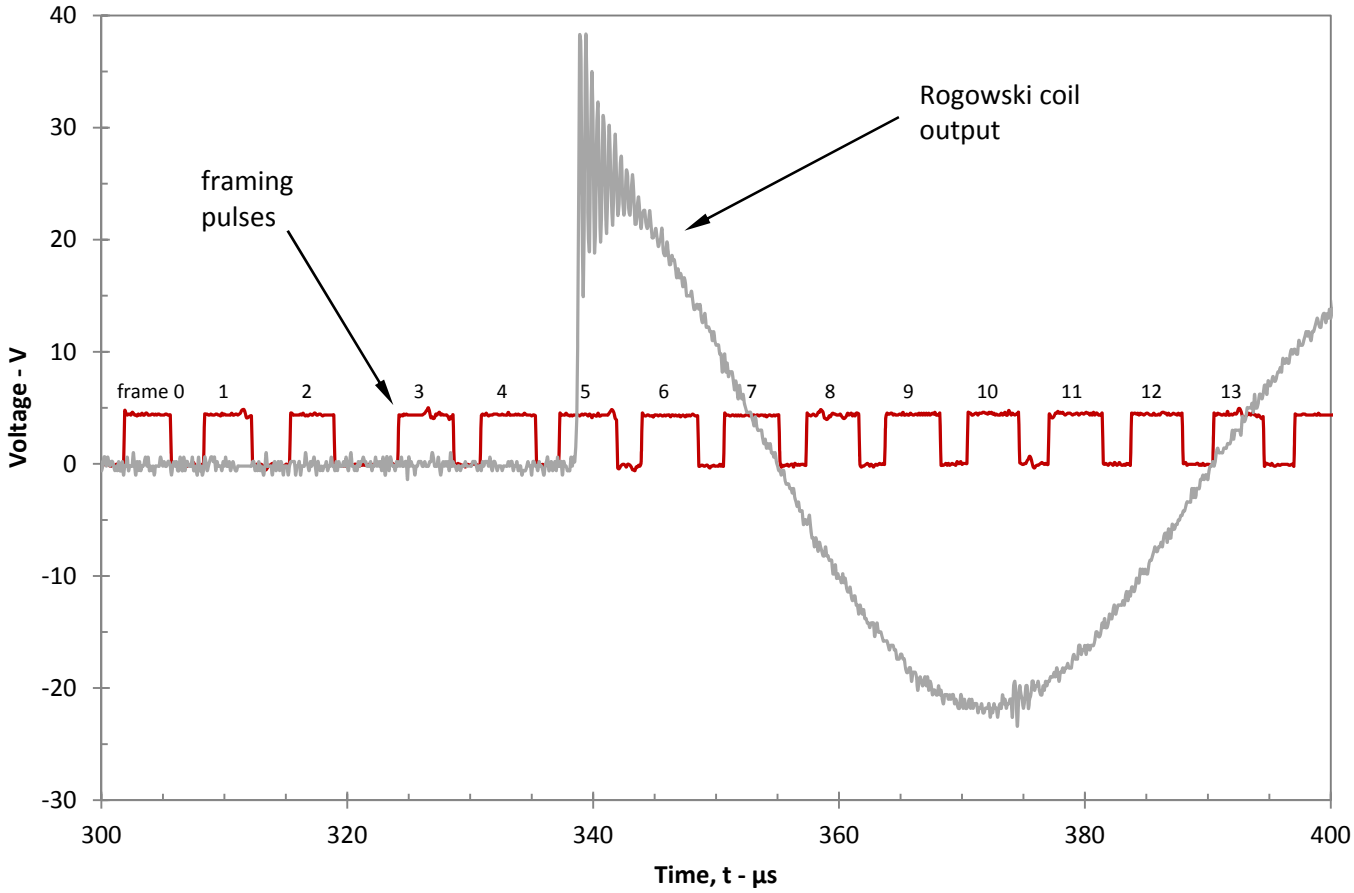

Figure 3.5: Example of a graph of the time variation of the Rogowski coil output and the framing pulses. The rising edge of each framing pulse results in an image in the high-speed camera.

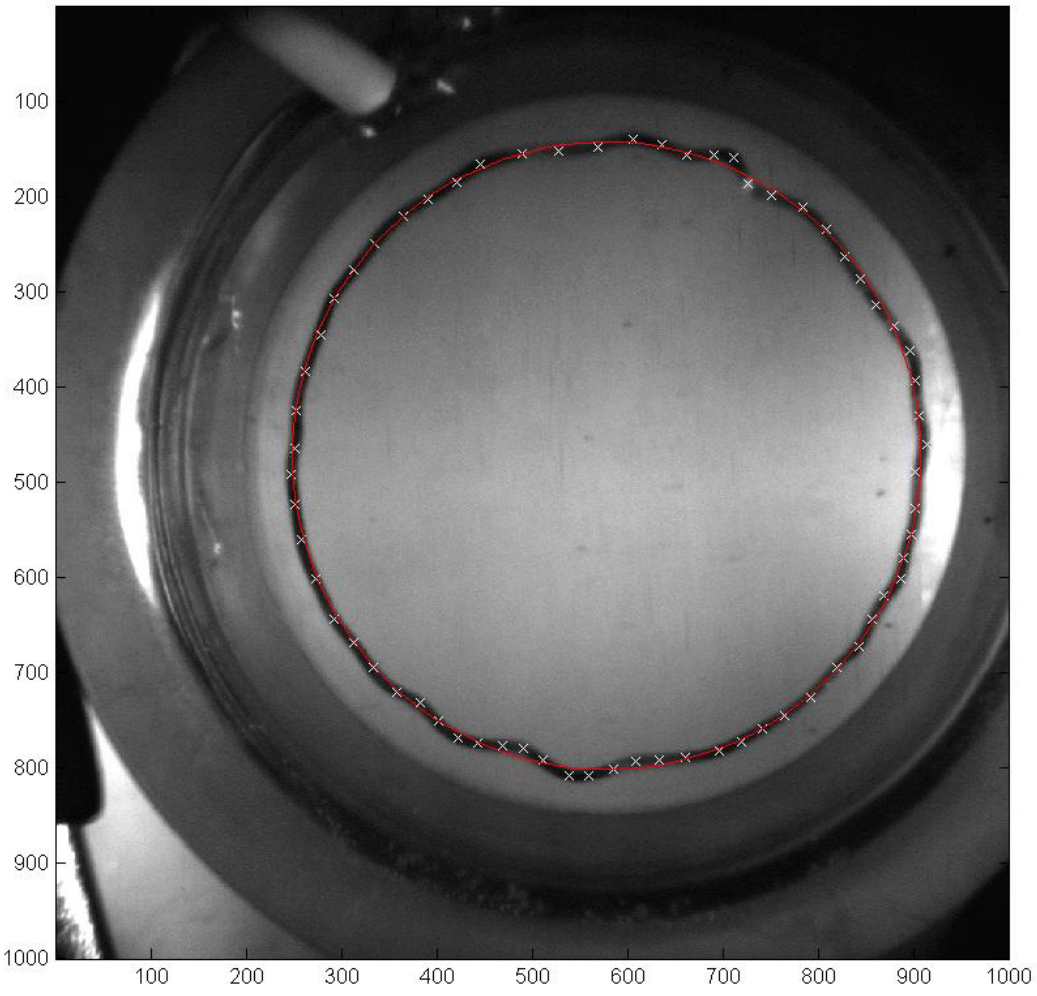

Figure 3.6: Example of a best-fit circle following the code described in the Appendix. The white crosses are the selected points along the ring specimen. The best-fit circle is represented by the red circle.

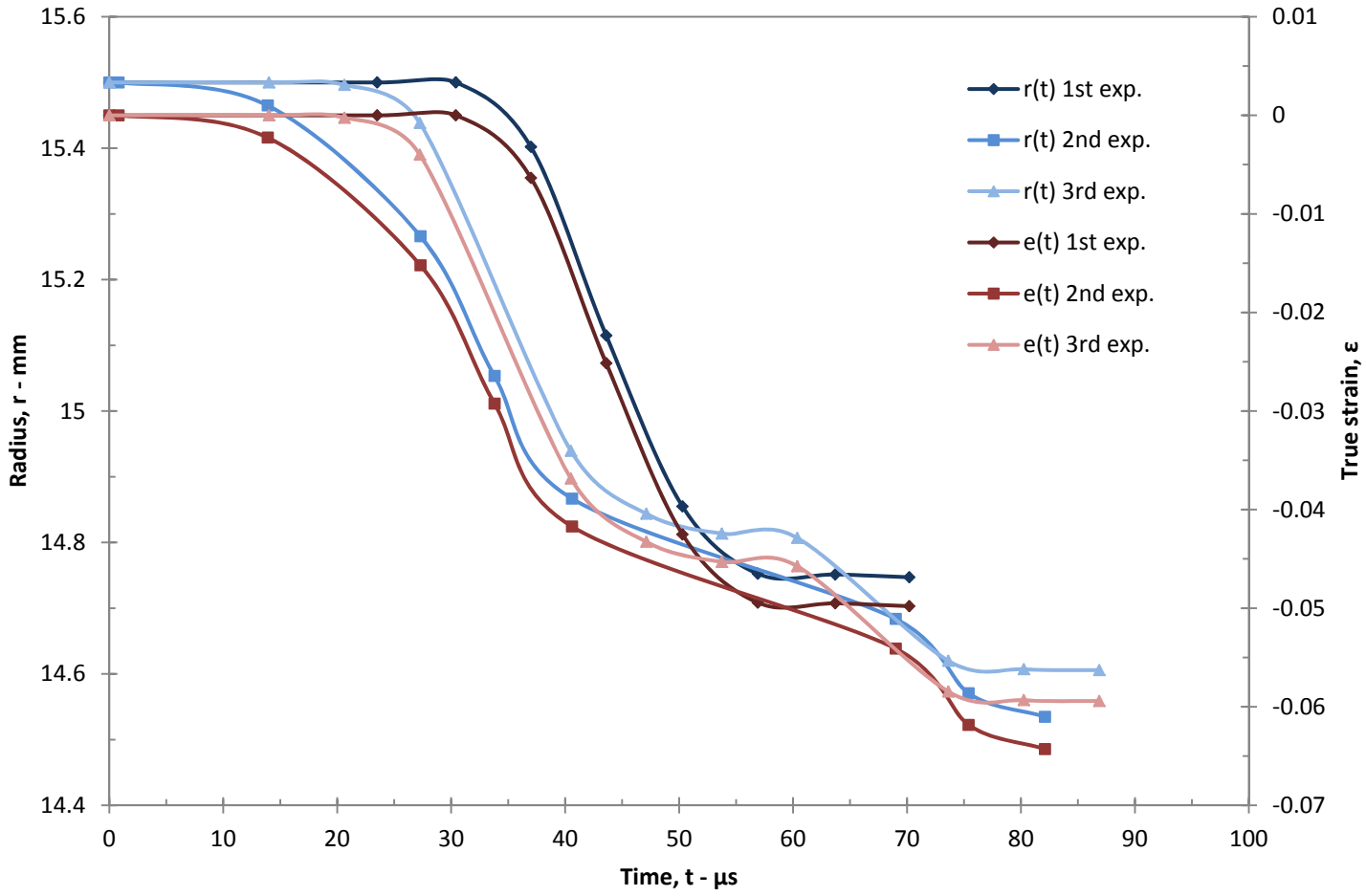

Figure 3.7: Time variation of the ring radius and the hoop strain for the three experiments performed with a 2 kV charge voltage.

Table 1: *List of the experiments and the following data: times at the onset of buckling, corresponding impulses, radii of the rings, velocities and strains.*

Charge Voltage	***Exp. N°***	***t_0 in µs***	***$\mathcal{I}(t_0)$ in Pa.s***	***$r(t_0)$ in mm***	***$V(t_0)$ in $m.s^{-1}$***	***$\varepsilon(t_0)$***
2 kV	*1*	*<50.3*	*128.94*	*14.85*	*-43*	*>-0.0425*
	2	*40.6*	*92.58*	*14.87*	*-34*	*-0.0417*
	3	*40.5*	*91.78*	*14.93*	*-38*	*-0.0368*
3 kV	*1*	*26.56*	*212.53*	*14.98*	*-83*	*-0.0341*
	2	*38.4*	*176.08*	*14.86*	*-85*	*-0.0424*
	3	*28.7*	*203.52*	*>14.54*	*-80*	*>-0.071*
4 kV	*1*	*23.7*	*297.61*	*14.82*	*-152*	*-0.0450*
	2	*24.9*	*327.01*	*>14.37*	*-138*	*>-0.0753*
	3	*24.7*	*304.42*	*14.74*	*-124*	*-0.0507*
5kV	*1*	*<26.2*	*<526.2*	*>13.7*	*-182*	*>-0.1228*
	2	*17.7*	*420.32*	*14.23*	*-217*	*-0.0856*
	3	*19.7*	*474.01*	*14.19*	*-226*	*-0.0881*

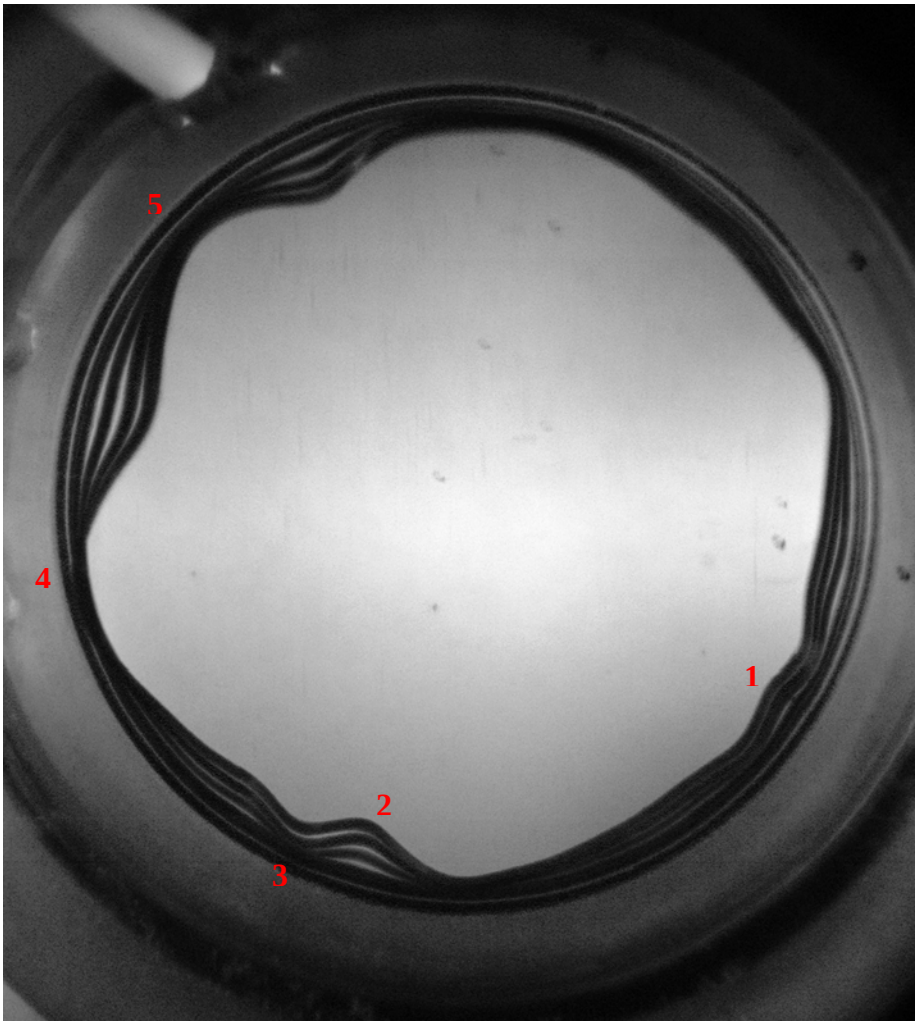

Figure 3.8: *Overlay of images taken between t = 0 and t = 135.4 μs during the deformation of the ring. This overlay corresponds to the second experiment performed with a charge level of 2 kV. The numbers in red indicate the positions studied for this experiment.*

Table 2a: List of the positions studied in the first experiment for a 2 kV charge voltage.

Position n°	***Time (µs)***	***Apparent mode n***
1	*83.60*	*25*
	103.70	*24*
	117.10	*24*
	123.80	*23*
	130.50	*23*
2	*83.60*	*9*
	103.70	*7*
	117.10	*7*
	123.80	*7*
	130.50	*7*
3	*103.70*	*7*
	117.10	*7*
	123.80	*6*
	130.50	*6*

Table 2b: List of the positions studied in the second experiment for a 2 kV charge voltage.

Position n°	***Time (µs)***	***Apparent mode n***
1	*73.63*	*19*
	80.25	*20*
	93.50	*19*
	106.75	*19*
	120.00	*18*
	133.25	*19*
	146.50	*20*
2	*106.75*	*7*
	120.00	*7*
	133.25	*7*
	146.50	*7*
3	*93.50*	*4*
	106.75	*4*
	120.00	*4*
	133.25	*4*
	146.50	*4*

Table 2c: List of the positions studied in the third experiment for a 2 kV charge voltage.

Position n°	***Time (µs)***	***Apparent mode n***
1	*75.4*	*23*
	82.1	*23*
	108.7	*23*
	135.4	*22*
2	*75.4*	*16*
	82.1	*16*
	108.7	*15*
	135.4	*15*
3	*75.4*	*20*
	82.1	*20*
	108.7	*19*
	135.4	*19*
4	*82.1*	*6*
	108.7	*6*
	135.4	*6*
5	*82.1*	*3*
	108.7	*3*
	135.4	*3*

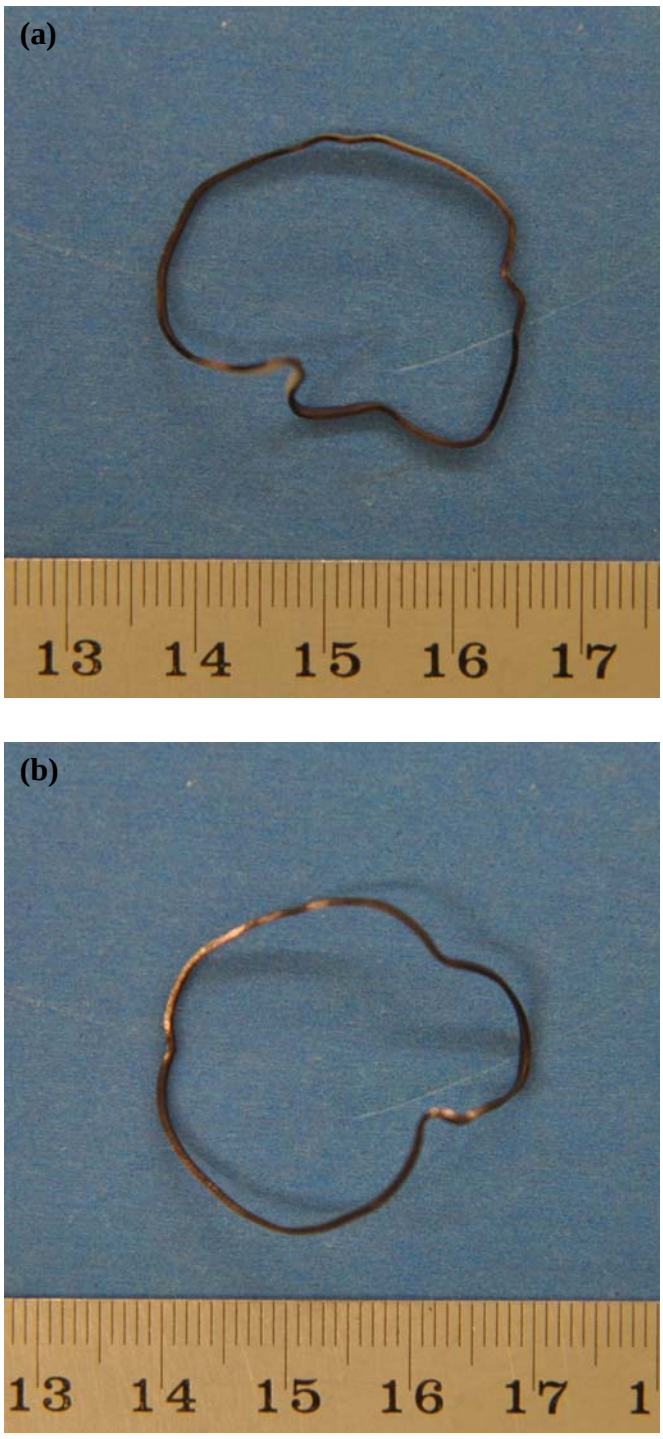

Figure 3.9: Photographs of the ring specimens at the end of the second (a) and third (b) experiments performed with a 2 kV charge level.

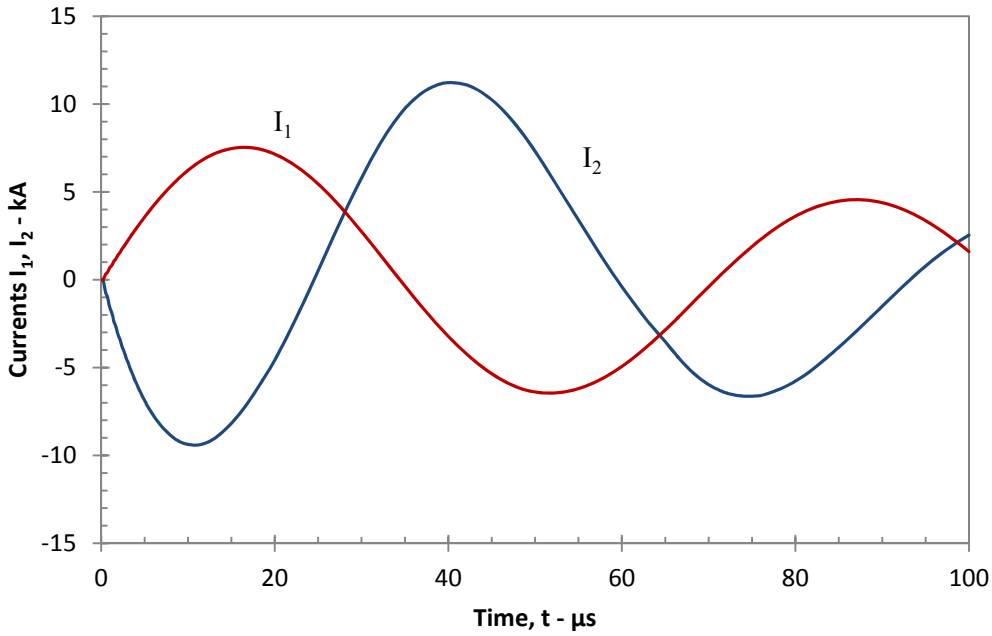

Figure 3.10: Currents I_1 and I_2 as functions of time, for a 3 kV charge voltage.

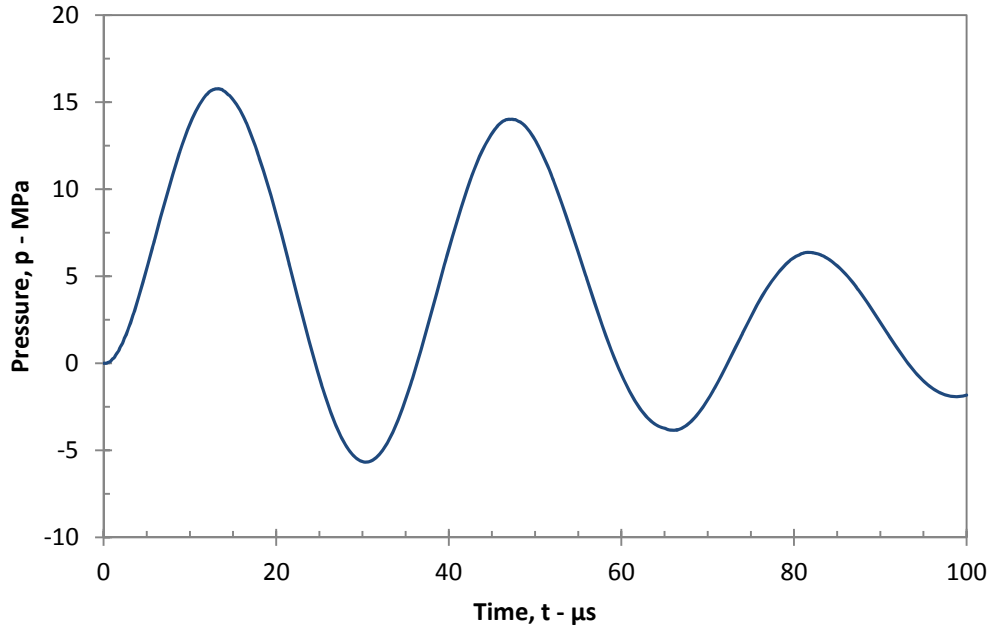

Figure 3.11: Pressure p acting on the ring as a function of time for a 3 kV charge voltage.

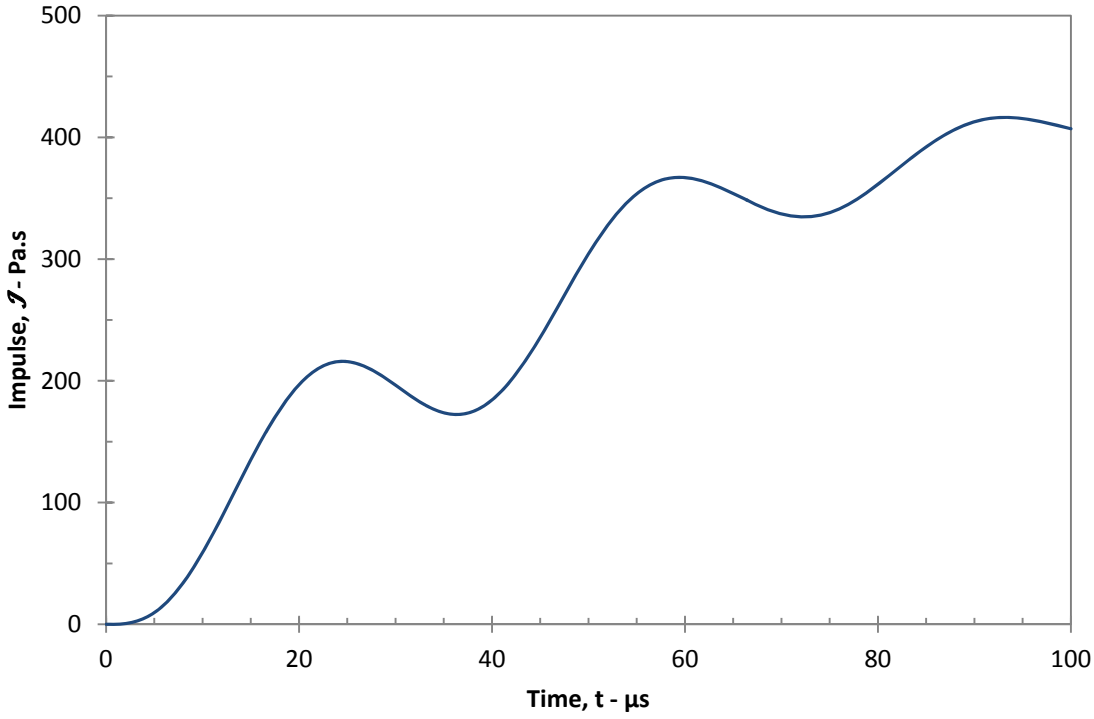

Figure 3.12: Impulse $\mathcal{I}$ in Pa.s, corresponding to the previous pressure, for a 3 kV charge level.

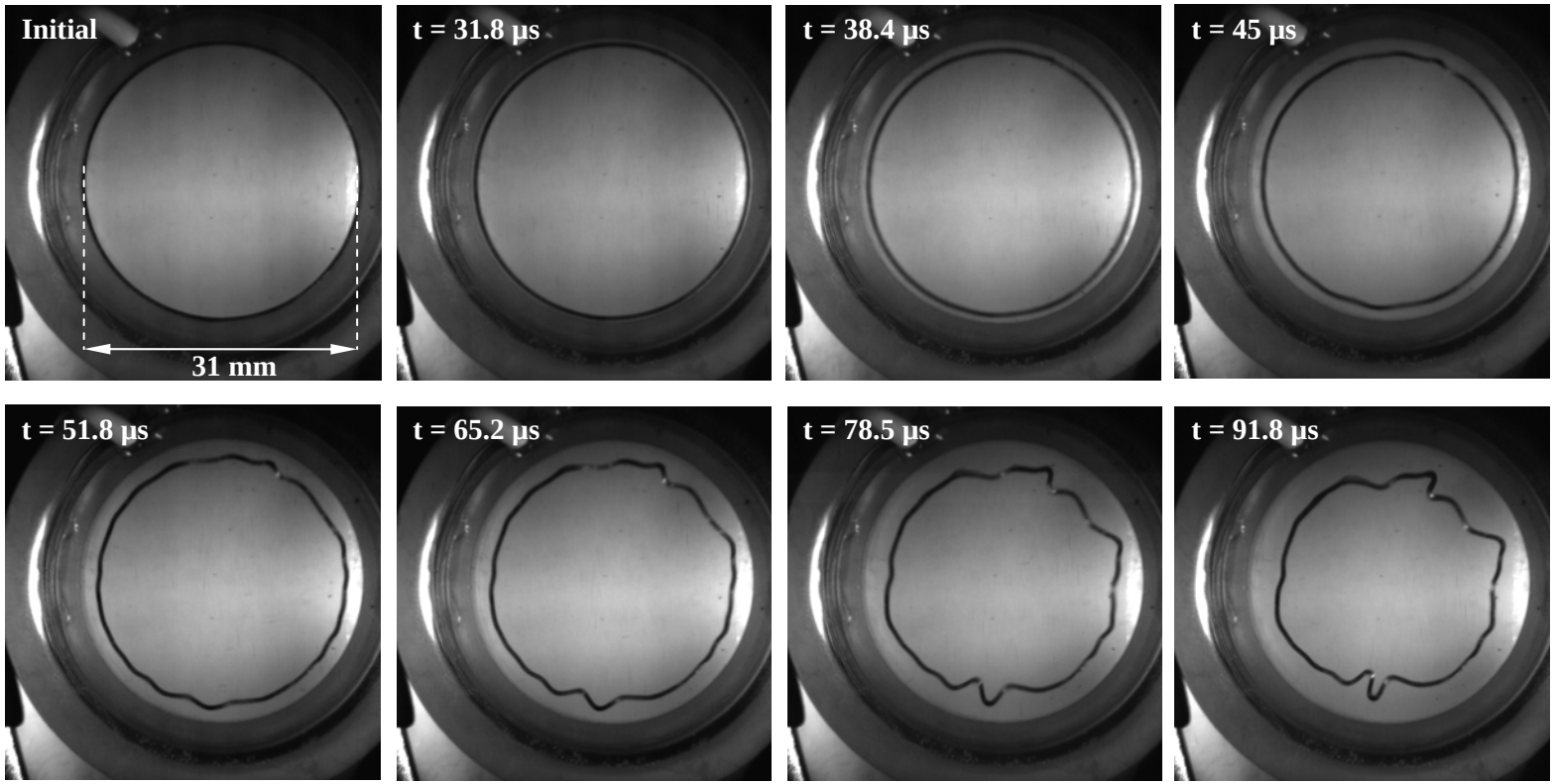

Figure 3.13: Selected sequence of images taken at different times during the deformation of a ring, for a 3 kV charge level.

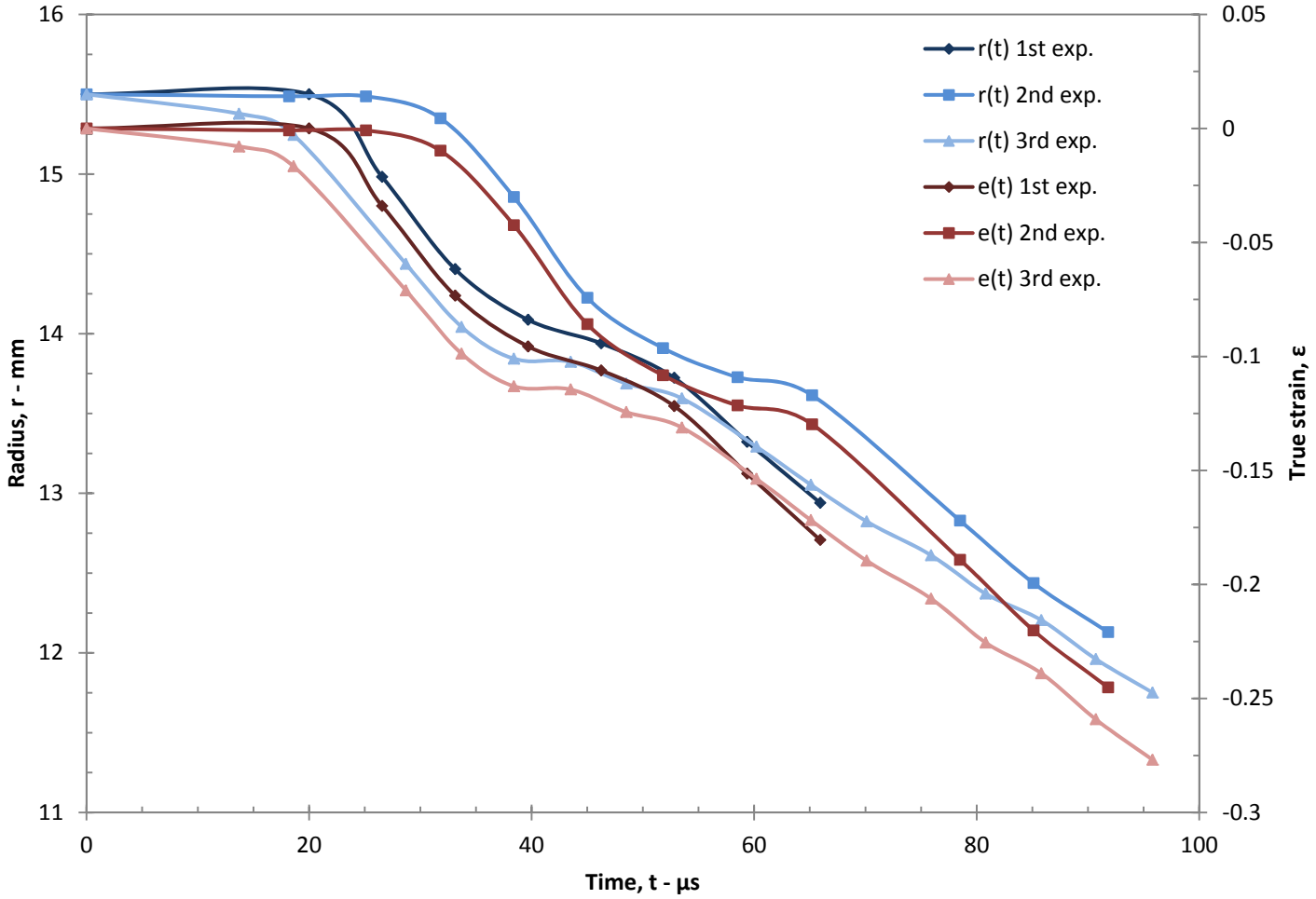

Figure 3.14: Time variation of the ring radius and the hoop strain for the three experiments performed with a 3 kV charge voltage.

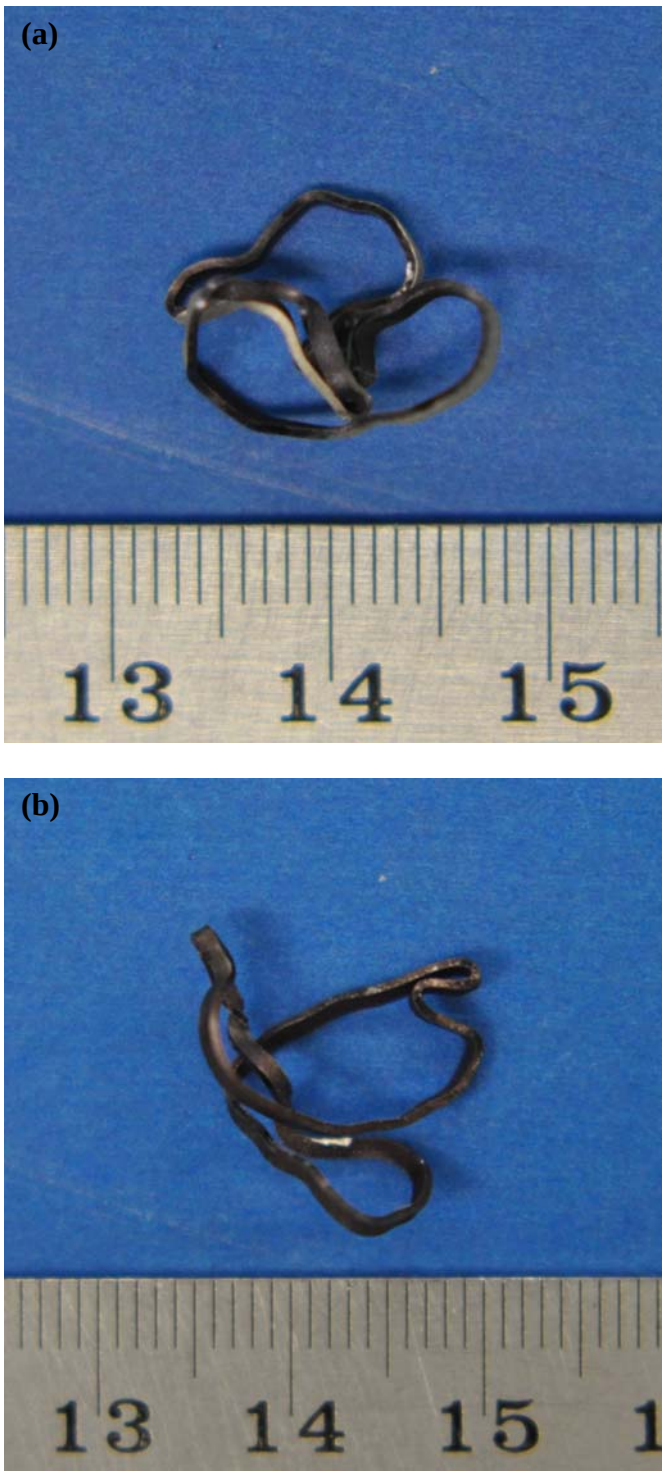

Figure 3.15: Photographs of the ring specimens at the end of the second (a) and third (b) experiments performed with a 3 kV charge level.

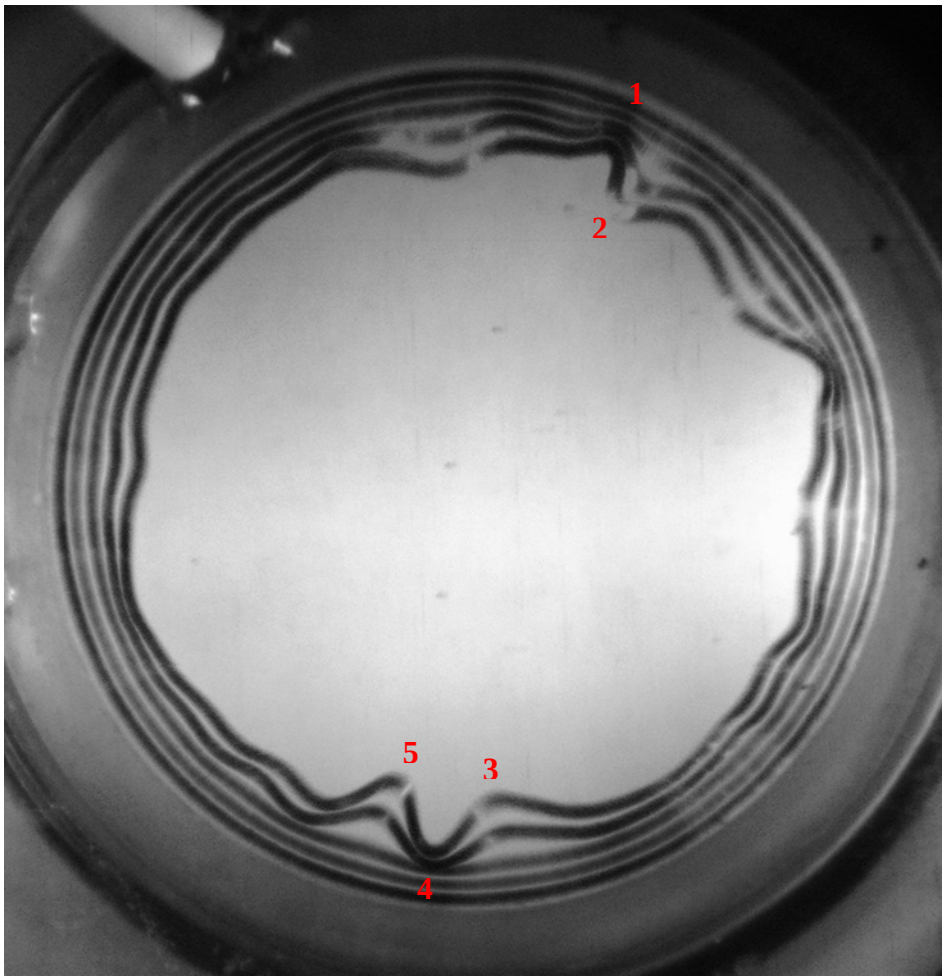

Figure 3.16: Overlay of images captured between t = 0 and t = 91.8 μs during the deformation of the ring. This overlay corresponds to the second experiment performed with a charge level of 3 kV. The numbers in red indicate the positions studied for this experiment.

Table 3a: List of the positions studied in the first experiment for a 3 kV charge voltage.

Position n°	***Time (µs)***	***Apparent mode n***
1	*39.6875*	*22*
	46.2500	*21*
	52.8125	*22*
	59.3750	*18*
	65.9375	*19*
2	*39.6875*	*25*
	46.2500	*25*
	52.8125	*24*
	59.3750	*26*
	65.9375	*26*
3	*39.6875*	*28*
	46.2500	*27*
	52.8125	*27*
	59.3750	*27*
	65.9375	*26*
4	*59.3750*	*29*
	65.9375	*30*
5	*52.8125*	*18*
	59.3750	*17*
	65.9375	*17*
6	*39.6875*	*19*
	46.2500	*19*
	52.8125	*18*
	59.3750	*18*
	65.9375	*18*

Table 3b: List of the positions studied in the second experiment for a 3 kV charge voltage.

Position n°	***Time (µs)***	***Apparent mode n***
1	*45.0*	*27*
	51.8	*26*
	58.5	*26*
	65.2	*26*
2	*51.8*	*23*
	58.5	*23*
	65.2	*22*
3	*51.8*	*32*
	58.5	*30*
	65.2	*32*
4	*51.8*	*18*
	58.5	*18*
	65.2	*18*
5	*51.8*	*19*
	58.5	*18*
	65.2	*19*

Table 3c: List of the positions studied in the third experiment for a 3 kV charge voltage.

Position n°	***Time (µs)***	***Apparent mode n***
1	*48.5*	*33*
	53.5	*34*
	60.2	*34*
2	*38.4*	*27*
	48.5	*25*
	53.5	*25*
	60.2	*25*
3	*43.5*	*25*
	53.5	*25*
	60.2	*23*
	65.1	*24*
4	*38.4*	*13*
	43.5	*13*
	60.2	*13*
	65.1	*13*
	75.9	*13*

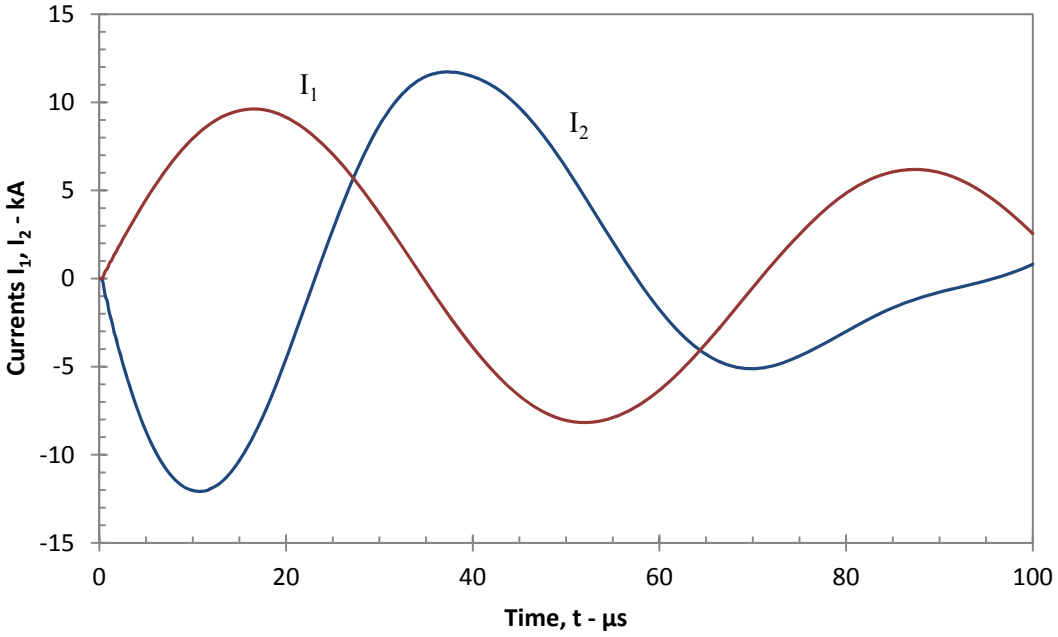

Figure 3.17: Currents I_1 and I_2 as functions of time, for a 4 kV charge voltage.

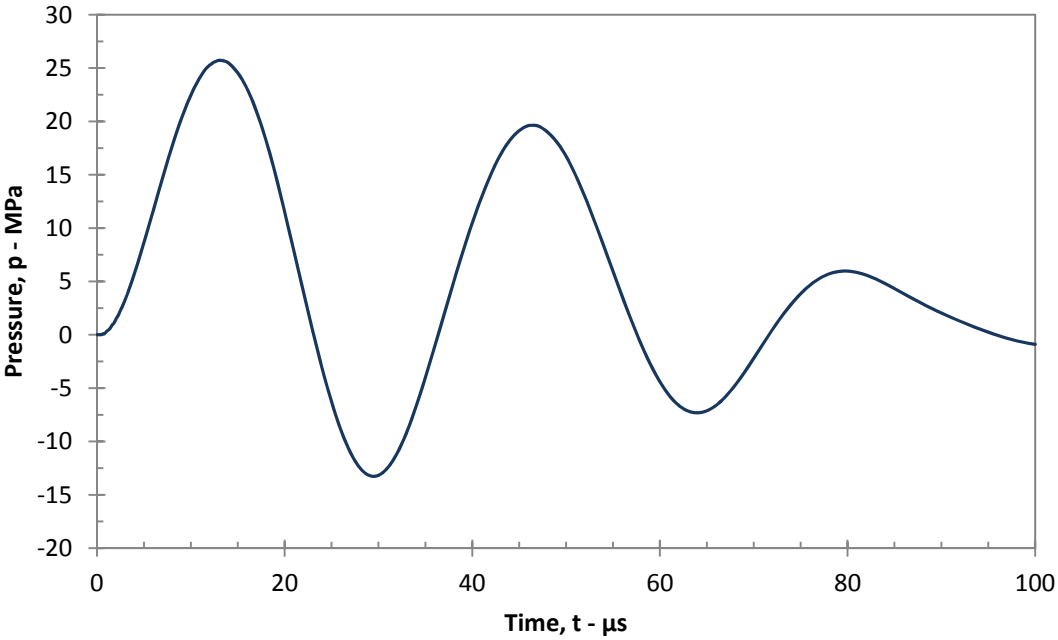

Figure 3.18: Pressure p acting on the ring as a function of time for a 4 kV charge voltage.

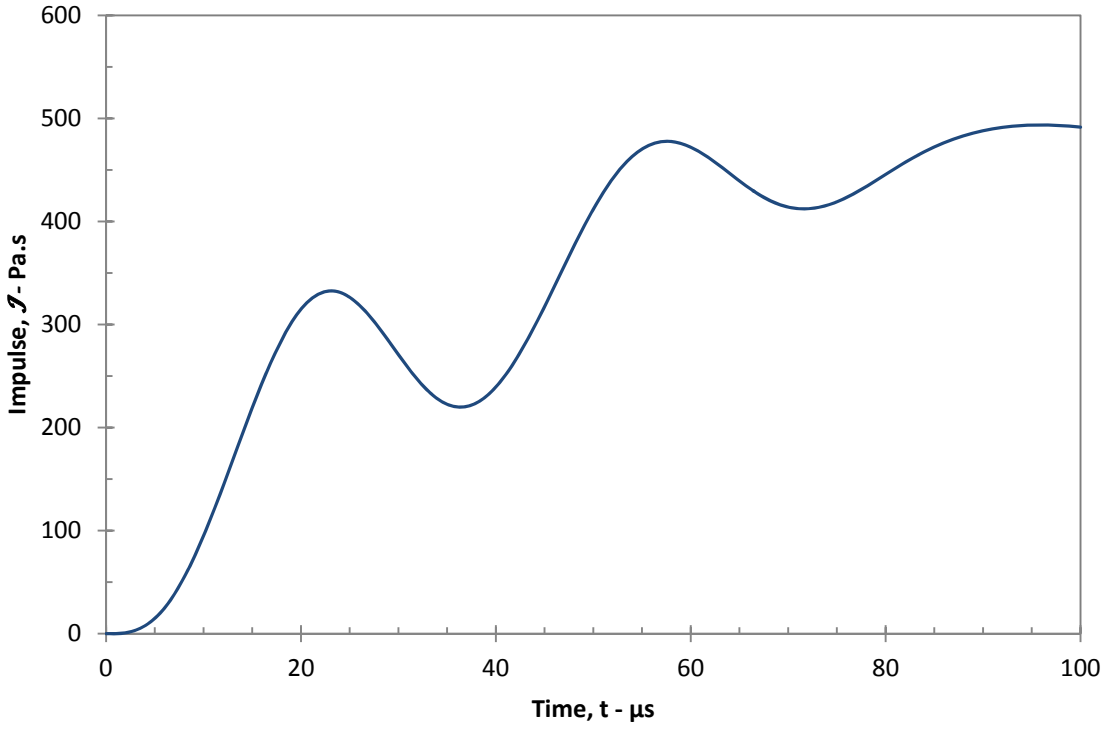

Figure 3.19: Impulse $\mathcal{I}$ in Pa.s, corresponding to the previous pressure, for a 4 kV charge level.

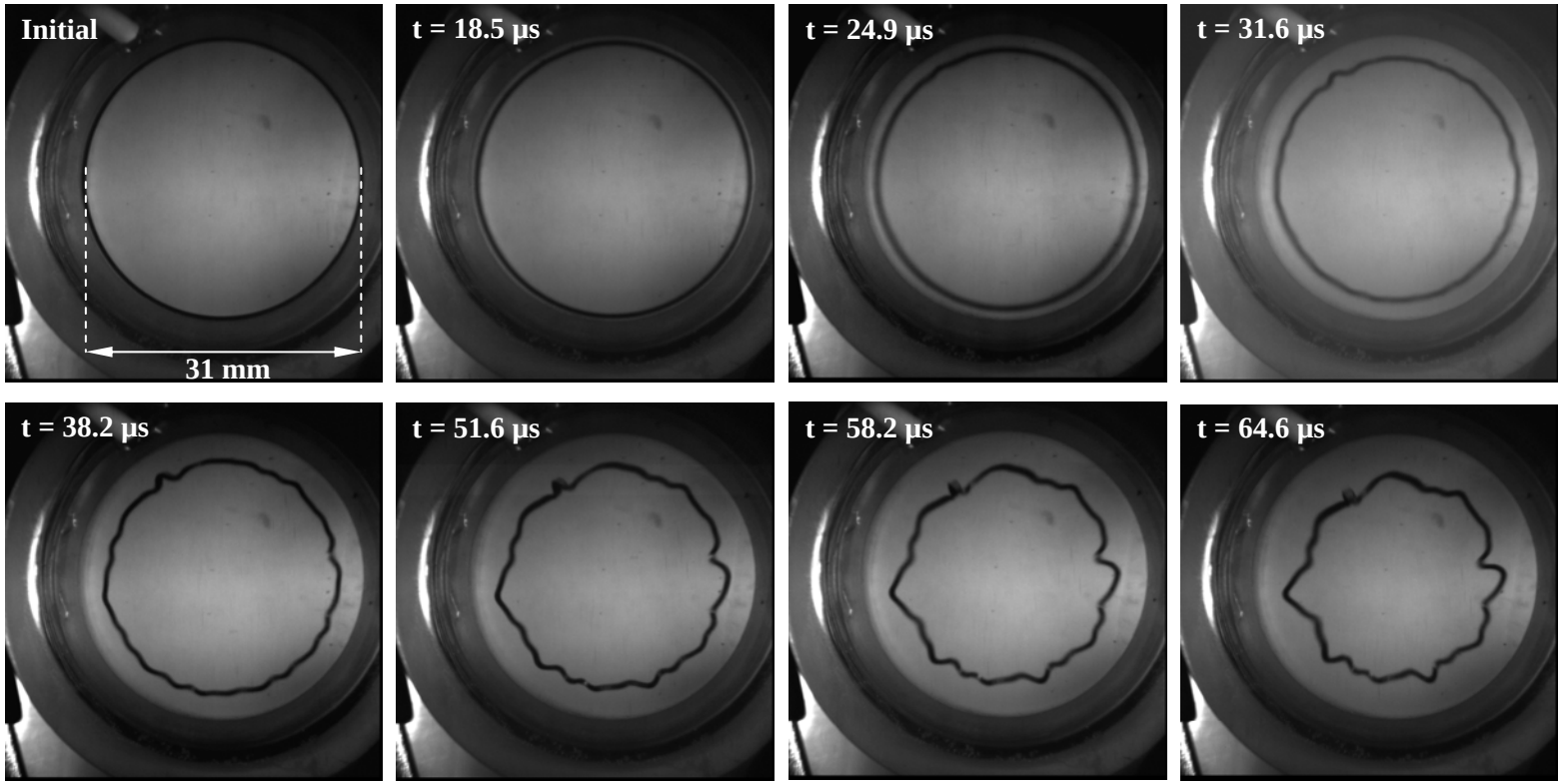

Figure 3.20: Selected sequence of images taken at different times during the deformation of a ring, for a 4 kV charge level.

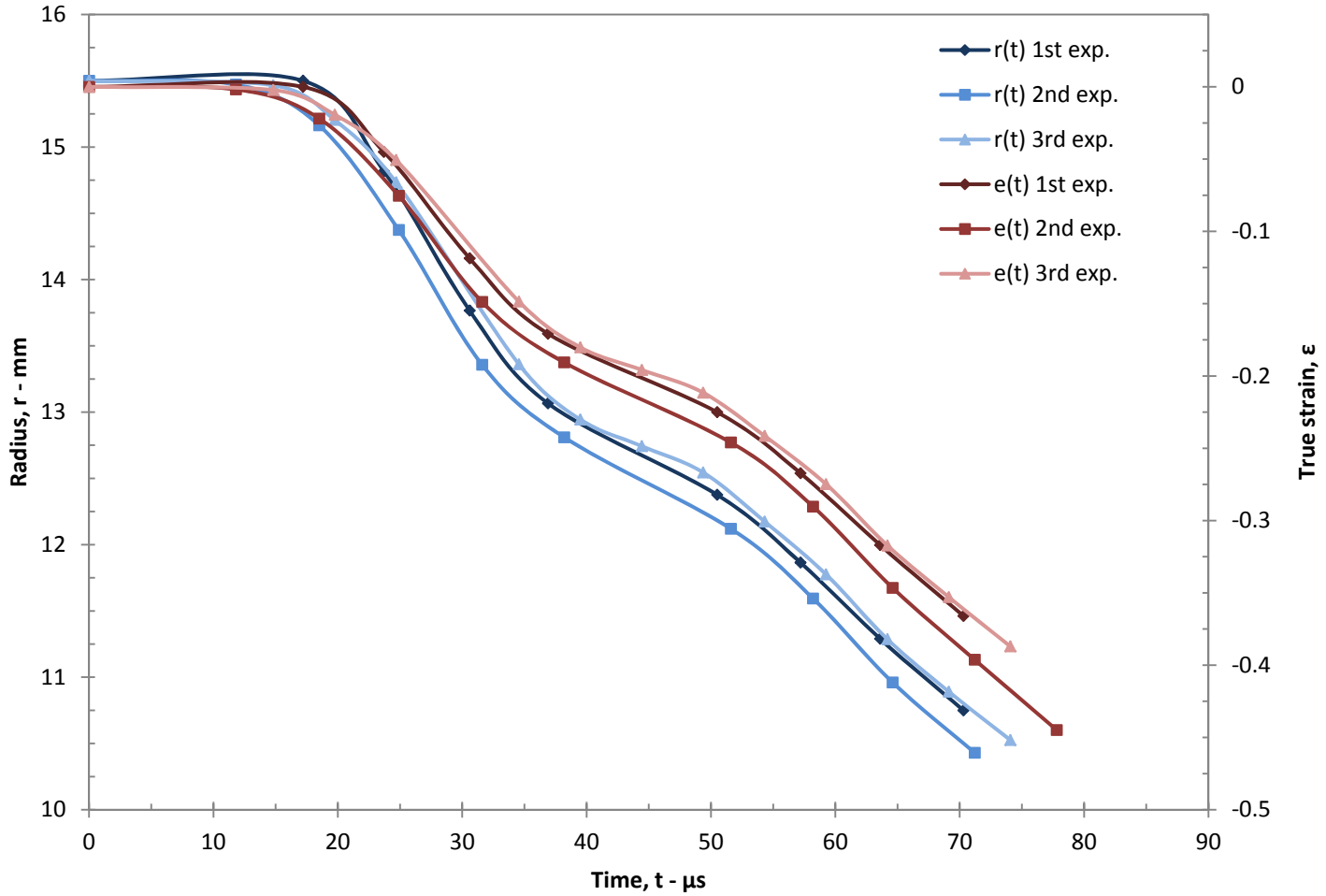

Figure 3.21: Time variation of the ring radius and the hoop strain for the three experiments performed with a 4 kV charge voltage.

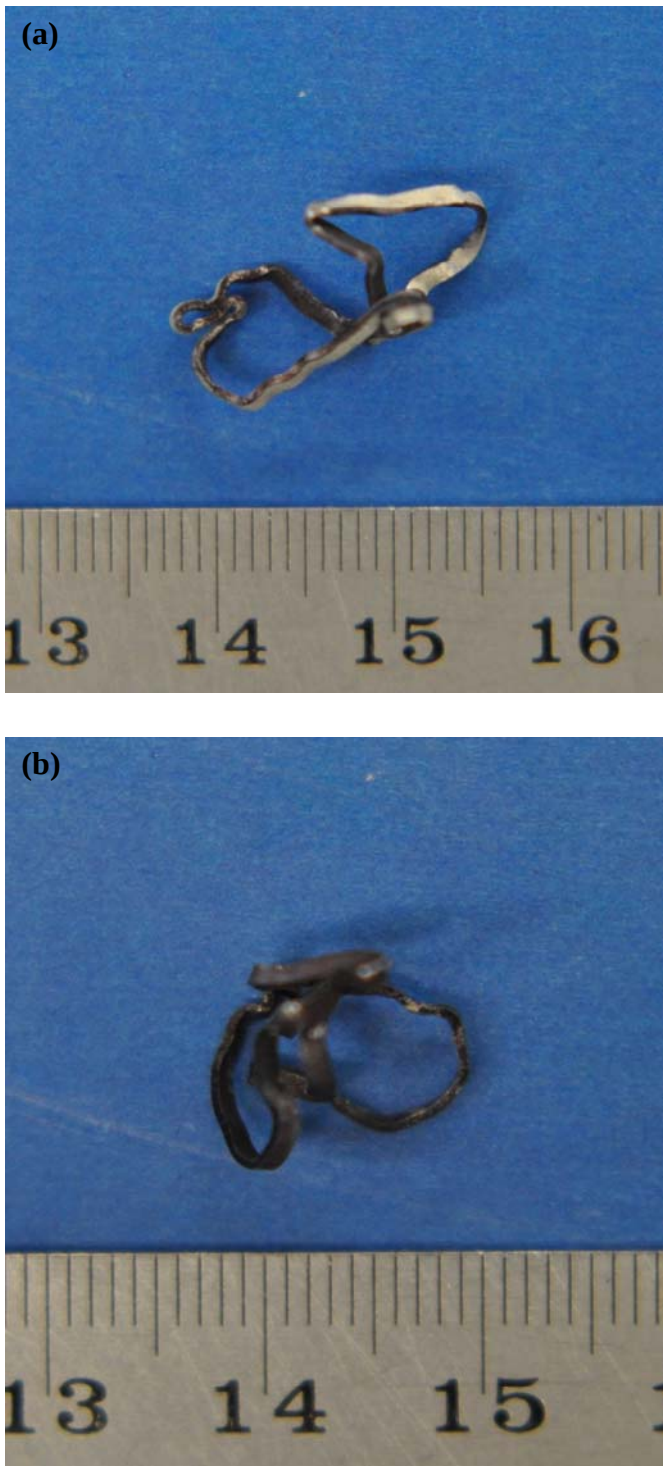

Figure 3.22: Photographs of the ring specimens at the end of the second (a) and third (b) experiments performed with a 4 kV charge level.

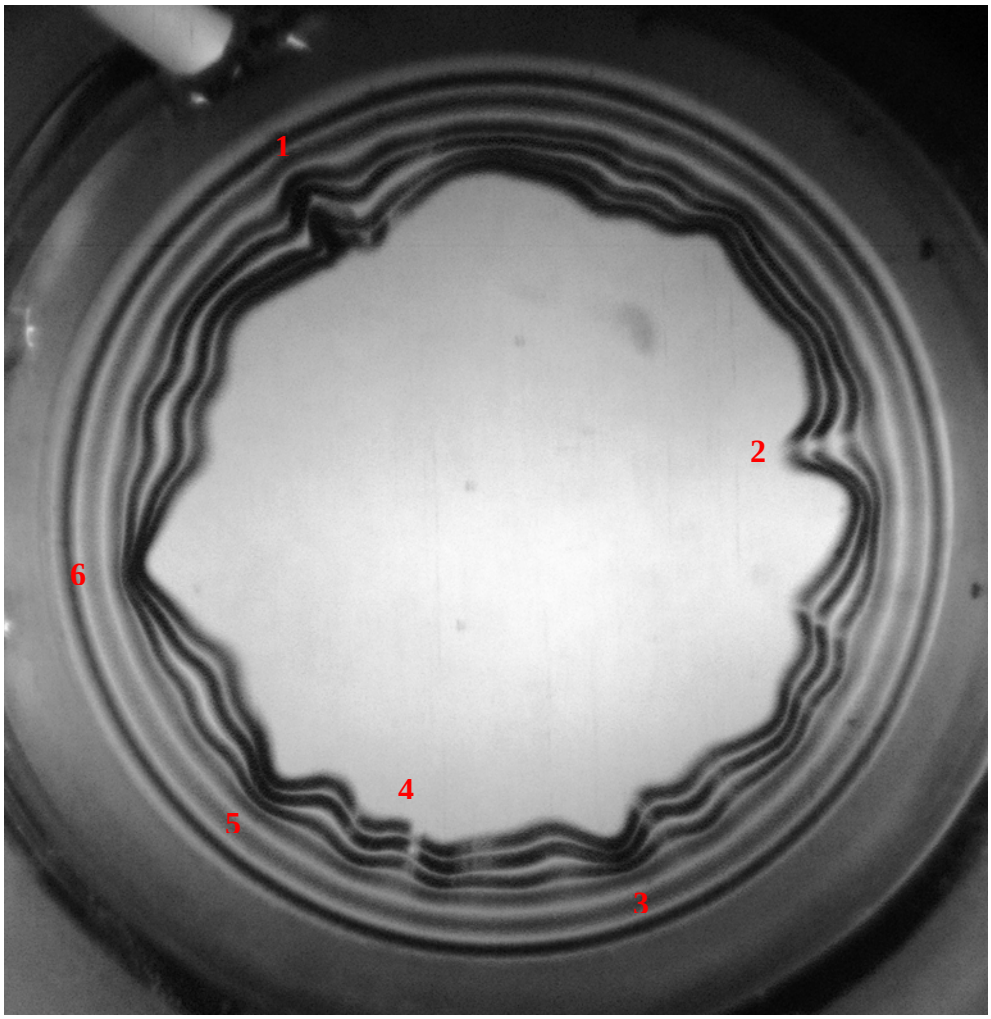

Figure 3.23: Overlay of images captured between t = 0 and t = 77.8 μs during the deformation of the ring. This overlay corresponds to the second experiment performed with a charge level of 4 kV. The numbers in red indicate the positions studied for this experiment.

Table 4a: List of the positions studied in the first experiment for a 4 kV charge voltage.

Position n°	***Time (µs)***	***Apparent mode n***
1	*10.4*	*26*
	17.2	*27*
	30.6	*28*
2	*17.2*	*26*
	30.6	*25*
	36.9	*25*
	43.6	*26*
	50.5	*24*
3	*17.2*	*25*
	30.6	*25*
	36.9	*25*
	43.6	*24*
	50.5	*23*
4	*17.2*	*25*
	30.6	*25*
	36.9	*24*
	43.6	*23*
	50.5	*22*
5	*17.2*	*25*
	30.6	*25*
6	*30.6*	*22*
	36.9	*21*
	43.6	*22*
	50.5	*21*
7	*30.6*	*27*
	36.9	*25*
	43.6	*25*
	50.5	*24*

Table 4b: List of the positions studied in the second experiment for a 4 kV charge voltage.

Position n°	***Time (µs)***	***Apparent mode n***
1	*31.6*	*26*
	38.2	*28*
2	*38.2*	*27*
	51.6	*25*
	58.2	*25*
3	*38.2*	*21*
	51.6	*21*
	58.2	*21*
	64.6	*21*
	71.2	*21*
	77.8	*22*
4	*38.2*	*24*
	51.6	*24*
	58.2	*21*
	64.6	*23*
5	*38.2*	*21*
	51.6	*20*
	58.2	*21*
	64.6	*21*

Table 4c: List of the positions studied in the third experiment for a 4 kV charge voltage.

Position n°	***Time (µs)***	***Apparent mode n***
1	*57*	*28*
	63.6	*27*
	68.6	*27*
	73.5	*27*
	79.2	*28*
2	*63.6*	*28*
	68.6	*30*
	73.5	*29*
	79.2	*31*
3	*57*	*28*
	63.6	*27*
	68.6	*27*
	73.5	*26*
	79.2	*26*
4	*57*	*20*
	63.6	*20*
	68.6	*19*
	73.5	*20*
	79.2	*20*

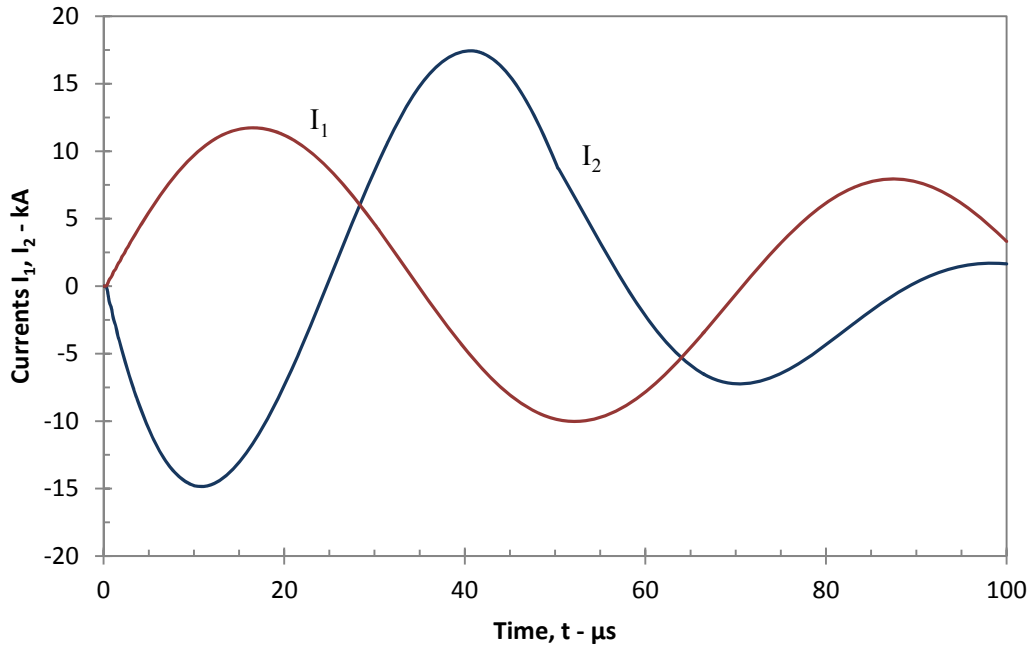

Figure 3.24: Currents I_1 and I_2 as functions of time for a 5 kV charge voltage.

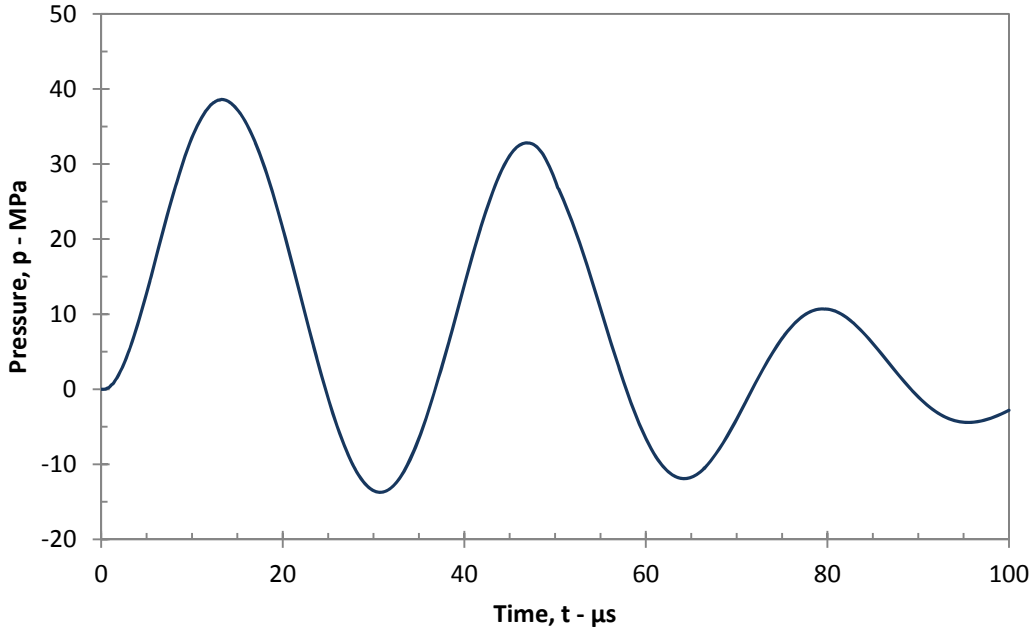

Figure 3.25: Pressure p acting on the ring as a function of time for a 5 kV charge voltage.

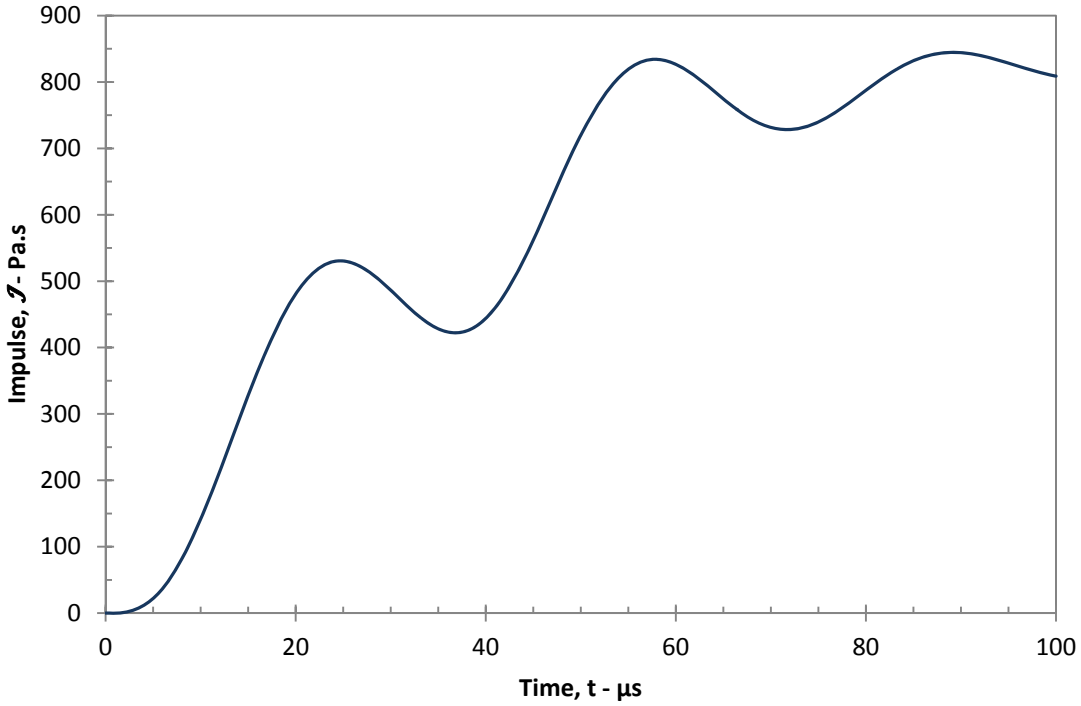

Figure 3.26: Impulse $\mathcal{I}$ in Pa.s, corresponding to the previous pressure, for a 4 kV charge level.

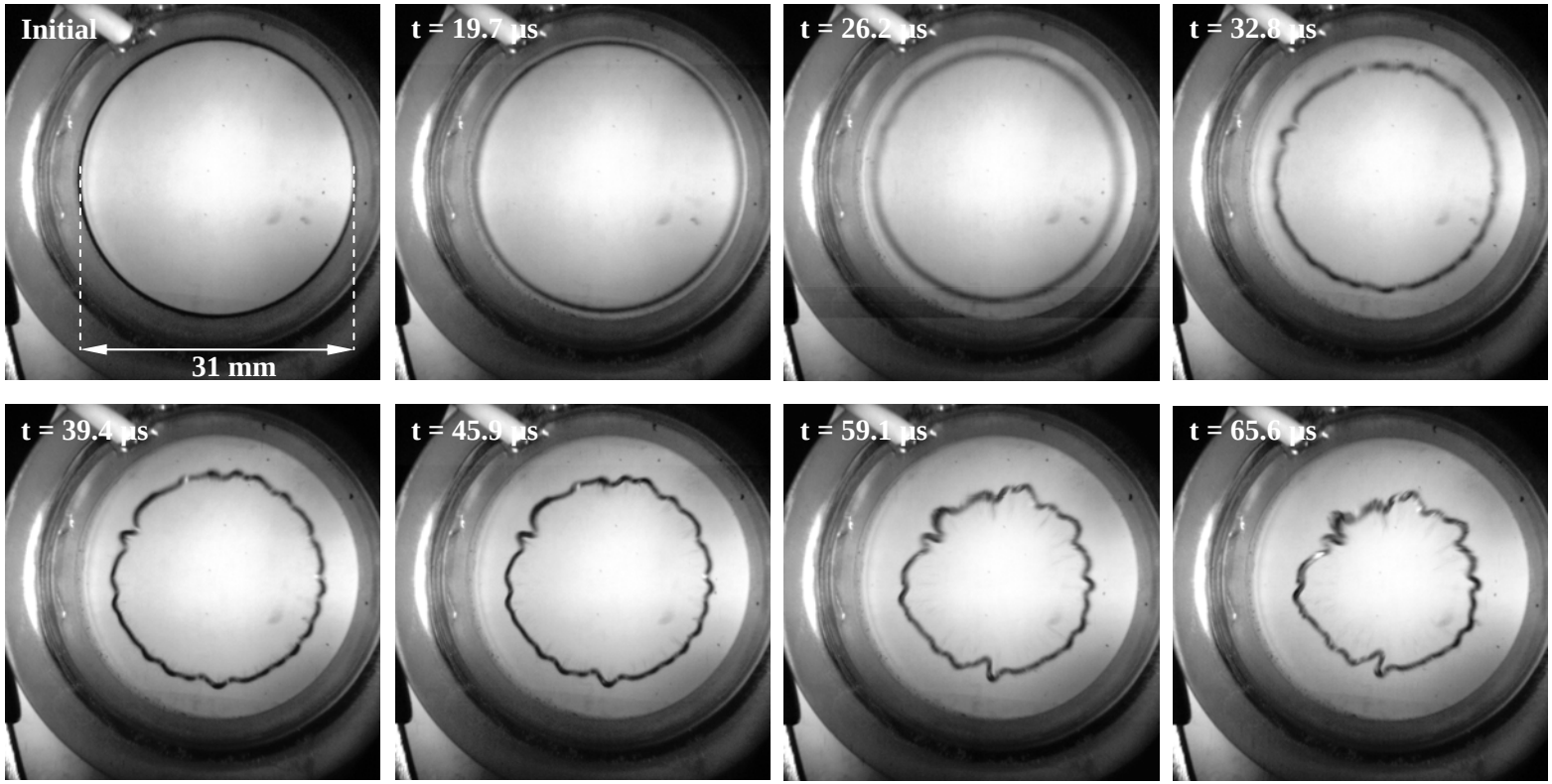

Figure 3.27: Selected sequence of images taken at different times during the deformation of a ring, for a 5 kV charge level.

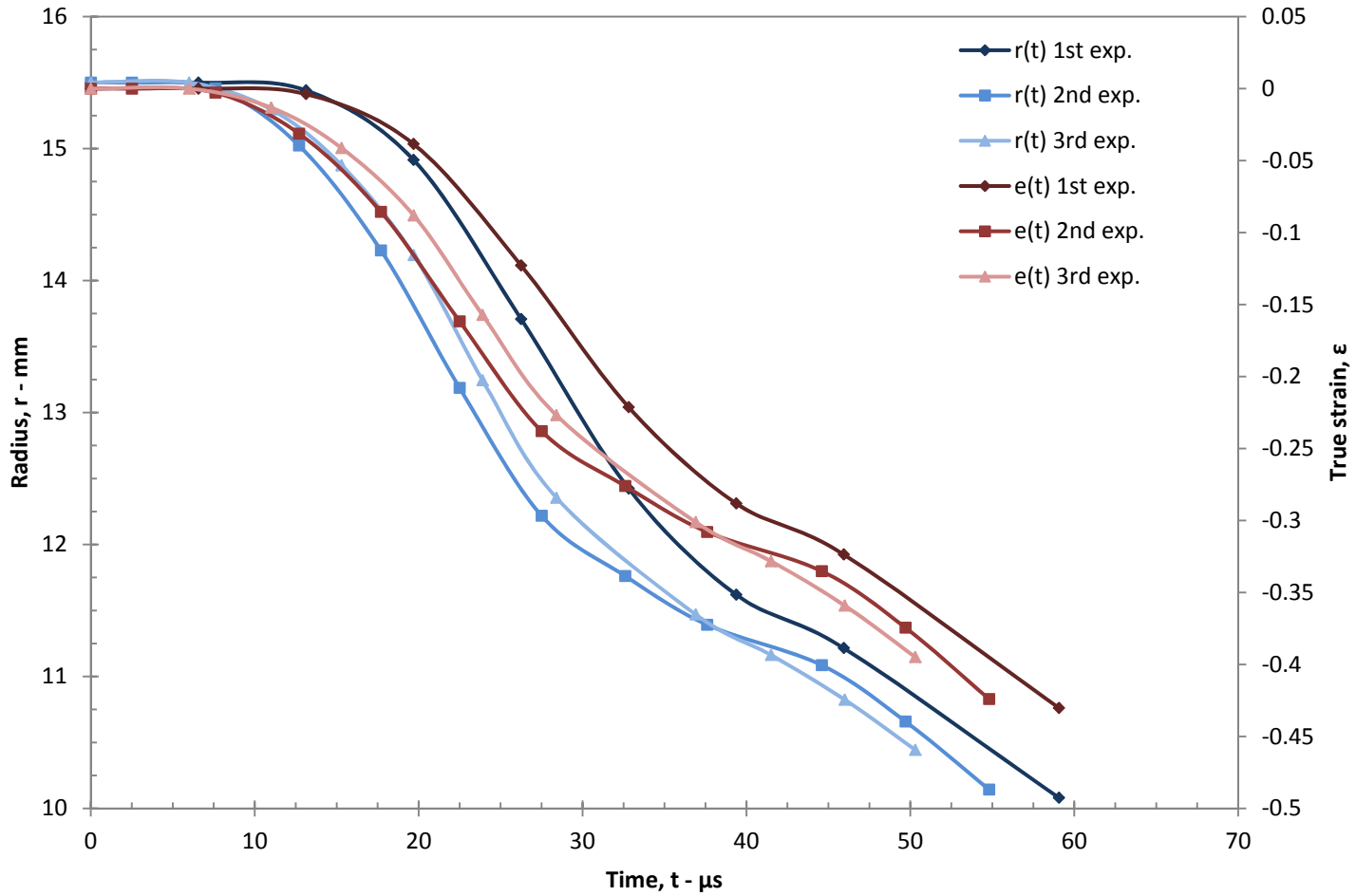

Figure 3.28: Time variation of the ring radius and the hoop strain for the 3 experiments performed with a 5 kV charge voltage.

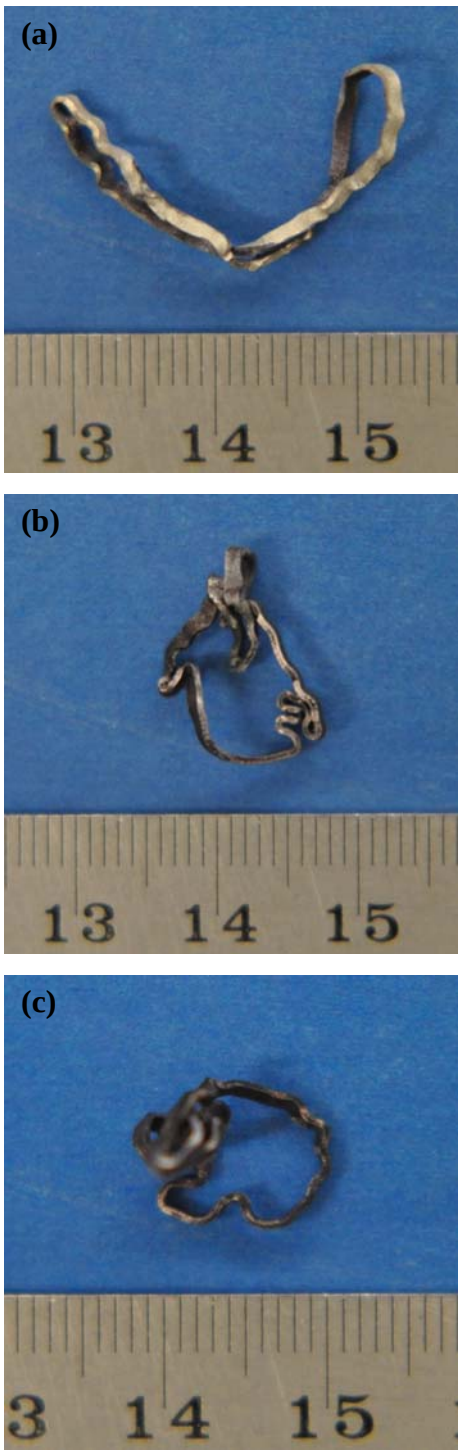

Figure 3.29: Photographs of the ring specimens at the end of the first (a), second (b) and third (c) experiments performed with a 5 kV charge level.

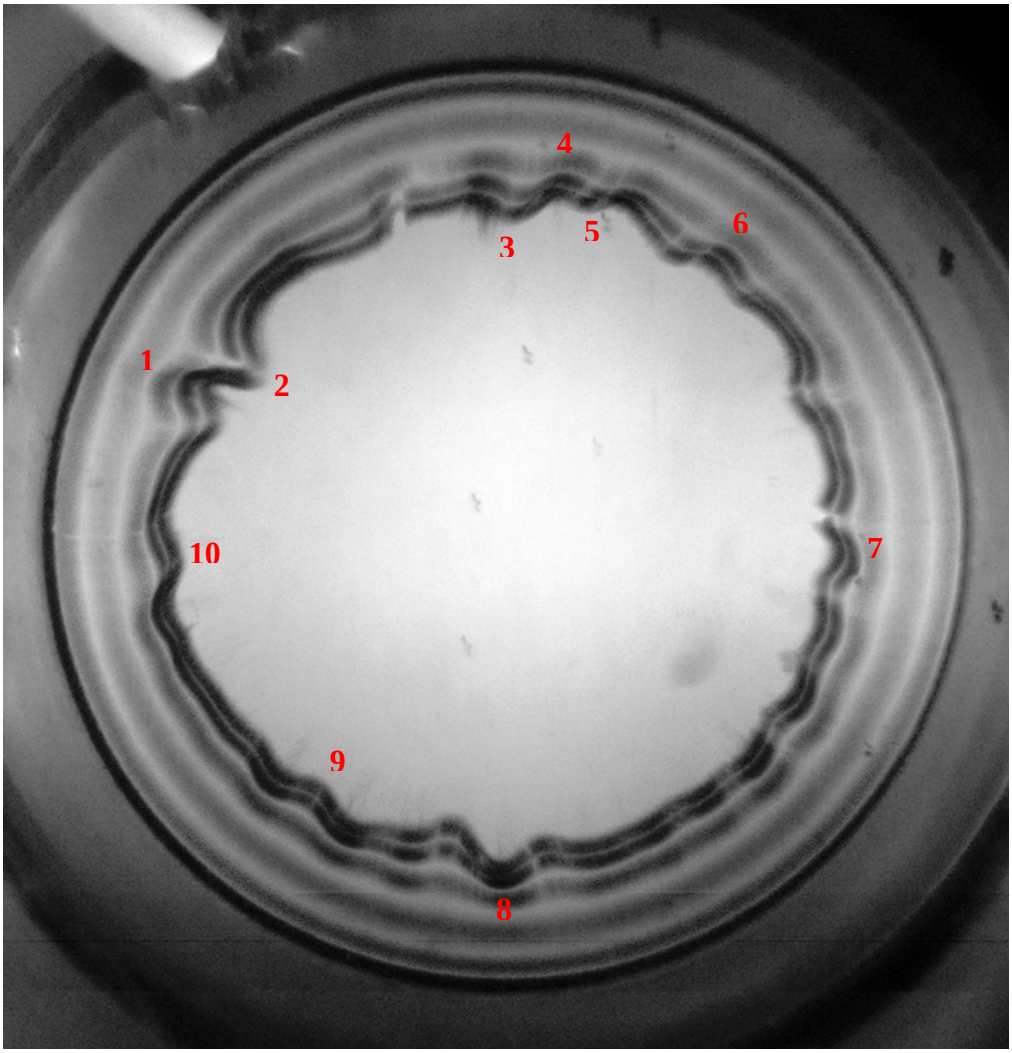

Figure 3.30: Overlay of images captured between t = 0 and t = 45.9 μs during the deformation of the ring. This overlay corresponds to the first experiment performed with a charge level of 5 kV. The numbers in red indicate the positions studied for this experiment.

Table 5a: List of the positions studied in the first experiment for a 5 kV charge voltage.

Position n°	***Time (µs)***	***Apparent mode n***
1	*39.4*	*31*
2	*39.4*	*26*
3	*39.4*	*44*
4	*39.4*	*33*
5	*39.4*	*35*
6	*39.4*	*28*
7	*39.4*	*29*
8	*39.4*	*24*
9	*39.4*	*26*
10	*39.4*	*28*

Table 5b: List of the positions studied in the second experiment for a 5 kV charge voltage.

Position n°	***Time (µs)***	***Apparent mode n***
1	*37.6*	*21*
2	*37.6*	*20*
3	*37.6*	*33*
4	*37.6*	*30*
5	*37.6*	*22*
6	*37.6*	*20*
7	*37.6*	*22*

Table 5c: List of the positions studied in the third experiment for a 5 kV charge voltage.

Position n°	***Time (µs)***	***Apparent mode n***
1	*36.9*	*33*
2	*36.9*	*31*
3	*36.9*	*33*
4	*36.9*	*33*
5	*36.9*	*34*
6	*36.9*	*34*
7	*36.9*	*33*
8	*36.9*	*32*
9	*36.9*	*23*
10	*36.9*	*25*
11	*28.4*	*26*
	36.9	*27*
12	*28.4*	*30*
	36.9	*35*
13	*28.4*	*30*
	36.9	*31*
14	*36.9*	*21*

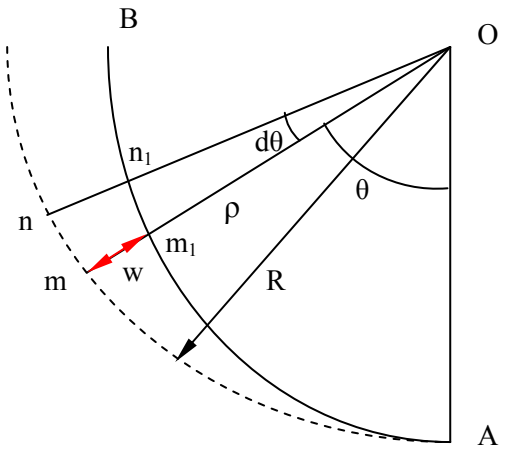

Figure 4.1a: Diagram of the geometry of a curved bar A-B.

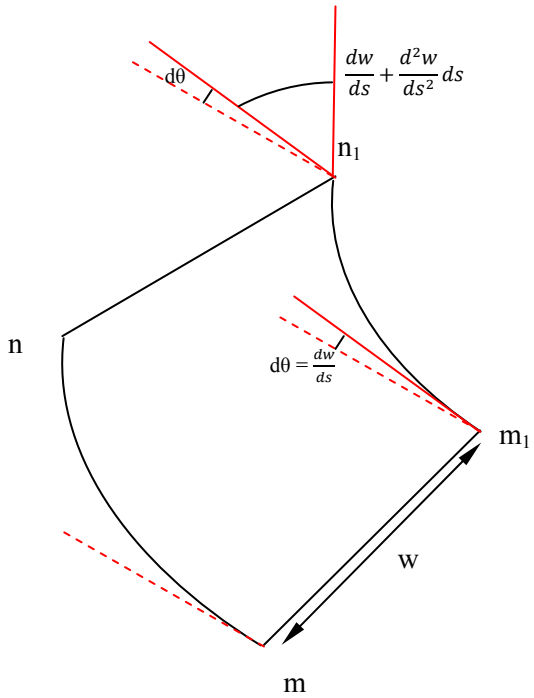

Figure 4.1b: Schematic diagram of the exaggerated deformations of a part of the ring.

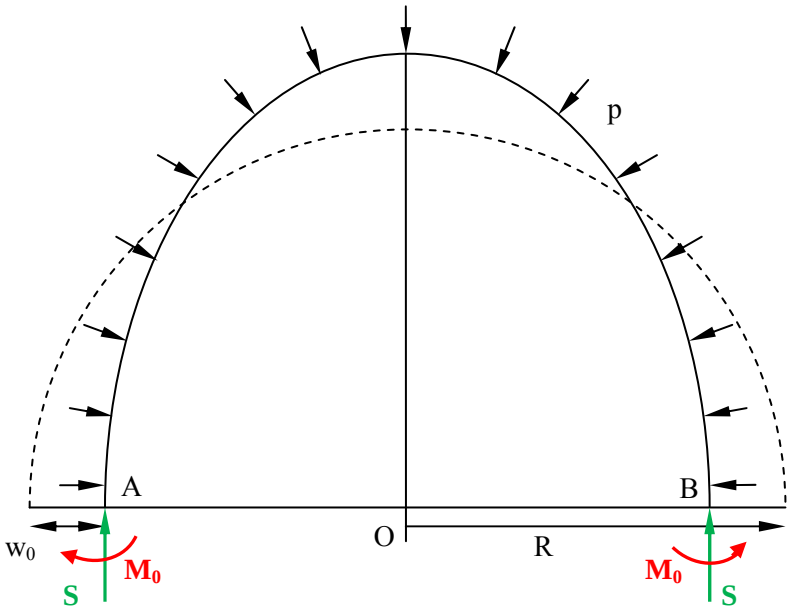

Figure 4.2: *Geometry of the deformed ring. The dotted line indicates the initial circular shape of the ring and the full line represents the deflected ring under the pressure p.*

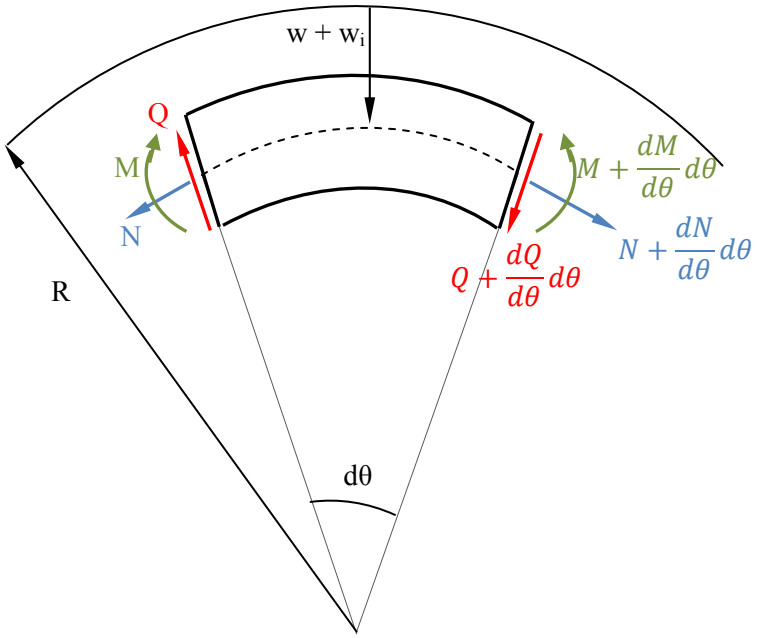

Figure 4.3a: Schematic diagram of a portion of the ring, showing the internal force resultants.

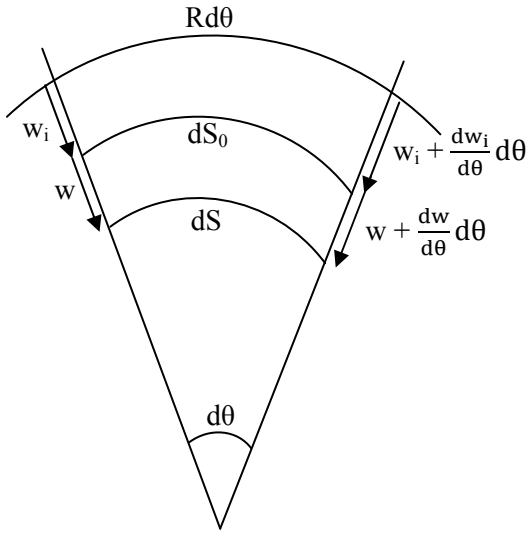

Figure 4.3b: Schematic diagram of a portion of the ring showing relationship between the strain ε and the curvature κ. Only the centerlines are represented.

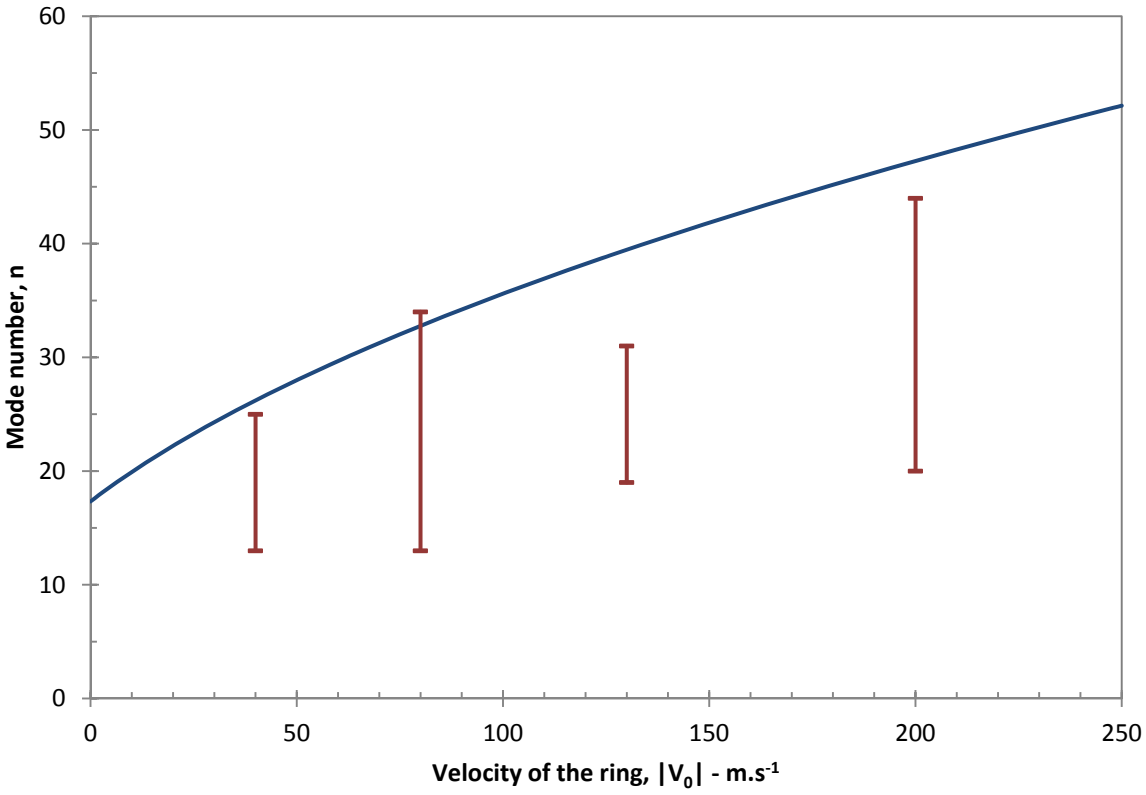

Figure 4.4: *Graph of the critical mode n_c (blue line) as a function of the absolute value of the velocity V_0 from the analysis (Eq. 4.26). The red lines represent the range from minimum to maximum mode numbers found in the experiments.*

Table 6: *Comparison between the computed critical mode numbers, minimum and maximum modes observed in the experiments.*

Charge level (kV)	***V_O ($m.s^{-1}$)***	***Critical mode number n_c***	***Minimum mode number n_{min}***	***Maximum mode number n_{max}***
2	*-40*	*26*	*13*	*25*
3	*-80*	*33*	*13*	*34*
4	*-130*	*39*	*19*	*31*
5	*-200*	*47*	*20*	*44*

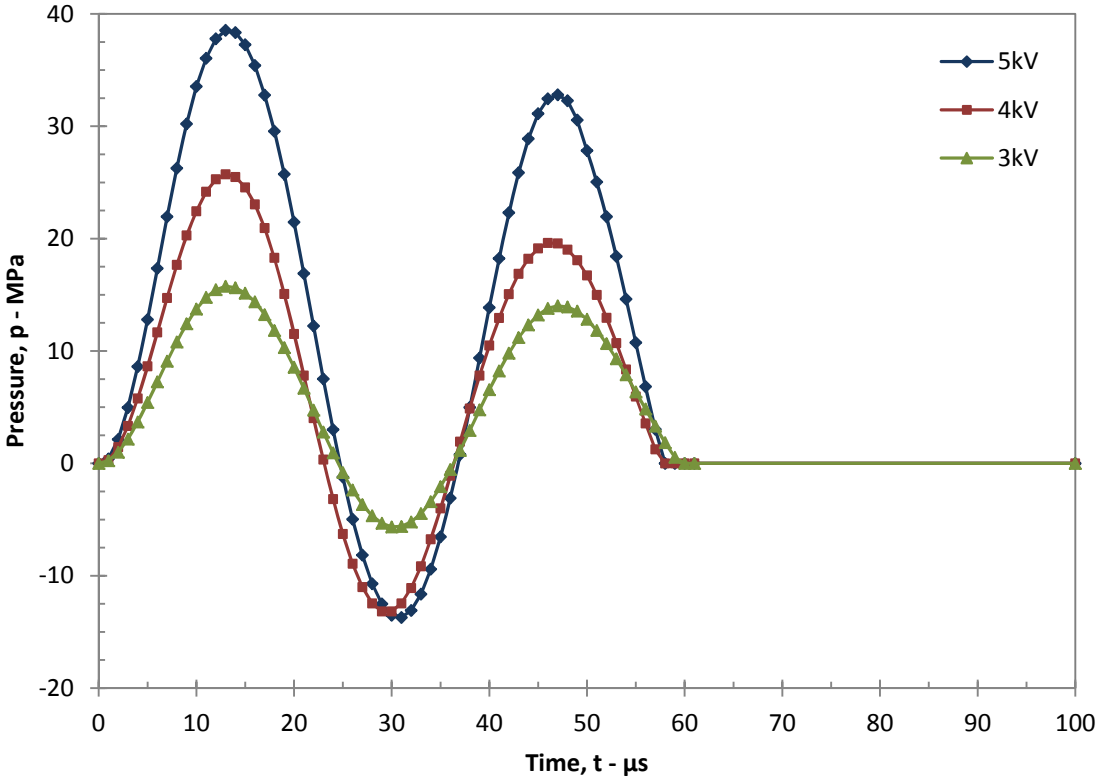

Figure 4.5: Time variation of the pressure used in the ABAQUS simulations. The points on these plots refer to the discrete value taken for the model in ABAQUS.

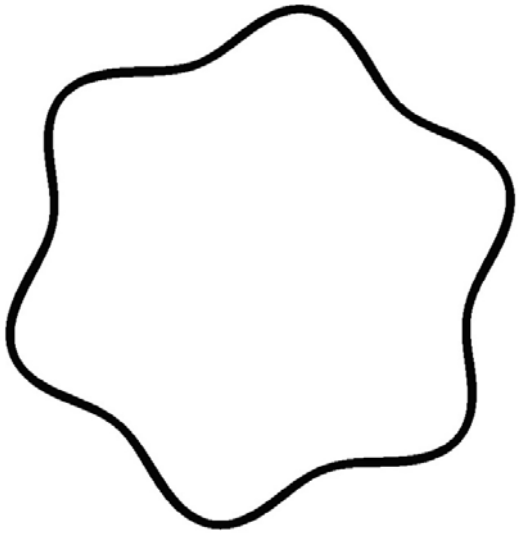

(a) mode 6

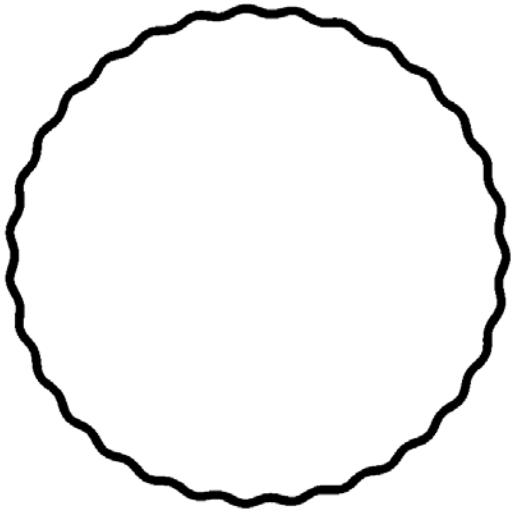

(b) mode 30

Figure 4.6: Examples of buckling imperfection shapes after ABAQUS buckling analysis, for mode 6 (a) and mode 30 (b).

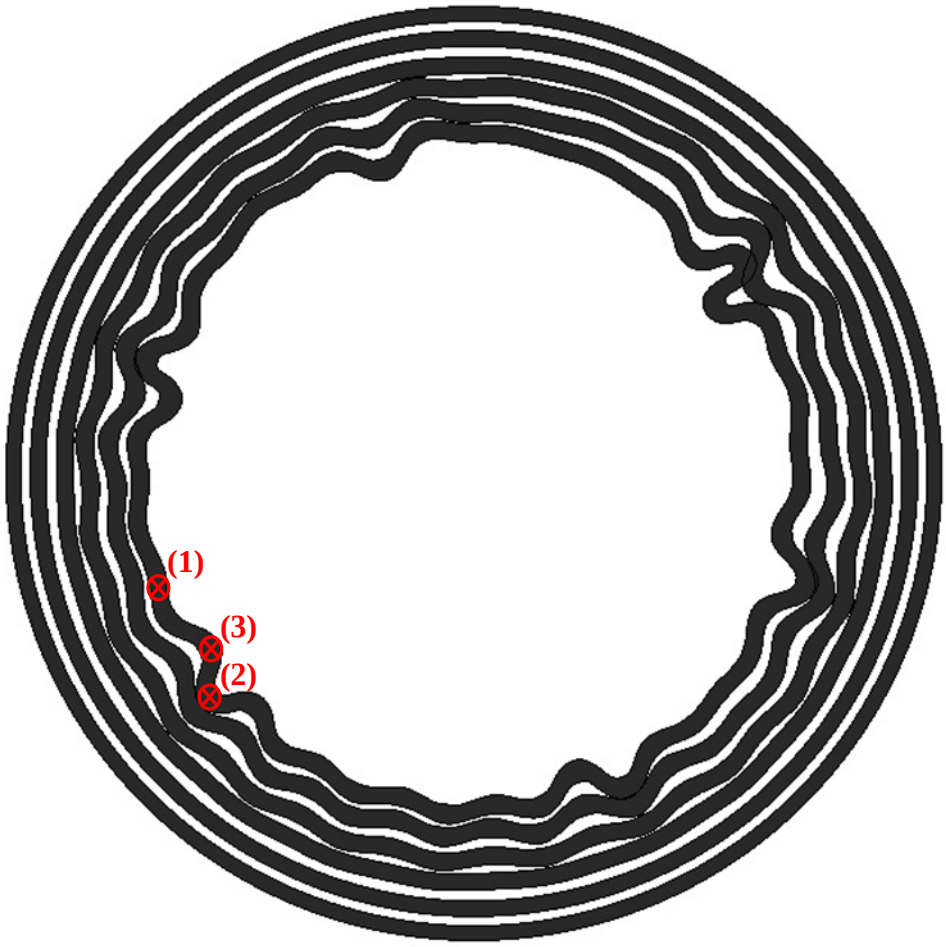

Figure 4.7: *Overlay of several images taken between 0 and 72 µs from the 3 kV ABAQUS simulation. The red crosses and numbers indicate the points considered in Figure 4.8.*

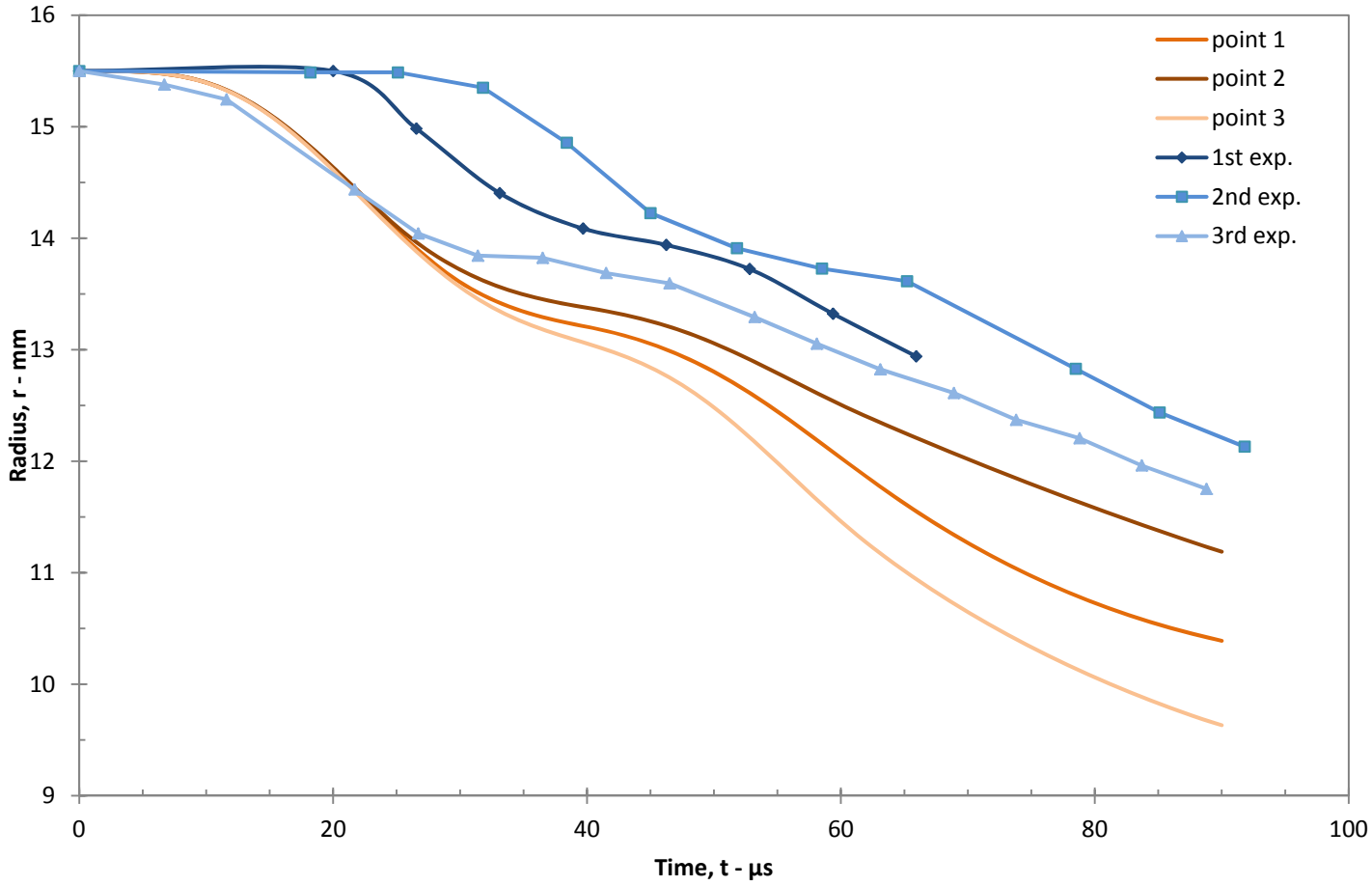

Figure 4.8: *Time variation of the radius at points (1), (2) and (3) for the 3 kV ABAQUS simulation. The blue lines show the corresponding 3 kV experimental data.*

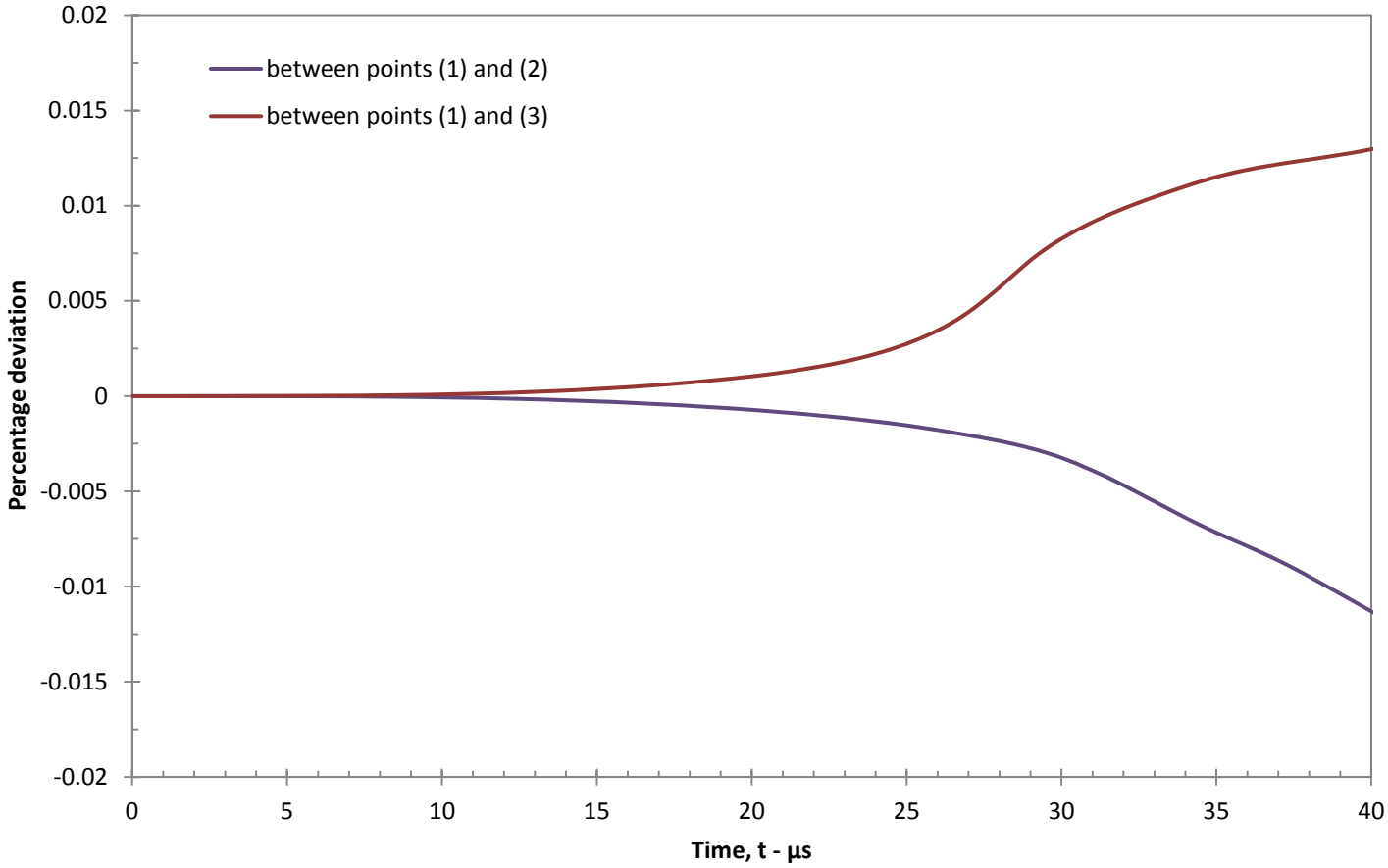

Figure 4.9: Percentage deviation between the radii at points (2) and (3) with respect to the radius at point (1).

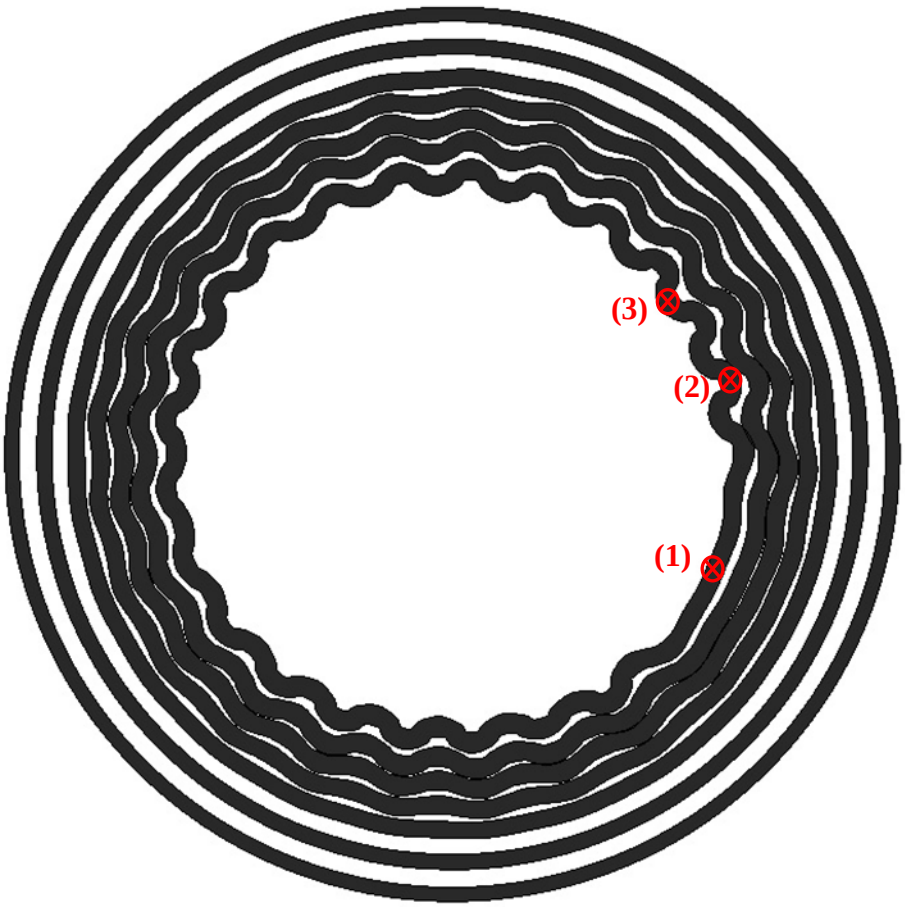

Figure 4.10: Overlay of several images taken between 0 and 60 μs from the 4 kV ABAQUS simulation. The red crosses and numbers indicate the points considered in Figure 4.11.

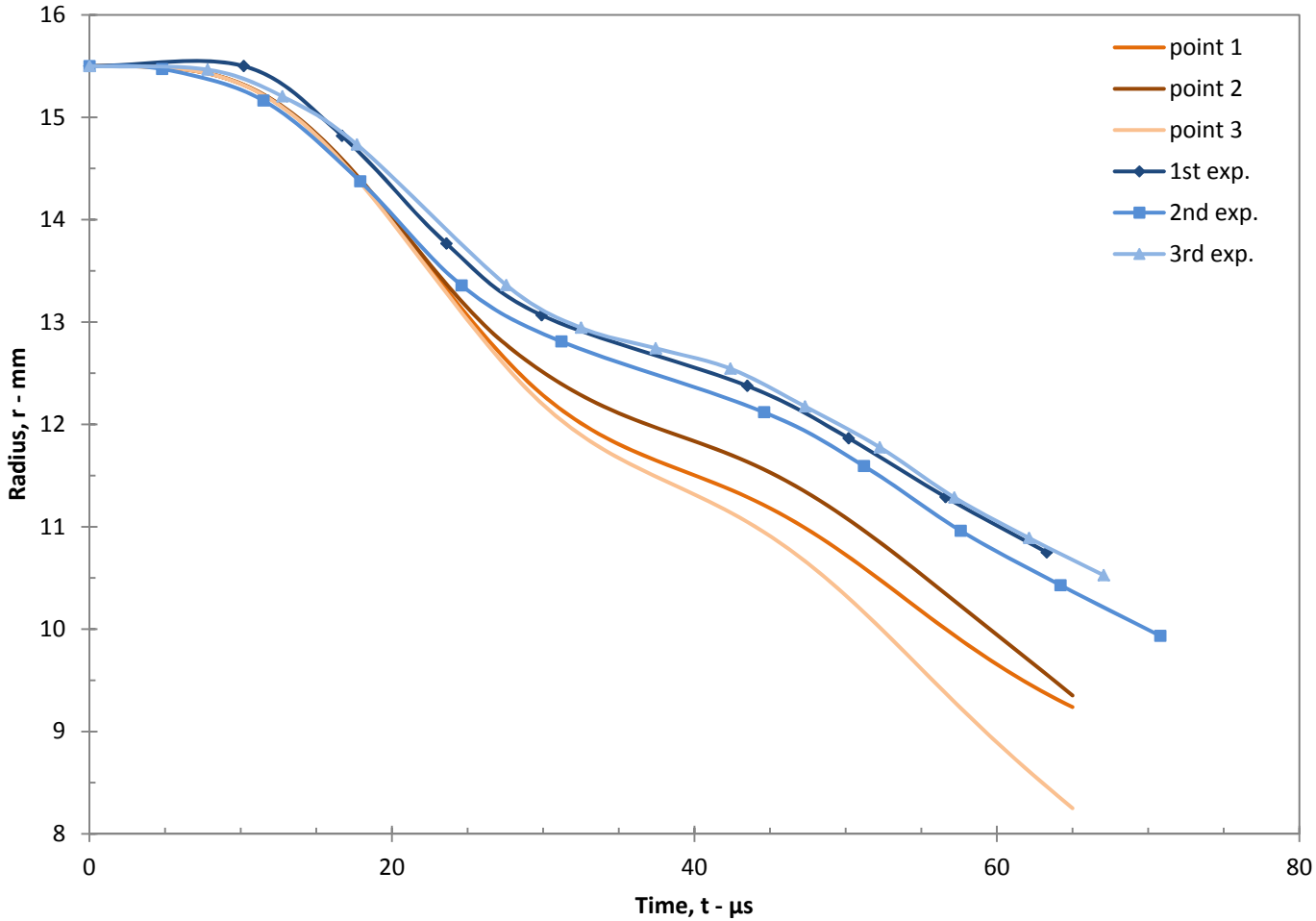

Figure 4.11: Time variation of the radius at points (1), (2) and (3) for the 4 kV ABAQUS simulation. The blue lines show the corresponding 4 kV experimental data, all shifted by Δt = 7 µs.

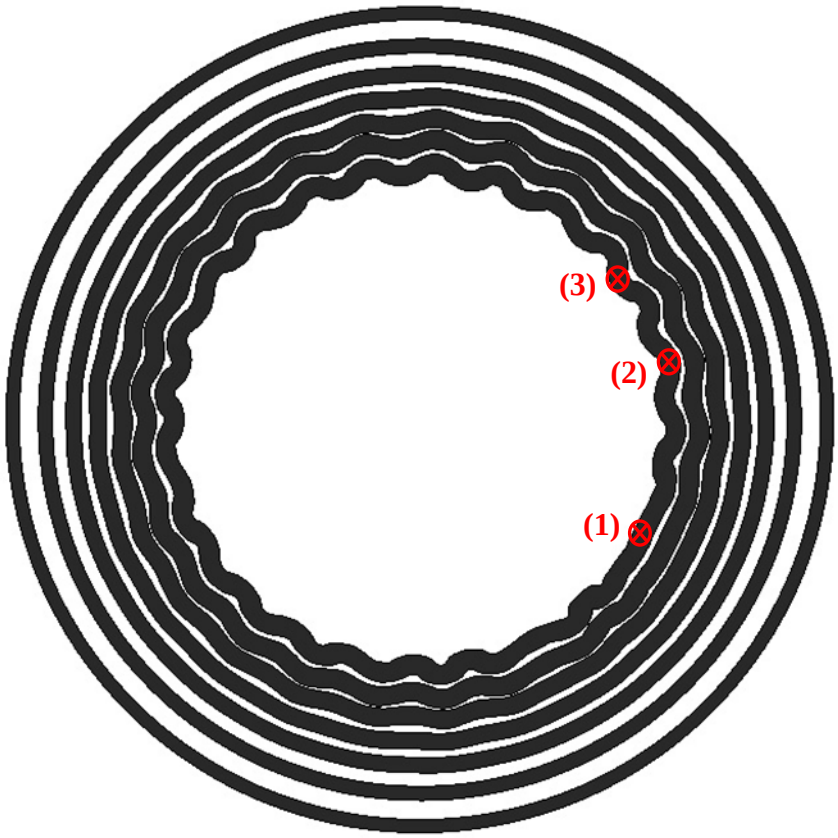

Figure 4.12: Overlay of several images taken between 0 and 35 µs from the 5 kV ABAQUS simulation. The red crosses and numbers indicate the points considered in Figure 4.13.

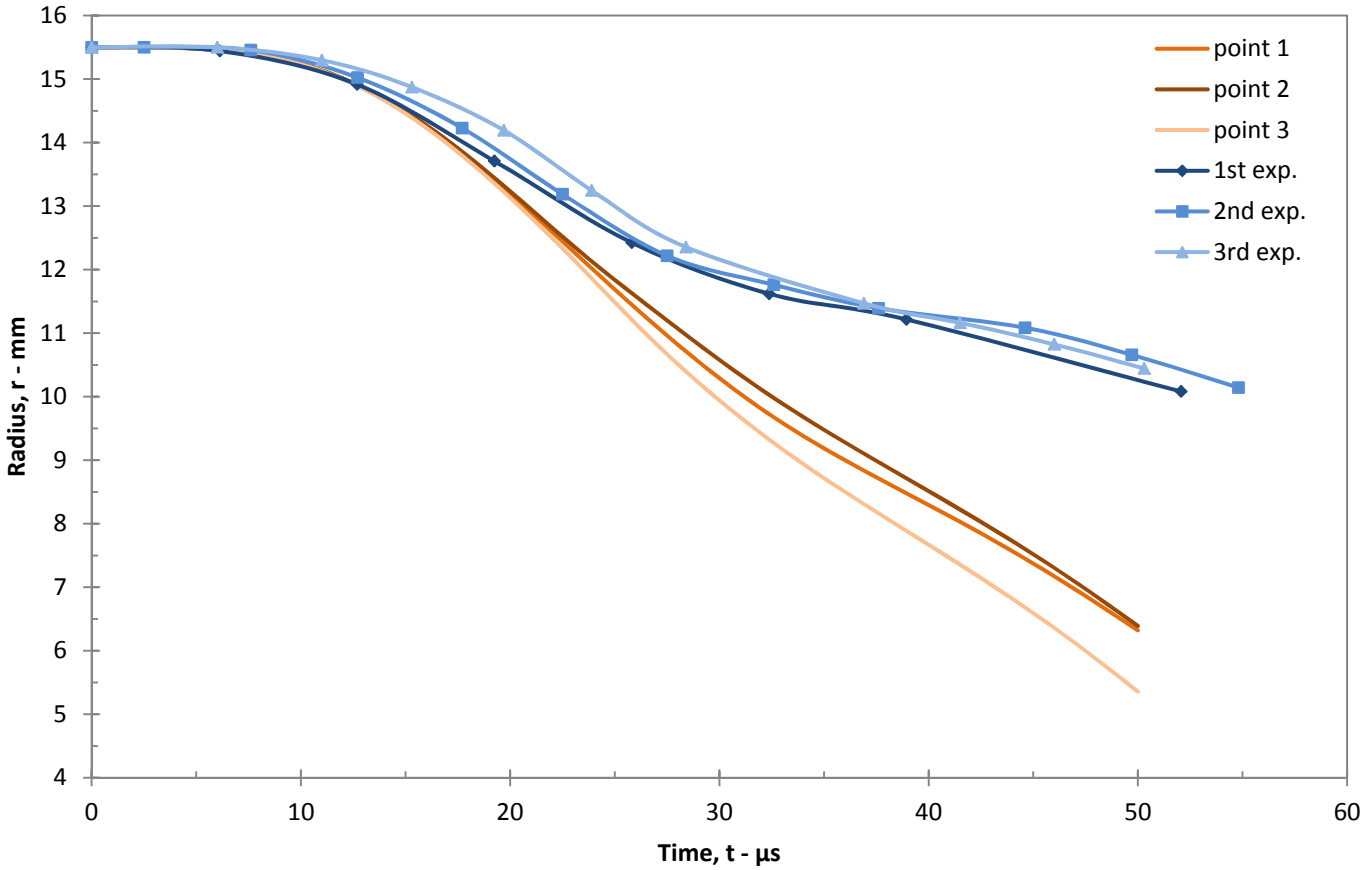

Figure 4.13: Time variation of the radius at points (1), (2) and (3) for the 5 kV ABAQUS simulation. The blue lines show the corresponding 5 kV experimental data. The first experimental curve is shifted by an amount of 7 µs.

References

ABAQUS Theory Manual, Version 6.7, Dassault Systèmes, 2007

AIP American Institute of Physics Handbook, Third Edition, *New York*, 1972

Al-Hassani S.T.S., Duncan J. L., Johnson W., On the parameters of the Magnetic Forming Process, *Journal of Mechanical Engineering Science* 1974, Vol.16 No.1

Al-Hassani S. T. S., The Plastic Buckling of Thin-walled Tubes Subject to Magnetomotive Forces, *Journal of Mechanical Engineering Science* 1974, Vol.16 No.2

Anderson D. L., Lindberg H. E., Dynamic Pulse Buckling of Cylindrical Shells under Transient Lateral Pressures, *AIAA Journal* 1968, 4549-472

Brush D. O., Almroth B. O., Buckling of Bars, Plates and Shells, *International Student Edition*, 1975

Florence A. L., Buckling of Viscoplastic Cylindrical Shells due to impulsive loading, *AIAA Journal* 1968, 4530-846

Jackson J. D., Classical Electrodynamics, Second Edition, *John Wiley & Sons*, 1962

Jones N., Okawa D. M., Dynamic Plastic Buckling of Rings and Cylindrical Shells, *Nuclear Engineering and Design* 1976, 125-147

Jones N., Structural Impact, *Cambridge University Press*, 1989

Lindberg H. E., Florence A. L., Dynamic Pulse Buckling, *Martinus Nijhoff Publishers*, 1987

Ravi Chandar K., Zhang H., On the dynamics of necking and fragmentation – I. Real-time and post-mortem observations in Al 6061-O, *Int. J. Fract.* 2006, 142:183-217

Timoshenko S. P., Theory of Elastic Stability, Second Edition, *Engineering Societies Monographs*, 1961

Vita

Aurélien Mainy was born in Pontarlier, France, in 1989. After graduating from Lycée Les Augustins High School, he entered the "Classes Préparatoires aux Grandes Ecoles" at Lycée Saint Louis, Paris. Following the national entrance examination for the French engineering schools, he was admitted at Ecole Centrale de Lille in 2008. In August 2010, he entered the University of Texas at Austin to pursue the degree of Master of Science in Engineering Mechanics as a double-degree program with Ecole Centrale de Lille.

Permanent email addresses: aurelien.mainy@centraliens-lille.org
aurelien.mainy@utexas.edu

This thesis was typed by the author.